UNIVERSITEIT VAN PRETORIA
UNIVERSITY OF PRETORIA
YUNIBESITHI YA PRETORIA
Denkleiers • Leading Minds • Dikgopolo tša Dihlalefi

Preclinical positron emission tomography imaging properties of radiolabeled nimotuzumab:

A retrospective analysis towards imaging application for visualizing epidermal growth factor receptor expression

by

Gladness Mocumi

22005332

Dissertation submitted in partial fulfilment of the requirements for the degree,

MSc in Department of Nuclear Medicine at the Faculty of Health Sciences,

University of Pretoria

Date (13 February 2025)

Candidate

Gladness Mocumi
Student number:22005332
Department: Nuclear Medicine
Faculty of Health Sciences
University of Pretoria

Supervisor

Prof Thomas Ebenhan
Department: Nuclear Medicine
Preclinical Imaging
Faculty of Health Sciences
University of Pretoria

Co-Supervisor

Dr Julie Bolcaen
SSC Laboratory Radiation Biophysics Division
iThemba LABS
Somerset West 7129

Co-Supervisor (Assistant)

Dr Janie Duvenhage
Nucl Med Research Infrastructure
Steve Biko Academic Hospital
Steve Biko and Malan Street
Capital Park, Pretoria 0001

HOD - Nuclear Medicine
Prof Mike M Sathekge
Department: Nuclear Medicine
Faculty of Health Sciences
University of Pretoria

Declaration

I, Gladness Mocumi, declare that the dissertation entitled **"Preclinical Positron Emission Tomography Imaging Properties of Radiolabeled Nimotuzumab: A Retrospective Analysis Towards Imaging Application for Visualizing Epidermal Growth Factor Receptor Expression"**, submitted in fulfillment of the requirements for the degree **Masters in Medical Nuclear Science** at the **University of Pretoria**, is my original work. This dissertation has not been submitted by me, either wholly or in part, for any degree or examination at any other university.

Acknowledgements

I wish to express my heartfelt gratitude to my supervisors, **Prof. Thomas Ebenhan**, **Dr. Janie Duvenhage** and **Dr. Julie Bolcaen** for their invaluable assistance, guidance, and encouragement throughout this study. Special thanks to **Dr. Janie Duvenhage** - your unwavering support, both professionally and emotionally, meant more to me than words can express. You were a pillar of strength and a source of inspiration, and I deeply appreciate your kindness and dedication.

I am also immensely grateful to my family and friends for their unwavering faith in my abilities, their continuous encouragement, and their support, which sustained me throughout this journey.

Additionally, I extend my sincere appreciation to the research radiographers at the **Nuclear Medicine Research Infrastructure** (**NuMeRI)**, **Cecile Swanepoel** and **Liani Smith**, for their invaluable training on the Interview Fusion software and their assistance with the analysis of the PET/CT images. Your expertise and generosity with your time were integral to the success of this work.

Thank you all for contributing to this meaningful chapter of my academic journey.

Financial assistance

The financial support provided by the **Southern African Institute for Nuclear Technology and Sciences (SAINTS) at iThemba LABS** for this study is gratefully acknowledged. The opinions, findings and conclusions expressed in this dissertation are solely those of the author and do not necessarily reflect the views, opinions, or conclusions of SAINTS.

Abstract

The purpose of this study was to evaluate the preclinical imaging properties of radiolabeled nimotuzumab (h-R3) for visualizing epidermal growth factor receptor (EGFR) expression using positron emission tomography (PET). The primary aim was to enhance knowledge of radiolabeled h-R3 to provide insight into its *in vivo* pharmacology and particular EGFR expression patterns using small animal PET imaging.

The research involved a retrospective, exploratory analysis of data sets from animal studies conducted at Sir Charles Gairdner Hospital. This entailed analyzing data obtained from the injection of [^{89}Zr]Zr-DFO-h-R3, [^{64}Cu]Cu-DOTA-h-R3, and [^{64}Cu]Cu-SarAr-h-R3. The imaging data were reconstructed and analyzed using Interview Fusion Software to generate three-dimensional (3D) projections and volumes of interest (VOI). The total radioactivity uptake was calculated for different regions of interest, including the whole body, chest, cardiac region and abdomen. Statistical methods, such as calculating means, standard deviations, and performing two-tailed student's *t*-tests, were employed to evaluate the data and assess significance between groups.

Elevated levels of radioactivity in the abdomen, intestines, liver/spleen, or bone were deemed unfavorable. In contrast to Intravenous (IV) administration, intraperitoneal (IP) injection of [^{89}Zr]Zr-DFO-h-R3 resulted in high levels of radioactivity in the spleen and femoral bone. Intravenous administration of [^{64}Cu]Cu-DOTA-h-R3 exhibited larger amounts of radioactivity in the intestines, liver/spleen compared to IV injected [^{64}Cu]Cu-SarAr-h-R3.

[^{64}Cu]Cu-SarAr-h-R3 and [^{89}Zr]Zr-DFO-h-R3 may be considered for future exploration in EGFR-overexpressing cancers and/or correlation analysis with tissue analyses for h-R3 expression *in situ*.

Table of contents

List of Figures

List of Tables

1. INTRODUCTION

Globally, cancer has emerged as a significant health crisis, claiming almost 10 million lives in 2020.[1, 2] Despite extensive efforts to combat the disease, cancer continues to be the second most prevalent cause of mortality worldwide.[3] Cancer can arise from a series of genetic mutations that lead to uncontrolled cell growth and can potentially spread to other organs.[4, 5] Genetic alterations in proto-oncogenes, tumor suppressor genes and deoxyribonucleic acid (DNA) repair genes are recognized as key drivers that contribute to the development and progression of cancer.[6] Proto-oncogenes play a crucial role in the regulation of normal cell growth and division. However, when these genes undergo genetic mutation, they transform into active oncogenes, leading to uncontrolled cell growth. Tumor suppressor genes function to inhibit cell proliferation. Contrary to proto-oncogenes, the deactivation of tumor suppressor genes causes unregulated cellular proliferation, which is likely to result in cancer. DNA repair genes ordinarily mend damaged DNA, but changes in these genes can result in further DNA damage and contribute to cancer development.[6, 7] The risk factors of cancer are comprised of internal factors and external factors. Internal risk factors include infections caused by certain viruses, bacteria or fungi, gene mutations, changes in hormones, compromised immune systems, and metabolic abnormalities. External factors include excessive consumption of alcohol, poor diet, insufficient physical activity, and smoking of tobacco. Once cancerous cells enter the bloodstream, they travel to other parts of the body where they begin to grow and form new tumors that invade normal tissues – a process known as metastasis.[8, 9]

When cells begin to divide uncontrollably and proliferate, they create tumors, which may be either non-cancerous or cancerous.[7] Benign and malignant tumor types vary in metastatic activity.[10] Benign tumors are not cancerous and do not invade healthy organs/tissues and/or metastasize. However, benign tumors can grow to a considerable size and exert pressure on adjacent organs, nerves or bone structures and usually needs to be surgically removed. Malignant tumors are cancerous, and they tend to invade healthy organs or tissues and often metastasize at some stage to other parts of the body.[7, 8] There are over 100 types of cancers, which are classified by organs or tissues from

which they originate (e.g., lung cancer, ovarian cancer, breast cancer, etc.).[5, 7, 11] This classification is substantiated by the observation that the change from normal cells to malignant cells takes place through a series of alterations in phenotype and genetic composition. Tumor cells frequently retain characteristics comparable to the tissue or organ from which they originally arose, even after spreading to other regions of the body.[12] Growth patterns, malignancies, survival and mortality rates, and response to treatment often vary between cancer types even when developed from the same tissue.[13] According to the origin of the cell types, tumors are classified into five general classes: carcinomas, sarcomas, myelomas, leukemias and lymphomas. *Carcinomas* are malignant neoplasms originating from epithelial cells and constitute most human cancers. *Sarcomas* are solid tumors that originate in connective tissues like muscles, bones, cartilage, and fibrous tissue. *Myeloma* is a type of hematological cancer that originates from the abnormal proliferation of malignant plasma cells in the bone marrow. It constitutes 1% of all cancers and 13% of hematological tumors. *Lymphomas* originate in the lymphatic system's nodes or glands, such as the vessels, nodes, spleen, tonsils, and thymus. *Leukemias*, on the other hand, develop from blood-forming cells and immune system cells.[13, 14]

Globally, gynecological malignancies constitute around 40% of all cancer cases and are responsible for over 30% of cancer-related fatalities among women.[15] Gynecological cancers mostly originate in the female reproductive system including the ovaries, endometrium, cervix, vagina and vulva. The different gynecological cancers classify according to where they develop and grow. The most prevalent gynecological cancer types are ovarian, endometrial and cervical cancers, with ovarian cancer accounting for the highest mortality rate.[5, 16-20] Vaginal and vulval cancers, gestational trophoblastic tumors, and fallopian tubic cancers are among the rarer forms of gynecological malignancies.[18, 21]

Gynecological malignancies are unfortunately very prevalent in Sub-Saharan Africa, resulting in considerable morbidity and death.[22] In the South African context, gynecological malignancies comprise a significant proportion of all cancer diagnoses among females.[23] Breast cancer along with cervical cancers make up for 85% of gynecological malignancies in the country.[24] The primary risk factors for gynecological

cancers are the inheritance of defective genes, such as the breast cancer (BRCA) genes, followed by postmenopausal age and hormone replacement therapy.[25-28] Other risk factors include smoking, earlier menarche, low parity, reproductive factors, poor diet, a sedentary lifestyle, smoking, and drinking alcohol.[29, 30] The risk factors and frequency of gynecological cancers vary depending on the type.[30] The accurate classification and staging of gynecological cancers are of paramount importance in predicting patient outcomes, planning treatment strategies, evaluating treatment results, facilitating knowledge exchange, and conducting research.[31] The World Health Organization (WHO) provides guidelines for diagnosing gynecological tumors, while the TNM (Tumor/Nodes/Metastasis) system and the International Federation of Gynecology and Obstetrics (FIGO) classification system are employed to classify and stage malignant tumors, taking into account their extent and spread within the body.[32] The TNM system evaluates the tumor's behavior and natural history by considering its localized growth, regional lymph node involvement, and distant spread. Cancers are then classified into stage categories based on their similar prognosis, as determined by the T, N and M categories.[33]

The development of cervical carcinoma is predominantly attributed to prolonged infection with oncogenic strains of human papillomavirus (HPV).[34] It is often observed in the thirties but becomes more prevalent in the forties, with a higher incidence post-menopause.[35] Rare histological types of cervical cancer are more prevalent in young females.[36] The two principal histological subtypes of cervical cancer are squamous cell carcinoma (SCC) and adenocarcinoma. The SCC is classified into HPV-associated SCC and HPV-independent SCC. HPV-associated SCC is typically associated with a more favorable prognosis, while HPV-independent SCC may have TP53 mutations.[36, 37] Mutations in the TP53 gene can alter the function of the p53 protein. These mutations are common in various cancers and can impact prognosis and treatment.[38-40] Adenocarcinoma is classified into HPV-associated and HPV-independent types, including gastric-type, mesonephric type and clear cell type.[37, 41] The risk factors of cervical cancer include HPV infections, smoking, multiparity, early sexual debut, having numerous sexual partners and a prior diagnosis of sexually transmitted diseases.[42-45]

Endometrial cancer is the most frequently diagnosed gynecological cancer in developed regions and the second most prevalent in developing nations, with the highest incidence rates occurring in postmenopausal women.[46-48] The primary histological classifications of endometrial cancer include endometrioid carcinoma, serous carcinoma, clear cell carcinoma, mucinous carcinoma and undifferentiated or dedifferentiated carcinoma.[37, 49] Endometrioid and mucinous carcinomas are classified as type I endometrial cancers, with endometroid carcinoma being the most prevalent type.[50-52] While, serous and clear cell carcinomas are classified as type II endometrial cancers.[51, 52] Undifferentiated endometrial carcinoma is a high-grade, poorly differentiated tumor associated with an unfavorable clinical outcome.[53, 54] Factors that increase the risk of developing endometrial cancer include being overweight, exposure to estrogen without the balancing effects of progesterone, physical inactivity, early menarche, diabetes and Lynch syndrome.[49, 55, 56]

Vulval and vaginal cancers are less common compared to cervical and endometrial cancers.[57, 58] SCC is the most prevalent subtype, with adenocarcinomas and melanomas also occurring.[59, 60] Melanoma arises from pigment-producing cells and is rare but aggressive.[60, 61] Adenocarcinoma originates from glandular cells and can either be primary or secondary from other sites.[62] Risk factors for these cancers include HPV infections, smoking, chronic inflammation of the vulvar or vaginal regions and immunosuppression.[63-66]

Ovarian cancer is a diverse condition that can be classified into various subtypes (i.e., epithelial ovarian carcinomas, gem cell tumors and stromal cell tumors) according to tumor origin, etiology, pathogenesis, molecular alteration, risk factors, morphology and prognosis.[19, 67, 68] Ovarian cancers are predominantly of the epithelial subtype, which can be further categorized into type I and type II tumors.[25, 69] Type I cancers are highly differentiated (low grade), genetically stable and are confined to the ovaries. These cancers develop from precursor lesions including cystadenomas or borderline tumors. The most common subtype of type I cancers includes serous cancer, mucinous, endometroid carcinomas and Brenner tumors. Type II ovarian cancers are typically poorly differentiated, highly aggressive and develop rapidly without discernible precursor lesions. These types of tumors are present in extensive disease stages, and can be

classified into serous, endometroid, clear cell and transitional cell carcinoma.[68, 70] The greatest risk factor of this disease is the inheritance of faulty genes (e.g., BRCA genes), but also postmenopausal age, early age at menarche and estrogenic replacement therapy.[25-28, 71]

Gynecological malignancies, including ovarian, cervical and uterine cancers, often present with unclear or no symptoms during their early stages.[72, 73] This can result in delayed diagnosis, frequently until the cancer has advanced to a later stage.[73] One of the major challenges in gynecological cancers is the need for highly sensitive and specific biomarkers for early detection.[74, 75]

2. LITERATURE REVIEW

2.1 Diagnostic procedures

Many diagnostic procedures are employed for the evaluation and diagnosis of gynecological cancers. These procedures are essential for confirming the presence of gynecological cancers, determining the severity of the diseases and guiding the treatment decisions. Different diagnostic approaches include a combination of imaging studies, laboratory tests and tissue sampling techniques.

A pelvic examination is often the initial step in evaluating gynecological symptoms.[76] Healthcare providers assess the pelvic organs for any abnormalities, such as masses, tenderness, or enlarged lymph nodes.[77]

The Cancer Antigen 125 (CA-125) is a protein more commonly expressed on the surface of ovarian cancer tissues and is also secreted into the bloodstream.[78, 79] It is often employed as a tumor biomarker to monitor the response to treatment of ovarian cancer patients and to evaluate the recurrence of ovarian cancer in ovarian cancer survivors.[78] CA-125 blood tests are sometimes utilized in combination with other screening techniques to improve the sensitivity and specificity of ovarian cancer detection (e.g., CA-125 detection combined with trans-vaginal ultrasound).[71] Human Epididymis Protein 4 (HE4) is an additional biomarker that may be elevated if ovarian cancer occurs and can be used in conjunction with CA-125 for diagnosis. HE4 measurement has been found to be more diagnostically accurate than CA-125 in the identification of ovarian cancer.[80-82] Genetic screening for variants in genes such as BRCA1 and BRCA2 may be advisable

for patients with a family background of gynecological cancers to assess their risk and guide treatment decisions.[83, 84]

Biopsy is an alternative diagnostic procedure performed by taking a tissue sample from the affected areas for pathological examination.[85] Biopsies are used in various cancer diagnoses to assist in verifying the presence of cancer, determine the histological subtype, and evaluate the severity and stage of the disease.[86] Types of biopsies used in gynecological cancers may include colposcopy, endometrial biopsy and ovarian biopsy. A colposcopy is examining the cervix, vagina and vulva using a magnifying instrument called a colposcope. Biopsies may be taken during this procedure to sample suspicious areas.[87-89] Obtaining an endometrial specimen through biopsy enables the examination and diagnosis of endometrial cancer or other uterine abnormalities.[90] In cases of suspected ovarian cancer, a biopsy of ovarian tissue or fluid may be carried out for pathological analysis.[91] Laparoscopy is a minimally invasive procedure that involves the insertion of a thin, illuminated tube (laparoscope) equipped with a camera into the abdomen, with the purpose of visualizing the ovaries, fallopian tubes and other pelvic organs.[92-94] It can assist in the identification of ovarian tumors and the collection of tissue samples for biopsy.[95]

Another elegant approach used for diagnosis is to use whole body *in vivo* imaging techniques. *In vivo* imaging facilitates non-invasive assessment of target cells and tissues in real time and can thereby offer more precise diagnosis, staging and monitoring of cancer treatment outcomes.[70, 96] These modalities include trans-vaginal ultrasound (US), magnetic resonance imaging (MRI), single-photon emission computed tomography (SPECT), computed tomography (CT) and positron emission tomography (PET).[71, 97, 98]

2.2 Non-invasive imaging techniques used in gynecological cancers

2.2.1 Ultrasound

Trans-vaginal ultrasound (US) produces sound waves to generate detailed images of organs and neighboring structures. US serves as the initial imaging technique used for individuals with suspected ovarian cancer.[99, 100] It is a safe, inexpensive technique that can often identify ovarian masses, cysts as well as tumors.[71] US is a pivotal modality in

the early identification and assessment of gynecological malignancies and the evaluation of tumor dimensions within the pelvic and abdominal regions. Trans-abdominal and trans-vaginal US techniques are also the principal imaging techniques for the diagnosis of ovarian cancer. Trans-abdominal ultrasound utilizes low frequency convex probes to determine adnexal masses that extend beyond the pelvic region. Trans-vaginal ultrasound employs a high frequency endocervical probe that is placed adjacent to the ovaries, thereby providing excellent spatial resolution.[70, 101]

2.2.2 Anatomic imaging (CT and MRI)

Computed tomography (CT) and magnetic resonance imaging (MRI) are both employed to define the stage of the disease and for follow-up assessments. CT leverages ionizing radiation to create cross-sectional visualizations of the abdomen and pelvic area, furnishing detailed data regarding the sizes and positions of tumors as well as their probable metastatic potential.[70, 71] CT is also frequently used to determine the feasibility of optimal surgical cytoreduction.[99, 102] MRI serves a crucial function in determining the origin of a pelvic mass and identifying an adnexal mass with its high-quality magnetic fields and pulsed radiofrequency waves that produce images with exceptional soft tissue contrast and resolution.[102, 103] The use of MRI scans is very useful for assessing the tumor's dimensions, the extent of tissue infiltration and the involvement of lymph nodes.[104, 105]

2.3 Nuclear imaging

Nuclear imaging modalities have been utilized in the assessment, staging, therapy and monitoring of cancer.[106, 107] Nuclear imaging involves the use of radioactive compounds that are attached to specific substances, enabling the selective targeting of desired cells or anatomical sites. This enables the visualization and examination of the functional processes occurring in the target.[108] As a result, it has become one of the primary approach for molecular imaging in personalized cancer therapy and has contributed to the development of personalized and effective strategies for combating gynecological cancers by providing functional and molecular insights into tumors.[109-111]

Single-photon emission computed tomography (SPECT) and positron emission tomography (PET) are imaging techniques in nuclear medicine, both providing functional

imaging data enabling the visualization of physiological processes.[112-114] SPECT utilizes gamma rays emitted by a radiotracer to produce 3D images of the distribution of the tracer in the body.[115, 116] PET monitors the spatial distribution of radionuclides that emit positrons and are coupled to targeting molecules. PET is generally thought to be more suitable than SPECT as it offers higher sensitivity and higher resolution.[114, 117]

SPECT and PET are frequently combined with CT (SPECT/CT, PET/CT) as a powerful tool for capturing both functional and anatomical information in the body.[111, 117] PET/CT imaging can offer meaningful insights into the molecular pathobiology and extent of the disease, which can then inform treatment decision-making.[118] PET/MRI combining scanners are also available, often for more intricate investigations or soft tissue based organ-specific imaging (e.g., brain). Recently, total-body PET scanners became available as a technological advancement to hyper-increase image sensitivity or drastically reduce scan times.[119]

2.4 PET tracers for imaging of gynecological cancers

Several PET tracers have been engineered to enable the diagnostic investigations of gynecological cancer.[108, 109, 120] Tracers such as 2-deoxy-2-[^{18}F]fluoro-D-glucose ([^{18}F]FDG), [^{18}F]fluoro-3'-deoxy-3'-L-fluorothymidine ([^{18}F]FLT), 16α-[^{18}F]fluoro-17β-estradiol ([^{18}F]FES), [^{18}F]fluoro-misonidazole ([^{18}F]FMISO), [^{64}Cu]copper(II)-diacetyl-bis(*N*^{4}-methylthiosemicarbazone) ([^{64}Cu]Cu-ATSM) and [^{18}F]fluoro-azomycin-arabinoside ([^{18}F]FAZA) provide insight into metabolic, proliferative and molecular characteristic of gynecological tumors.[121, 122] These tracers will enable the clinicians to visualize and quantify the biological activity within tumors to accurately stage, plan treatment and evaluate therapeutic response.[121, 123] [^{18}F]FDG is the most frequently utilized PET radiotracer to detect, stage and monitor cancer by measuring glucose metabolism in tumors. This technique is based on using [^{18}F]FDG as a radiolabeled glucose analogue. Malignant tumor cells have elevated metabolic activity compared to the healthy neighboring tissue and will therefore take up more glucose than normal cells for glycolysis.[124] Cellular hexokinase can phosphorylate both [^{18}F]FDG and glucose, enabling them to enter the glycolytic pathway.[125] However, unlike glucose, [^{18}F]FDG cannot undergo further metabolic processing, resulting in its continuing retention within

tumor cells.[126] This PET tracer has been used to visualize and detect ovarian cancer by identifying regions with heightened glucose metabolism, which are indicative of malignancies, particularly germ cell tumors.[127] [^{18}F]FLT is a radiotracer that is utilized to detect active proliferating cells.[128, 129] This tracer is employed to assess tumor development and treatment response in ovarian cancer by measuring the rate of DNA synthesis.[108] [^{18}F]FLT is taken up by actively dividing cells through the pyrimidine salvage mechanism, mostly during their cell cyclic S-phase, and then becomes trapped within the cells by thymidine kinase (TK1) – dependent phosphorylation.[130] The intercellular retention of [^{18}F]FLT is a measure of cellular TK1 activity, which is closely associated with cellular proliferation and represents a key enzyme in the DNA synthesis salvage pathway.[120, 129] [^{18}F]FES is a radiolabeled estradiol analog that has proven to be the most suitable estrogen receptor (ER) ligand. It is commonly used in targeting overexpressed ERs found in gynecological malignancies, for instance breast cancer, and can therefore represent the ER expression levels and predict the efficacy of endocrine therapy.[131-133]

Cellular hypoxia is frequently found in solid tumors including ovarian cancers.[134-136] The influence of hypoxic conditions on the outcomes of immunotherapy is a critical factor to consider when devising treatment strategies.[137] Tracers that have been used for imaging cellular hypoxia include [^{18}F]FMISO, [^{64}Cu]Cu-ATSM and [^{18}F]FAZA. Both, [^{18}F]FMISO and [^{18}F]FAZA are 2-nitroimidazole compounds. These compounds permeate into cells and undergo a succession of reductive transformations. In an oxygen-rich environment, these compounds are quickly re-oxidized and diffused out of cells.[138] However, under hypoxic conditions, these compounds undergo reductive metabolism, forming highly reactive intermediates that associate with intracellular macromolecules and accumulate in hypoxia sites.[134, 139, 140] [^{18}F]FMISO represents the most extensively studied hypoxia-imaging tool and is utilized in numerous cancer centers worldwide and has been used to evaluate and measure oxygen levels in gynecological cancers before therapy.[108, 139, 141, 142] It has also been utilized to predict the initial resistance to hormone therapy in cancers with ER expression, such as breast cancer.[143, 144] [^{18}F]FAZA has been employed to assess the extent of hypoxia in ovarian malignancy and to estimate how patients will respond to treatment.[145] The neutral, lipophilic molecule [^{64}Cu]Cu-ATSM exhibits the capacity to diffuse from the bloodstream into adjacent cellular structures. Once inside the hypoxic

cells, it undergoes a process of reduction and becomes trapped and accumulates in cells experiencing hypoxia. However, it quickly washes out of normoxic cells without any alterations. This tracer has been used in the identification of patients who are suitable candidates for hypoxia-targeted therapy of cervical cancer. Additionally, [^{64}Cu]Cu-ATSM has been employed to monitor hypoxia during therapy.[120, 146]

2.5 Immuno-PET imaging

Immuno-PET (i.e., antibody-based PET) is a non-invasive imaging technique widely utilized in diagnostics and therapeutics. The integration of monoclonal antibodies (mAbs) with the high-resolution imaging capabilities of PET enables the functional evaluation of target expression, including quantification of *in vivo* tumor targets.[147, 148] The tracers comprise of a signaling agent (e.g., radionuclide) linked to a targeting vector (mAbs or their variants) (**Figure 1**). The connection between radionuclide and mAbs is established using a bifunctional chelator (BFC).[149]

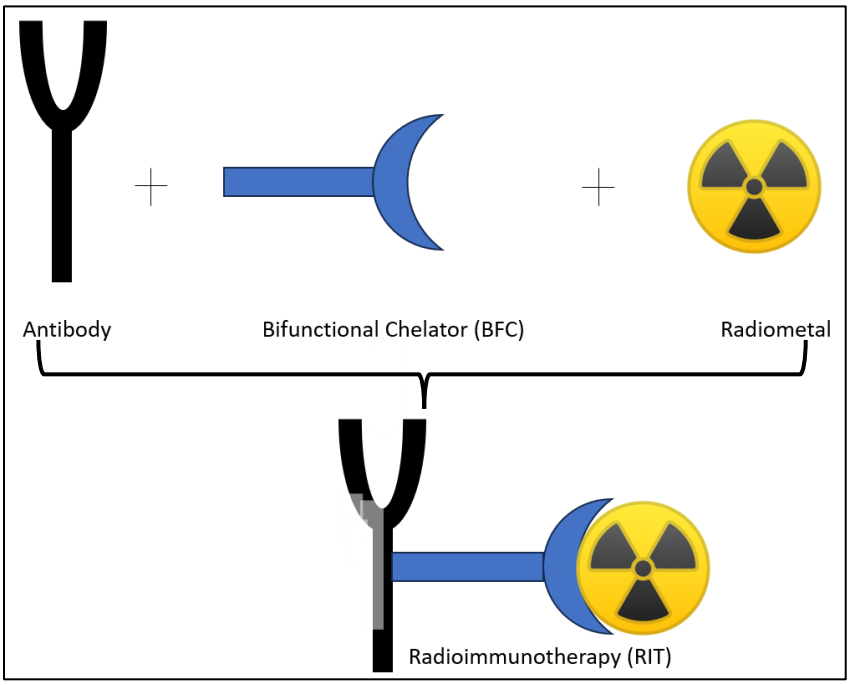

Figure 1: Schematic representation of a radionuclide being linked to a monoclonal antibody via a bifunctional chelator.
Inputs for this figure were obtained from previous publication.[150]

Bifunctional chelators (BFCs) are molecules that contain two functional groups, one for chelation of a radionuclide and the other for coupling to the antibody or antibody fragment.[151] They are engineered to exhibit strong stability and sensitivity to the desired radionuclide, while also causing minimal interference with the binding affinity and specificity of the targeting vector. The choice of a BFC is determined by the specific radionuclide utilized, the targeting vector and the imaging application.[149, 152] To prevent dissociation *in vivo*, it is crucial that the BFC itself is stable *in vivo* and properly complexes and integrates the radionuclide.[153] Antibodies utilized for immuno-PET must exhibit a high-level specificity for the targeted cell, disease or biological process. Various mAbs have been utilized in clinical settings due to their specificity, affinity and stability in serum.[154] Their prolonged circulation time also render them effective as targeting agents for imaging procedures conducted over extended periods.[152, 155]

2.5.1 Immuno-PET radionuclides

Various radionuclides are employed to radiolabel mAbs. The selection of radionuclides typically relies on aligning the physical properties (i.e., half-life, decay mode and energy, labeling chemistry, radiological dose and exposure) with the targeting vector (i.e., mAb) and the specific biological process under investigation.[117, 152] The commonly used radionuclides for immuno-PET imaging include copper-64 (^{64}Cu), zirconium-89 (^{89}Zr) and iodine-124 (^{124}I). They all feature long half-lifes (e.g., ^{124}I = 4.2 days; ^{89}Zr = 3.3 days; and ^{64}Cu = 12.7 hours) which match the antibody's longer biological half-life and are predominantly necessary for imaging of protracted biological processes.[156]

Recent advancements in immuno-PET imaging have demonstrated the potential of radiolabeled antibodies in nuclear medicine. For example, the anti-SAS1B (SB5) antibody has been labeled with ^{89}Zr using the chelator desferrioxamine B (DFO) showed limited uptake in mice bearing uterine cancer tumors, suggesting its potential application in the detection and monitoring of uterine malignancy.[157] Furthermore, previous research has demonstrated the successful coupling and radiolabeling of mAbs with ^{89}Zr for PET imaging in cancer patients.[157, 158] Additionally, radiolabeled anti-EGFR antibodies, such as ^{64}Cu-labeled cetuximab, have been explored for the diagnosis, monitoring and assessment of EGFR-expressing tumors.[159]

2.5.2 Bifunctional chelators

Bifunctional chelators are used to label mAbs with ^{89}Zr are diethylenetriaminepentaacetic acid (DTPA), ethylenediaminetetraacetic acid (EDTA), 1,4,7,10-tetraazacyclododecane-1,4,7,10-tetraacetic acid (DOTA) and deferoxamine (DFO) and its derivatives.[160] DFO and its derivatives are the most commonly utilized chelators for binding with ^{89}Zr.[147] In the past, investigations of PET imaging using ^{89}Zr were conducted using metal chelators such as EDTA and DTPA, to study the coordination behavior and complex generation.[161] EDTA is a hexadentate chelator that includes two extra water molecules in the complexation process.[162] DTPA is capable of occupying the coordination site of zirconium, leading to increased thermodynamic stability of the compound.[163] The thermodynamic of ^{89}Zr-labeled DTPA ([^{89}Zr]Zr-DTPA) was observed to be slightly greater than that of [^{89}Zr]Zr-EDTA, probably due to DTPA's ability to saturate Zr^{4+}, whereas EDTA needs exogenous water molecules.[164] DFO exhibits similarities with EDTA as a hexadentate chelator and displays better chelating properties for ^{89}Zr compared to DTPA.[160] The DTPA ligand coordinates to the metal center via three nitrogen and five oxygen atoms, while the DFO ligand offers six oxygen donor atoms, which are particularly advantageous for the strongly oxophilic zirconium ion.[160] Many preclinical investigations have been conducted utilizing DFO as a labeling agent to conjugate antibodies with the radioisotope ^{89}Zr. However, the *in vivo* stability of the ^{89}Zr -DFO complex remains uncertain, as free ^{89}Zr has been observed accumulating in the bone, which may be influenced by the *in vivo* performance characteristics of the labeled antibody.[164]

^{64}Cu has favorable properties (i.e., half-life and decay scheme) for radiolabeling a diverse array of molecules, accommodating a broad spectrum of molecular weights and pharmacokinetic behaviors. Chelators commonly used for ^{64}Cu include DOTA, 1,4,8,11-tetraazacyclotetradecane- N,N',N''N'''-tetraacetic acid (TETA), bromoacetamidobenzyl-1,4,8,11-tetraazacyclotetradecane-N,N',N'',N'''-tetraacetic acid (BAD), 1,4,8,11-tetraaza-cyclotetradecane-1-(α-1,4-toluic acid) (CPTA) and 1-N-(4-aminobenzyl)-3,6,10,13,16,19-hexaazabicyclo[6.6.6]-eicosane-1,8-diamine (SarAr).[165, 166] DOTA and its variants are frequently utilized to label mAbs with ^{64}Cu, as it is commercially accessible and approved by the Federal Drug Administration.[147, 167]

SarAr includes the diamsar chelator and a linker which enhances the labeling efficiency after conjugation.[168] Sarcophagine chelators (e.g., SarAr) form highly stable complexes especially with ^{64}Cu. This is confirmed by studies showing that the *in vivo* stability of sarcophagine-^{64}Cu complexes surpass that of other chelators like DOTA.[167, 169] [^{64}Cu]Cu-SarAr-ch14.18 and [^{64}Cu]Cu-SarAr-14.G2a have been pre-clinically employed for PET imaging of neuroblastoma and melanoma.[170] The biodistribution results showed that the liver had a low uptake, the ^{64}Cu remained bound to SarAr and was not taken up by endogenous proteins in the liver.[161]

2.6 Immuno-PET for gynecological cancers

2.6.1 The use of monoclonal antibodies in cancer treatment

Most human epithelial cancers display significant overexpression of growth factors, including epidermal growth factor (EGF) and transforming growth factor α (TGFα), as well as epidermal growth factor receptor (EGFR) family members.[171] For example, trastuzumab (Herceptin) and pertuzumab (Omnitarg) are antibodies which have been employed in the management of metastatic breast cancer.[172] Trastuzumab is a humanized mAb that inhibits the activity of the human epidermal growth factor receptor-2 (HER2) and approved anti-HER2 agent for adjuvant treatment in individuals with HER2-positive disease.[173] HER2 is a transmembrane receptor-like protein that belongs to the HER family of tyrosine kinase receptors.[174] Herceptin, a targeted cancer therapy, functions by recognizing and binding to the HER2 protein expressed on the surface of cancer cells. This interaction triggers several mechanisms that contribute to its anti-tumor effects, including stimulating antibody-dependent cellular cytotoxicity, preventing extracellular domain cleavage, disrupting intracellular signaling pathways, diminishing angiogenesis and decreasing DNA repair capacity. These effects ultimately result in slowing down tumor growth, inducing cell death and enhancing clinical results for individuals with HER2-positive breast cancer.[175] The combination of trastuzumab and chemotherapy has demonstrated enhanced efficacy in treating metastatic breast cancer (MBC), with improved response rates, time to disease progression and overall survival outcomes for patients.[173, 176]

Similar to trastuzumab, pertuzumab is a recombinant humanized mAb that is engineered to specifically bind to the extracellular region of the HER2 protein.[174, 177] Omnitarg works by disrupting the interaction between HER2 and other members of the HER protein family, such as HER1, HER3 and HER4. Consequently, the formation of HER heterodimers is restricted.[177] Radiolabeled pertuzumab with lutetium-177 (^{177}Lu) was utilized in a preclinical study to focus on the therapeutic potential of targeting disseminated HER2-positive micro-metastases, such as those found in ovarian cancer. The results demonstrated promising outcomes in terms of preventing tumor progression without adverse side effects, assisting in the preparation of clinical studies for therapy using [^{177}Lu]Lu-pertuzumab.[174] Preclinical investigations have demonstrated that the combination of pertuzumab and trastuzumab exhibits enhanced antitumor efficacy relative to the use of pertuzumab as a single agent. The simultaneous binding of these mAbs to distinct epitopes on the HER2 receptor, without interfering with each other, leads to complementary mechanisms for inhibiting HER2 signaling.[177]

EGFR is frequently overexpressed in diverse cancer cell types. Emerging research demonstrates that the anti-EGFR antibody nimotuzumab (h-R3), in contrast with cetuximab and panitumumab, requires bivalent binding to achieve stable attachment to the cell surface.[171, 178] Nimotuzumab is a mAb of the humanized immunoglobulin G1 (IgG1) isotype that binds to the EGFR with intermediate affinity. The reduced binding affinity of nimotuzumab for EGFR enables the selective targeting of tumor cells expressing high levels of EGFR, while leaving normal cells with lower EGFR expression unaffected.[179] Nimotuzumab is designed to disrupt the signaling pathways that promote the proliferation and persistence of cancerous cells by targeting EGFR and has demonstrated potential in treating tumors that overexpress EGFR, including specific brain malignancies, squamous cell carcinoma of the head and neck, non-small cell lung cancer, pancreatic cancer and epithelial cancers.[169, 180-184] A distinctive characteristic of h-R3 is its comparatively lower occurrence of side effects in comparison to other EGFR-targeting mAbs.[185] This characteristic has played a crucial role in the commercialization of unlabeled h-R3 in many countries and its use in clinical trials for various cancer types.[186] This study pre-clinically evaluates radiolabeled nimotuzumab (h-R3) as a tracer to visualize EGFR expression by using immuno-PET.

2.6.2 Relevant studies using nimotuzumab-based imaging

Radiolabeled-h-R3 has been extensively studied for its therapeutic value of cancer and targeting capabilities by immuno-PET. Barta *et al.* (2013) examined the effect of radiolabeling h-R3 on its uptake in cancer cells.[187] The h-R3 was hereby radiolabeled with iodine-131 (^{131}I) and lutetium-177 (^{177}Lu) and administered intravenously to the animals. ^{177}Lu-labelling was achieved using the following chelators: *p*-isothiocyanatobenzyl-1,4,7,10-tetraazacyclododecane-1,4,7,10-tetraacetic acid (*p*-SCN-Bn-DOTA), 2-(4-isothiocyanatobenzyl) diethylenetriaminepentaacetic acid (*p*-SCN-Bn-DTPA) and DOTA-NHS-ester (N-hydroxy-succinimidyl-DOTA). Nimotuzumab was also labeled with ^{131}I using oxidative iodination procedure, in accordance with the chloramine-T protocol. In this process, the carrier-free isotope ^{131}I was directly conjugated to h-R3. Two cancer cell lines, A431 (human squamous carcinoma) and HaCaT (human keratinocyte), were utilized in the investigation, with these results demonstrating that the choice of radiolabel and its attachment method had only minimal impact on the internalization of h-R3 into these EGFR-expressing cell lines. However, *in vivo*, the type of radiolabel and radiolabeling technique significantly influenced h-R3 clearance and liver uptake. A longer elimination half-life and lower liver uptake were observed for [^{131}I]iodo-h-R3, while ^{177}Lu-labeled h-R3 had a shorter elimination half-life, higher liver uptake, and longer retention in the liver. It was also found that the slowest time of radioactivity clearance from the blood was seen in [^{131}I]iodo-h-R3.[187]

In a different study published by Vera *et al.* (2011), ^{177}Lu-labeled h-R3 was preclinically evaluated for its potential for radioimmunotherapy of tumors with EGFR overexpression.[188] In this study, h-R3 was conjugated with *p*-SCN-Bn-DOTA, and subsequently radiolabeled with ^{177}Lu producing the [^{177}Lu]Lu-*p*-SCN-Bn-DOTA-h-R3 radioimmunoconjugate. [^{177}Lu]Lu-*p*-SCN-Bn-DOTA-h-R3 was acquired with high chemical and radiochemical purity, radiolabeling yield, specific activity and stability, without considerable loss of immunoreactivity. A stability of 95.9% and 93.2% of radioimmunoconjugates in DTPA excess and human serum was found after 10 days. *In vitro* studies were conducted in A431 cells, as well as the human colorectal carcinoma cell line SNU-C2B and a human skin fibroblast cell line. Where the radioimmunoconjugate exhibited specific receptor binding in SNU-C2B and A431 cells. The [^{177}Lu]Lu-*p*-SCN-Bn-

DOTA-h-R3 *in vivo* studies were performed in healthy and xenograft mice. The biodistribution analysis of healthy animals exhibited the characteristic pattern commonly observed with radioimmunoconjugates utilizing monoclonal antibodies. This pattern included uptake in reticuloendothelial organs (i.e., liver and spleen), clearance from the bloodstream over time, low uptake in non-target organs, and the influence of a chelator on blood clearance and organ uptake. The investigation in xenograft mice also showed the uptake of [^{177}Lu]Lu-*p*-SCN-Bn-DOTA-h-R3 in both tumor tissues and reticuloendothelial organs. These findings suggest that [^{177}Lu]Lu-*p*-SCN-Bn-DOTA-h-R3 is a potential radioimmunoconjugate for the targeted radioimmunotherapy of tumors exhibiting overexpression of EGFR.[188]

In 2019 Hartimath *et al.* utilized non-invasive small animal SPECT/CT imaging and *ex vivo* biodistribution to understand the *in vivo* behavior of PEGylated-Maytansine (PEG$_6$-DM1) antibody drug conjugates (ADCs).[189] In this investigation, h-R3-ADCs were conjugated to PEG$_6$-DM1, resulting in the production of immunoconjugates with low (h-R3-PEG$_6$-DM1-low) and high (h-R3-PEG$_6$-DM1-high) drug-to-antibody ratios. To ensure quality control, the researchers employed various analytical techniques, including ultraviolet spectrophotometry, size exclusion high performance liquid chromatography (HPLC), bioanalyzer, biolayer interferometry (BLI) and flow cytometry in EGFR-positive DLD-1 cells. The immunoconjugates were coupled with DOTA and radiolabeled with indium-111 (^{111}In). *In vitro* binding and internalization rates of [^{111}In]In-DOTA-h-R3, [^{111}In]In-DOTA-h-R3-PEG$_6$-DM1-low and [^{111}In]In-DOTA-h-R3-PEG$_6$-DM1-high were characterized showing that conjugation of multiple PEG$_6$-DM1 to h-R3 decreased the affinity for EGFR *in vitro*. Furthermore, the pharmacokinetics, biodistribution and imaging characteristics were assessed in normal and DLD-1 tumor bearing mice. The decreased affinity led to low tumor uptake of [^{111}In]In-DOTA-h-R3-PEG$_6$-DM1-high, with a slow overall whole-body clearance rate. These findings provided valuable insight for evaluating the pharmacokinetics and, normal tissue toxicity of PEGylated ADCs and determining the appropriate dosing rate.[189] In a similar study ADCs using h-R3 conjugated to PEG$_6$-DM1 were developed, which also produced conjugates with low (h-R3-PEG$_6$-DM1-low) and high (h-R3-PEG$_6$-DM1-high) drug to antibody ratios. Near infrared imaging (NIR) was hereby utilized for assessing treatment response. This study further investigated the

compounds employing UV spectrophotometry, size exclusion HPLC, bioanalyzer, BLI and, flow cytometry in EGFR-positive DLD-1, as well as tests in MDA-MB-468 cells (which have high EGFR density) and HT-29 cells (characterized by very low EGFR density). The control antibody drug conjugates were developed using a human anti-maltose binding protein (MBP) antibody. BLI revealed that the binding of h-R3-PEG_6-DM1-low and h-R3-PEG_6-DM1-high was significantly affected by conjugation of the drug. *In vitro* cytotoxicity studies of the immunoconjugates indicated that toxicity correlated with the number of drugs on antibody, with h-R3-PEG_6-DM1-high showing higher activity than h-R3-PEG_6-DM1-low. The immunoconjugates were used to treat EGFR positive Kirsten rat sarcoma viral oncogene (K-*ras*) mutant DLD-1 colorectal cancer xenograft, and DLD-1 cells were transduced with a red fluorescent protein (iRFP702) to allow the use of NIR imaging for tumor response monitoring. The h-R3-PEG_6-DM1-low immunoconjugate resulted in 4/6 completely cured animals while h-R3-PEG_6-DM1-high resulted in 2/5 cured animals. The study found that the ADCs were very effective in a colorectal cancer model *in vivo*.[190]

Chekol *et al*., (2018) conducted research to evaluate the pharmacokinetics, biodistribution, radiation dosimetry and, normal tissue toxicity of [^{89}Zr]Zr-DFO-h-R3 in healthy and tumor bearing mice. In this study, h-R3 was conjugated to DFO and radiolabeled with ^{89}Zr. By using a combination of *in vitro* gel-electrophoresis, BLI, and flow cytometry, the researchers were able to characterize [^{89}Zr]Zr-DFO-h-R3 in terms of its conjugation rate and efficiency, binding kinetics and target specificity. The compound's potential was further evaluated through micro-PET imaging and *ex vivo* biodistribution in healthy and EGFR-positive tumor-bearing mice. PET imaging in the EGFR-positive mice showed high tumor uptake with the highest uptake found in those mice bearing the human DLD-1 cell xenograft. The projected human effective dose was low (0.184 mSv/MBq) in females and not much higher (0.205 mSv/MBq) in males. Cell blood counts and blood biochemistry analyses showed no apparent compound toxicity to normal tissue; showing low organ absorbed dose and effective dose, which suggests that [^{89}Zr]Zr-DFO-h-R3 is suitable for human use.[191]

Izquierdo-Sanchez *et al*., (2018) performed a study that labeled h-R3 with gallium-67 using DTPA as a chelating agent, resulting in [^{67}Ga]Ga-DTPA-h-R3. The researchers then

assessed the biodistribution and affinity of this compound for EGFR-expressing mesothelioma cells using a human cell mice xenograft model. The radiolabeling rate and efficiency, radiochemical purity, serum stability and biodistribution were assessed. After IV administration of [^{67}Ga]Ga-DTPA-h-R3, its biodistribution along with tumor uptake was determined by micro-SPECT/CT scans which demonstrated consistent h-R3 uptake at the tumor site during the first 48 hours after administration. *In vivo* studies employing malignant pleural mesothelioma (MPM) xenografts demonstrated a significant uptake of the radioimmunoconjugate, which proves its potential as a biomarker that could enhance its theranostic utilization in patients with MPM.[192] Nguyen *et al*., (2021) conducted a study to investigate the efficacy of h-R3 coupled with ^{131}I and ^{90}Y to study the inhibition of tumor growth in a human laryngeal carcinoma xenograft model. The binding of h-R3 with ^{131}I was conducted utilizing the chloramine-T method, producing the [^{131}I]iodo-h-R3 conjugate. Nimotuzumab was coupled with *p*-SCN-Bn-DOTA and radiolabeled with ^{90}Y, producing [^{90}Y]Y-DOTA-h-R3 conjugate. [^{90}Y]Y-DOTA-h-R3 displayed immunoreactivity of 80% or more with laryngeal carcinoma cells. The labeled h-R3 conjugates were then assessed for their efficacy in treating laryngeal cancer in tumor-bearing xenograft mice. Mice with laryngeal carcinoma tumors treated with [^{131}I]iodo-h-R3 or [^{90}Y]Y-DOTA-h-R3 demonstrated reduced tumor volume and improved survival rates compared to the untreated control group and the group treated with unlabeled h-R3. Additionally, at equivalent doses, [^{90}Y]Y-DOTA-h-R3 had increased tumor inhibition activity compared to [^{131}I]iodo-h-R3.[193]

In a recent study conducted by Solomon *et al.,* (2020), researchers explored the site-specific labeling of h-R3 using the ΔN-SpyCatcher/SpyTag system in conjunction with various chelators and radiometals. Initially, ΔN-SpyCatcher was reduced using tris(2-carboxyethyl)phosphine (TCEP), followed by conjugation with desferoxamine-maleimide (DFO-mal) to produce a reactive ΔN-SpyCatcher-DFO. This moiety was then reacted with h-R3-SpyTag to create a stable DFO-$^{\text{SpyCatcher-}\Delta\text{N-SpyTag}}$-h-R3, which was subsequently radiolabeled using ^{89}Zr for *in vivo* micro-PET imaging of EGFR-positive MDA-MB-468 tumor xenografts. Similarly, ΔN-SpyCatcher was linked to an eighteen-membered macrocyclic chelator macropa-maleimide and utilized to radiolabel ΔN-SpyTag-h-R3 with actinium-225 (^{225}Ac) for *in vivo* radiotherapy studies. Such radiolabeled h-R3 versions

were also administered IV to healthy female athymic nude mice and mice bearing EGFR-positive MDA-MB-468 tumor xenografts. The results revealed that the conjugation and labeling using SpyTag/ΔN-SpyCatcher to h-R3 did not significantly affect its receptor binding compared to a non-specific conjugation approach. The [^{225}Ac]Ac-$^{SpyTag\text{-}\Delta N\text{-}SpyCatcher}$-h-R3 was effective *in vitro* and in an EGFR-positive/ triple-negative breast cancer xenograft model.[194]

2.7 Routes of tracer administration

The way that a tracer is administered can affect its pharmacokinetics and biodistribution. An IV administration is often used when a full dose with rapid absorption (bioavailability) is required.[195] However, this approach of administration may cause damage to surrounding tissues and increase the risk of systemic side effects, particularly in therapies targeting EGFR.[196] In contrast, intraperitoneal (IP) administration is one of the extensively utilized methods in rodent studies, such as those involving mice and rats. This method is easy to perform, fast, and minimally stressful for the animals. Moreover, larger volumes of tracer can be administered safely to mice through IP administration, compared to IV administration.[197] The success of the administration route is linked to how the radiotracer behaves within the biological system, including factors such as its rate of absorption into tissues, its distribution among organs, its metabolism, and excretion from the body.[198] The route of administration can have a significant impact on the success of cancer therapies. For instance, IP administered chemotherapy has been found to be the more effective treating option for ovarian cancer than chemotherapy given IV.[199] However, there is no information available on whether IP administration of a long-circulating imaging probe, such as radiolabeled h-R3, would have better pharmacokinetics in terms of lower non-specific uptake in areas close to the ovaries compared to IV administration of radiolabeled h-R3. An IP administration has been widely regarded as a successful route for tumor therapy.[200] It has been used to treat episodes of peritonitis in peritoneal dialysis patients and has been employed for chemotherapy in patients with intra-abdominal malignancies, such as gynecological and gastrointestinal cancers.[201] For example, IP injection has been used to administer docetaxel for the treatment of peritoneal dissemination of cancers.[202] IP chemotherapy can be used as a single therapy or in combination with systemic chemotherapy to treat both primary and secondary peritoneal surface malignancies.[203] IP

chemotherapy has demonstrated promise in treating ovarian cancer, both *in vitro* and clinical trials, but its efficacy and toxicity is not widely accepted in gynecologic oncology practice.[204]

3. AIM

This study aims to enhance knowledge of radiolabeled nimotuzumab (h-R3) to provide insight into its *in vivo* pharmacology and particular targeting EGFR expression patterns normal tissue by small animal PET imaging.

4. OBJECTIVES

The objectives of this research study were:

Objective 1 - To demonstrate the impact of IP- over IV administration of [^{89}Zr] Zr-DFO-h-R3 in real time, on *in vivo* tracer distribution and compare it with distribution of IV administered [^{64}Cu]Cu-DOTA-h-R3 and [^{64}Cu]Cu-SarAr-h-R3 using non-invasive, micro-PET/CT image-guided tracer quantification in mice.

Objective 2 - To determine the undesired presence of radioactivity for ^{89}Zr- and/or ^{64}Cu-radiolabeled h-R3 from organ-specific tracer uptake in mice.

5. METHODOLOGY

5.1 Study design

The research focuses on the exploratory, retrospective examination of data sets deriving from animal studies conducted at Sir Charles Gairdner Hospital in Perth, Western Australia. The data includes information obtained from the injection of new radioactive compounds and subsequent sequential small animal PET/CT imaging (i.e., non-invasive real-time tracking of these compounds in live mice) and measurements of the compound-related radioactivity in dissected organ and tissue samples from the same animals used for PET/CT imaging. **Figure 2** illustrates the study concept.

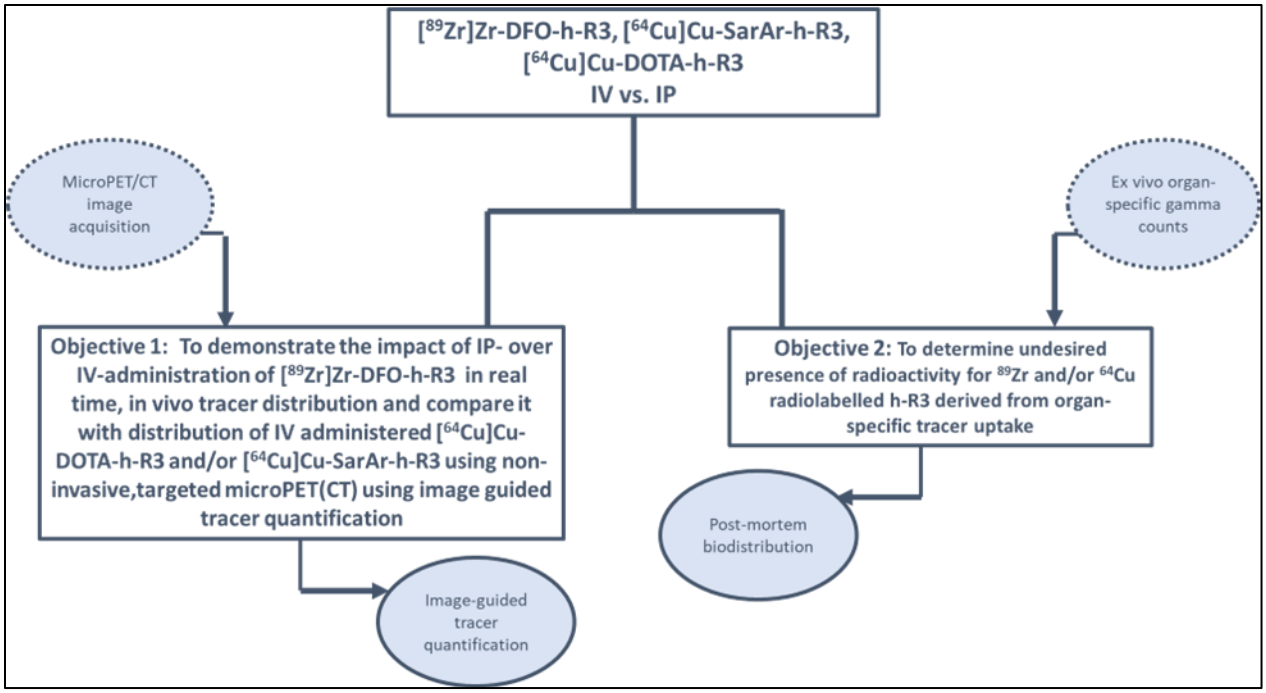

Figure 2: Flow diagram representing the study concept.

5.2 METHODS

5.2.1 In vivo assessment of [^{89}Zr]Zr-DFO-h-R3, [^{64}Cu]Cu-DOTA-h-R3 and [^{64}Cu]Cu-SarAr-h-R3

5.2.1.1 Tracer injections and prerequisite imaging study information

To address the first objective of the retrospective study, several experiments were conducted prior to this study without the involvement of the student. Animal experiments were performed at Rapid Laboratories, Sir Charles Gairdner Hospital, Perth, Western Australia, and were approved by the Animal Ethics Committee of the University of Western Australia (RA/3/100/1236). Three different molecules, namely [^{89}Zr]Zr-DFO-h-R3, [^{64}Cu]Cu-SarAr-h-R3 and [^{64}Cu]Cu-DOTA-h-R3, were investigated following either IV administration into healthy athymic nude mice (8 weeks old, 12-19 g, female). These mice were used to characterize the *in vivo* behavior of [^{89}Zr]Zr-DFO-h-R3, [^{64}Cu]Cu-SarAr-h-R3 and [^{64}Cu]Cu-DOTA-h-R3. The animals were anesthetized with 1.5-3.0% isoflurane in oxygen before the administration of the tracer. The injection formulation (volume = 50 - 150 µl), consisting of saline containing either [^{89}Zr]Zr-DFO-h-R3 (IP injected activity of

11.7 ± 1.1 MBq; IV injected activity of 9.4 ± 1.0 MBq), [^{64}Cu]Cu-SarAr-h-R3 (IV injected activity of 8.5 ± 2.2 MBq), or [^{64}Cu]Cu-DOTA-h-R3 (IV injected activity of 7.8 ± 1.2 MBq). A control group of mice received the same formulation of saline containing either [^{64}Cu]Cu-Cl_2 (IP injection with 26.3 ± 4.1 MBq), or [^{89}Zr]Zr-oxalate (IP injected activity of 6.5 ± 3.4 MBq) to simulate the real-time distribution of ionic ^{89}Zr- and ^{64}Cu-activity *in vivo*. Nuclear imaging was performed using a micro-PET camera. As an input in this study a total of 117 data files, known as "List mode files," were made available for the student.

This research utilized data from PET/CT imaging and reconstructed individual files for each time point (1 h, 2 h, 4 h ,6 h, 8 h and 24 h) post-injection. To visualize the co-registered micro-PET/CT images, specialized software (Inter View XP, Mediso Medical Systems, Debrecen, Hungary) was employed, which generated a 3D projection of the animal's whole body radioactivity signal. The software also provided image slides in axial, coronal and sagittal orientations based on the CT slide thickness. For each micro-PET scan, the corresponding images were analyzed using the Interview Fusion Software (Mediso, Hungary) to draw 3D-volumes of interest (VOI). The results are calculated using the total radioactivity uptake (kBq/ml) of each tracer after determining the relevant areas of interest, including VOIs for the whole-body, chest, cardiac region and abdomen. The file identification, body weight, injected activity, scan times, and organ VOI information were recorded in a data collection sheet using MS Excel (Microsoft, Redmond, WA, U.S.A) for further analysis.

Statistical analysis was performed to evaluate the data, with the mean and standard deviation (SD) reported. The coefficient of variation (CV) was calculated to compare the SD to the mean. A CV value less than 1 indicates a low SD which is less than the mean. A CV value more than 1 indicates a high SD that is greater than the mean. A two-tailed student's *t*-test was used to assess statistical significance between groups. A *P*-value of less than 0.05 was considered statistically significant.

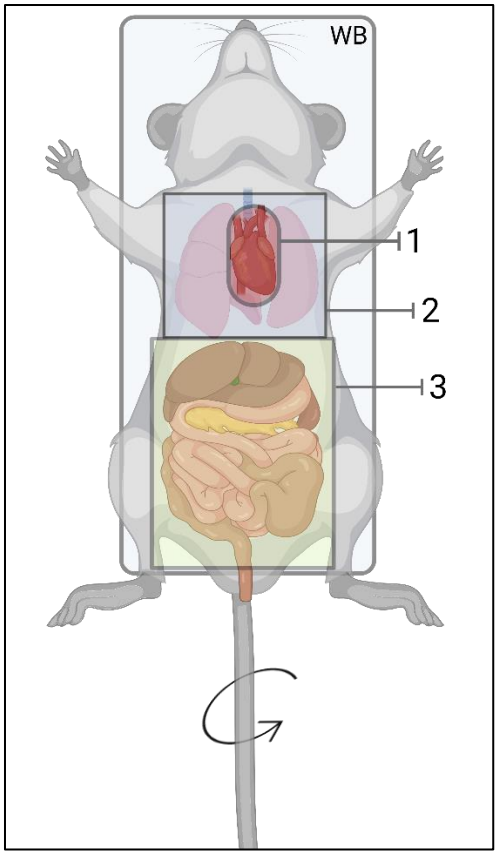

Figure 3: Scheme of micro-PET volume-of-interest area positioning.
Animals were enrolled in a simple image guided analysis by using volume of interest (VIO) areas that are manually drawn on each 3D PET image (CT support for alignment and orientation) **WB**) whole body VOI **1**) cardiac/ heart VOI **2**) thorax/ chest VIO and **3**) abdominal VIO utilized for all data sets. Positioning and size may differ between individual animals.

5.2.1.2 Study assessment scope

The research project investigated three main areas. Initially, the quality of each reconstructed image was assessed, and criteria for inclusion/exclusion (refer to Table A1) were established. Based on these criteria, a double-blinded process was conducted where the 3D-rendered animal scan underwent visual inspection. Secondly, the qualifying data sets were assessed for the image-guided distribution of different tracers for each time point scanned. **Figure 3** gives a simplified 2D projection including the positioning of 3D volume of interest (VOI) areas being #1: an ellipsoid VOI covering the heart muscle, i.e., the cardiac VOI; #2: a cubic VOI for chest/thorax, and #3: a cubic VOI including the full adnominal cavity including all organs (liver, spleen, pancreas, kidneys etc.). For #2

the counts for #1 were subtracted prior to any other calculation. The mean standardized uptake value (SUV) was calculated, which is the average of all counts in the region of interest (**Figure 3; WB**). This value was used as an input data point to draw time-activity curves (TAC) for each injected molecule and route. Finally, the results of the latter assessment were used to compare uptake- TACs of the comparing data set for [^{89}Zr]Zr-DFO-h-R3 and [^{89}Zr]Zr-oxalate. Additionally, [^{64}Cu]Cu-SarAr-h-R3 and [^{64}Cu]Cu-DOTA-h-R3 data sets were compared to [^{64}Cu]Cu-Cl_2. This was done to address objective 1, and literature on the clinical use of h-R3 radiopharmaceuticals was reviewed to support or argue the significance and relevance of the results for this part of the study.

5.2.2 Determining *ex vivo* biodistribution of Zr-89- or Cu-64-radiolabeled h-R3

5.2.2.1 Study inputs

At the conclusion of the imaging study, a selection of organs and tissues (15 in total) from each animal used for micro-PET imaging was made available for further *ex vivo* investigations. This included blood, plasma, heart, lung, spleen, liver, kidneys, small intestine, large intestine, brain, skin, muscle, femur, ovaries, and bladder samples, which were collected from animals either at 6 h or 24 h or 48 h post injection. The radioactivity levels of each organ and tissue were measured using the Wizard 2470 automatic gamma counter (PerkinElmer, USA). In total, 21 data sets (known as *ex vivo* sets) of up to 15 organ measurements were each provided for this study, along with the corresponding counts/min (CPM) values obtained from gamma counting and made available for this study. These data sets were generated to address objective 2 of this study.

5.2.2.2 Study methodology

Each data set obtained included up to 15 measurements of organ CPM, organ weights, time of measurement and, start and end times of measurements. The data obtained from the animal study was analyzed further, starting with activity corrections for both background and radioactive decay. The results were expressed as a percentage of the injected dose (ID) adjusted for organ or tissue weight (%ID/g).

The Tukey's Fences method was applied in this study to identify outliers in the data sets. This calculation is a reliable approach for detecting outliers in univariate distributions, including those that are symmetric or slightly skewed. It employs quartiles, the

interquartile range and boundary criteria derived from deviations from the data's central tendency.[205] The interquartile range (IQR) was calculated using the following equation: IQR = Q3 - Q1. To determine the lower and upper fences, the following equations were utilized:

- Lower fence = Q1 - 1.5 (IQR)
- Upper fence = Q3 + 1.5 (IQR)

Values falling outside the fences were considered outliers.

The median absolute deviation (MAD) method was also employed in this study to identify outliers. This technique is particularly useful when the data set's distribution is not normal. The MAD provides a more dependable measure of dispersion than the standard deviation around the mean, as it is less susceptible to outliers. The MAD is calculated by determining the median of the absolute deviations of individual data points from the overall median of the data set. This approach is less influenced by extreme values than the standard deviation, which can be significantly impacted by outliers.[206] To establish the lower and upper limits, the following equations were used:

- Lower limit = Median – 2.5 (MAD)
- Upper limit = Median + 2.5 (MAD)

The values below or above the limits were considered outliers. A threshold of 2.5 (MAD) is recommended because it strikes a balance between sensitivity to outliers and the risk of excluding valid data points. This threshold is considered a reasonable and moderate option, offering a practical approach to outlier detection that is neither overly conservative nor overly lenient.[206, 207]

5.2.2.3 Study assessment scope

To address the second objective, data was evaluated by comparing all organs within each data set. This allowed for the identification of areas of misdistribution caused by injection route or molecule design for each compound or tracer administration method. For instance, elevated levels of radioactivity in the abdomen or intestines were considered unfavorable, as were high levels in the liver, spleen or bone. The results in this study section were evaluated based on the evidence from clinical studies utilizing radiolabeled h-R3, to support or argue the findings.

5.3 Technological limitations

Technological challenges were reported to the student as part of the data sets provided. The micro-PET images for IV administered [^{64}Cu]$CuCl_2$ were not available, which was an internal control for IV administered [^{64}Cu]Cu-DOTA-h-R3 and [^{64}Cu]Cu-SarAr-h-R3. The results for [^{64}Cu]Cu-DOTA-h-R3 were predicted by the biostatistician to have low statistical power, with only two *ex vivo* biodistribution data sets being available. The micro-CT data was not always available, or the image fusion was deemed of inadequate quality; image analysis therefore relied solely on the reconstructed PET data, which made it difficult to locate and attribute accurate tracer distribution to organs or tissue sections (without anatomical references).

5.4 Ethical approval

The University of Pretoria Research Ethics Committee has previously approved the research protocol of this study, as evidenced by protocol number 355/2023.

6. RESULTS

6.1 Micro-PET image analysis

The data assessment (reconstructed image files) was performed on 117 imaging data sets (as described in the methods; see previous chapter); the results are summarised in Table A1 (see Appendix); 30 scans were excluded for the different reasons stated in the table, yielding n=86 scans for further image analysis.

6.1.1 Organ activity uptake for [^{89}Zr]Zr-DFO-h-R3 (IP versus IV)

[^{89}Zr]Zr-DFO-h-R3 was evaluated for its *in vivo* stability and biodistribution by means of micro-PET imaging at different time points post injection via either the IV or IP route (2 h, 4 h, 6 h, 24 h and 48 h) and compared to micro-PET images displaying [^{89}Zr]Zr-oxalate body distribution (1 h, 2 h, 4 h, 6 h and 24 h post IP injection) (**Figure 4**).

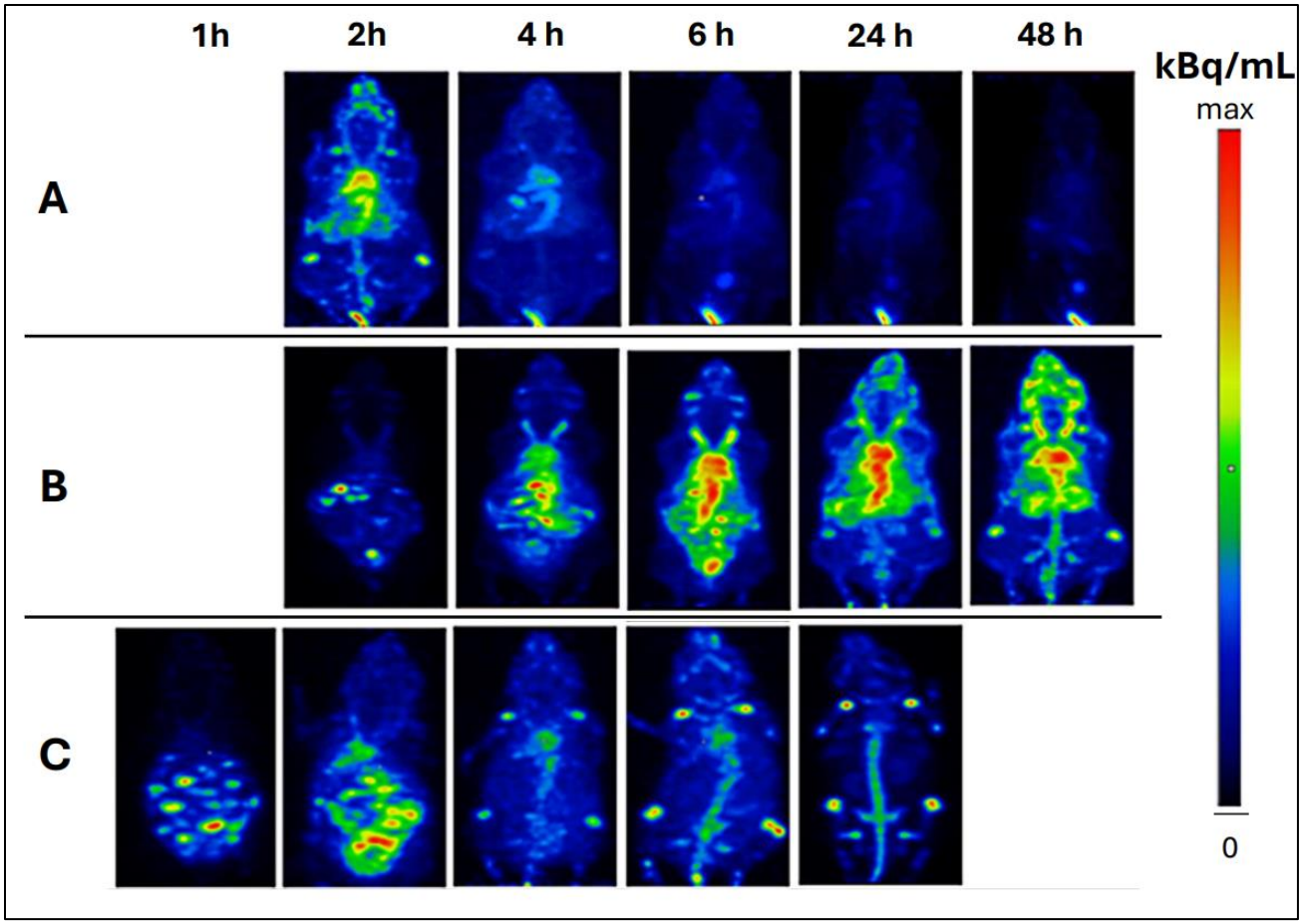

Figure 4: Micro-PET imaging of [^{89}Zr]Zr-DFO-h-R3
Sequential maximum intensity projections (MIP) images aligned head (top) to pelvis (bottom) – two representative data sets of healthy athymic nude mice injected with [^{89}Zr]Zr-DFO-h-R3 given either **A**) intravenously or **B**) intraperitoneally, are displayed. **C**) control, consecutive MIP images of a mouse injected intraperitoneally with [^{89}Zr]Zr-oxalate (pH 7.0). All micro-PET images were acquired at the indicated time points post administration (see top line) and normalized for radioactive decay for comparison. Color scale: signal intensity measured in kBq/ml.

Even in the absence of CT, the MIP images were of sufficient quality to indicate that a characteristic vascular distribution of administered [^{89}Zr]Zr-DFO-h-R3 (IP and IV) as well as [^{89}Zr]Zr-oxalate (IV route) was seen early-on post injection. After 2 h, the uptake of the tracer in the abdomen decreased and started accumulating in the bone. As expected for IV administration, the highest uptake of [^{89}Zr]Zr-DFO-h-R3 was present at the 2 h measured for the heart region followed by washout and diminishing of the signal. Other organ-related uptake of IV given [^{89}Zr]Zr-DFO-h-R3 activity could be identified in the

abdomen (as well as the liver and spleen) but was relatively quickly washed out over time. However, with IP administration of [^{89}Zr]Zr-DFO-h-R3, abdominal activity was visible from 2 h, which remained spread widely in the abdomen up to 6 h post tracer deposition in the abdominal cavity; thereafter onset accumulation in the kidneys occurred between 24 h and 48 h. In the case of [^{89}Zr]Zr-DFO-h-R3 injected intravenously, activity in the tail was visible as early as 2 h after administration, which remained throughout 48 h. Very little activity could be seen in the rest of the mouse at 2 h to 6 h post administration, indicating that most [^{89}Zr]Zr-DFO-h-R3 remained in the tail and only spread to other organs at later time points. These MIP images of [^{89}Zr]Zr-DFO-h-R3 administered both intravenously and intraperitoneally showed that the bone began to take up tracer at 24 h post injection (PI), with increased uptake observed at 48 h after injection.

The presence of IV given [^{89}Zr]Zr-oxalate in the cardiac region was quite low but remained visible up to the final scan (24 h PI). By being deposited as a bolus in an abdominal area [^{89}Zr]Zr-oxalate was most prevalent in the abdomen between 1 to 2 h, particularly at the IP site of injection. Increasing uptake of [^{89}Zr]Zr-oxalate in the bone was observed from as early as 4 h with the signal becoming most vivid at the endpoint imaging at 24 h, where avid activity accumulating is also visible in the spine and hip bone region.

Image quantification of the *in vivo* tracer biodistribution was performed on the micro-PET images obtained from the mice injected either with [^{89}Zr]Zr-oxalate intraperitoneally, [^{89}Zr]Zr-DFO-h-R3 intraperitoneally or [^{89}Zr]Zr-DFO-h-R3 intravenously. Image analysis was performed in three areas of interest. The tracer concentrations were hereby determined by way of drawing a 3D preset over the abdominal areal, chest/thorax and the cardiac (heart) region followed by image-guided calculations of the tracer concentration in these selected areas (standard SUV mean (kBq/mL) → SUV-based time-activity curves (TACs; see methods)) (**Figure 5** and **Figure 6**). An overall (whole body) concentration of the tracer / route was calculated as well.

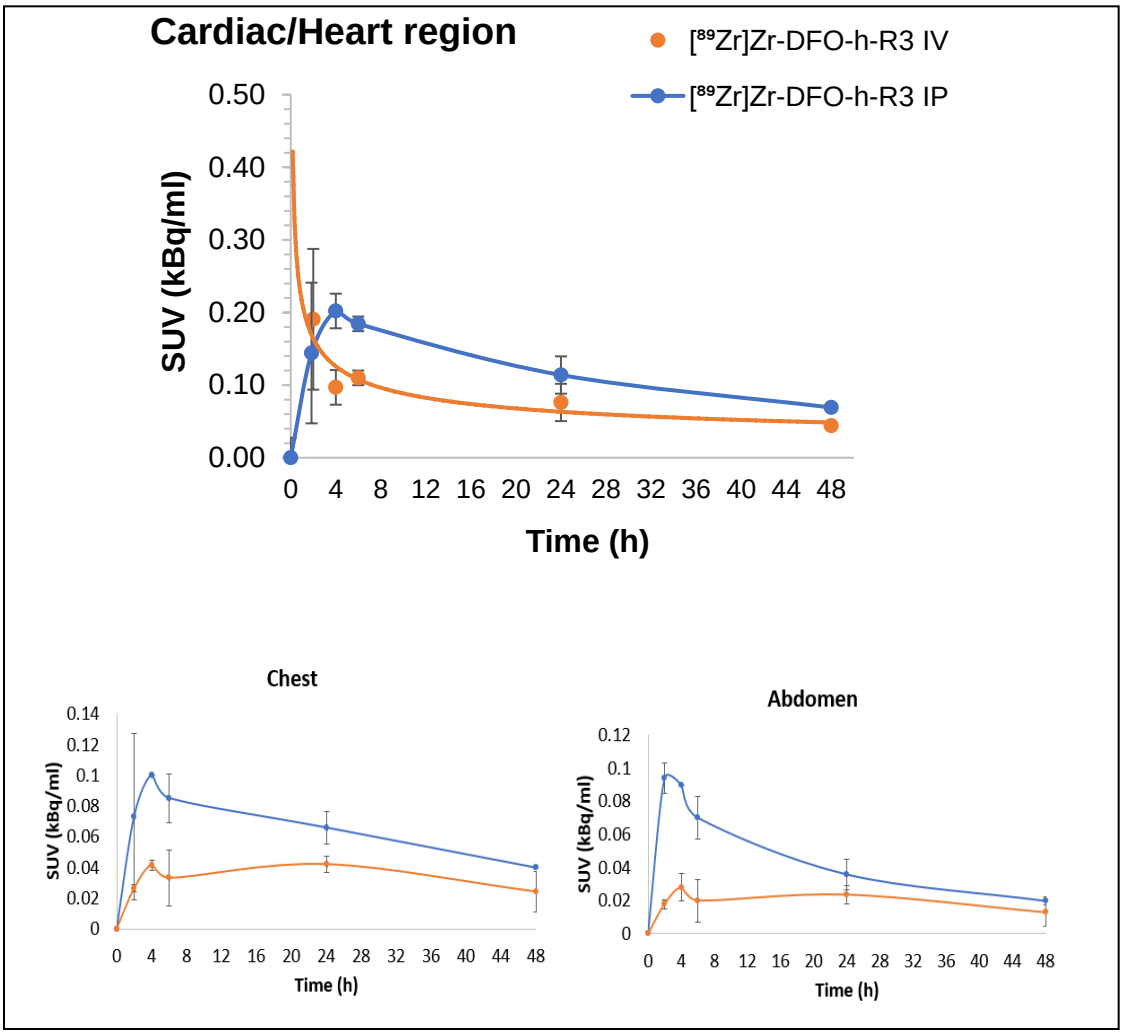

Figure 5: Image quantification for [^{89}Zr]Zr-DFO-h-R3
Time-activity curves representing the concentration of [^{89}Zr]Zr-DFO-h-R3 in three distinct regions within healthy mice. The reconstructed images were subjected to cubic 3D-VOI analysis delineating the cardiac region, chest/thorax area, and the abdominal cavity, thereby obtaining comparable SUV mean values (kBq/ml). Results are displayed as TAC of mean SUV ± sem (IV: n=3; IP: n=2).

The extrapolation of TAC for [^{89}Zr]Zr-DFO-h-R3 enabled the determination of the maximum concentration following IV administration at T_0, with is a calculated B_{max} of 0.24 ± 0.01 kBq/mL. In the other two regions (chest, abdomen), the activity reached a maximum concentration of 4 h after IP and IV tracer administration, respectively. The activity decreased significantly in the cardiac region from 2 h to 4 h after IV administration (P = 0.003), as well as in the chest from 2 h to 4 h post IV administration (P = 0.043). No statistically significant differences were observed in the abdomen and the whole body of

mice injected intravenously between the various time points (2 h, 4 h, 6 h, 24 h and 48 h) ($P > 0.05$).

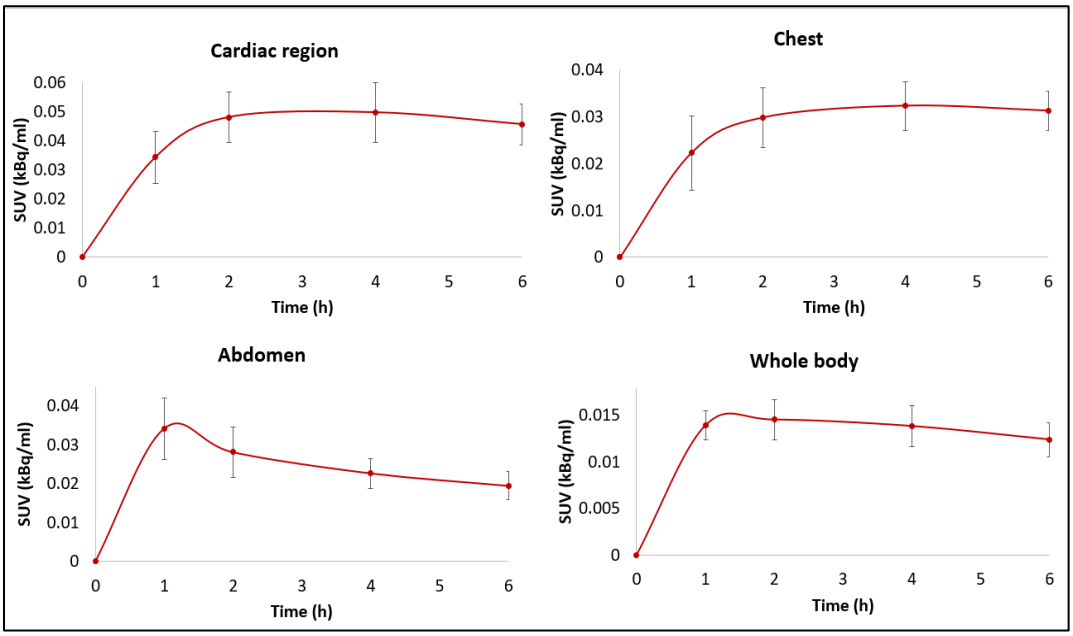

Figure 6: Time-activity curves derived from image analysis.
VOI analysis of micro-PET images obtained of the mice injected intraperitoneally with [^{89}Zr]Zr-oxalate. Reconstructed micro-PET images from mice were subjected to 3D-VOI analysis for the cardiac region, chest, abdomen, and whole body that allowed SUV values (kBq/ml). Results are displayed as mean SUV ± sem (n=4).

The results for IP administered [^{89}Zr]Zr-DFO-h-R3 indicated that the difference between the level of activity in the cardiac region 4 h after injection and 24 h was statistically significant ($P = 0.048$). The initial activity detected in the abdomen 2 h post administration decreased to approximately 50% calculated at 24 h ($P = 0.025$) and decreased four times by 48 h ($P = 0.040$), showing a significant wash out of the tracer from the area. However, there were no statistically significant differences found in either the chest or whole body at any time point. The [^{89}Zr]Zr-oxalate-micro-PET images were additionally utilized to perform a quantitative assessment of the *in vivo* distribution of the tracer in different regions, including the entire body, abdomen, chest and cardiac using standard SUVs and VOI-based time-activity curves (**Figure 6**). The concentration of [^{89}Zr]Zr-oxalate in the abdominal area peaked at 1 h PI (0.034 ± 0.008 kBq/ml) and significantly decreased until

6 h PI (P = 0.025). However, the differences between the time points in the whole body, chest and cardiac regions were not statistically significant.

6.1.2 Image analysis and organ uptake of ^{64}Cu-labeled h-R3

Distribution data for [^{64}Cu]Cu-DOTA-h-R3 and [^{64}Cu]Cu-SarAr-h-R3, administered intravenously to healthy athymic nude mice, was acquired using a maximum intensity projection (MIPs). Micro-PET scans were conducted at 2 h, 4 h, 6 h and 24 h after injection. The distribution of the ^{64}Cu-labeled h-R3 tracers were compared to that of [^{64}Cu]Cu-Cl_2 (administered intraperitoneally) in mice by means of micro-PET scans performed 1 h, 2 h, 4 h and 6 h following administration (**Figure 7**).

Despite the absence of CT imaging occurring for some scanning procedures, already 4 h PI, clear differences in biodistribution/ concentration of ^{64}Cu-labeled h-R3 could be seen when different chelators were used for radiolabeling. The MIP images indicated high concentration of [^{64}Cu]Cu-SarAr-h-R3 in the abdomen, particularly in the spleen and liver from 4 h to 24 h after injection. Concerning the cardiac radioactivity at four and 24 h [^{64}Cu]Cu-SarAr-h-R3 > [^{64}Cu]Cu-DOTA-h-R3. After 24 h, the concentration of [^{64}Cu]Cu-SarAr-h-R3 observed in the liver remained high, while the concentration in the spleen also remained high. [^{64}Cu]Cu-DOTA-h-R3 activity increased over time in the liver up to 24 h. The highest concentration of [^{64}Cu]Cu-Cl_2 was observed at 1 h PI in the abdomen (mostly in the injection site/ IP site), with a subsequent decrease in concentration as time elapsed.

Regarding PET-image guided quantification of the *in vivo* tracer distribution, the concentration for [^{64}Cu]Cu-SarAr-h-R3 was compared to that of [^{64}Cu]Cu-DOTA-h-R3 over time in three areas (cardiac/heart; chest/thorax; abdomen) using standard SUVs and VOI-based time-activity curves (**Figure 8**).

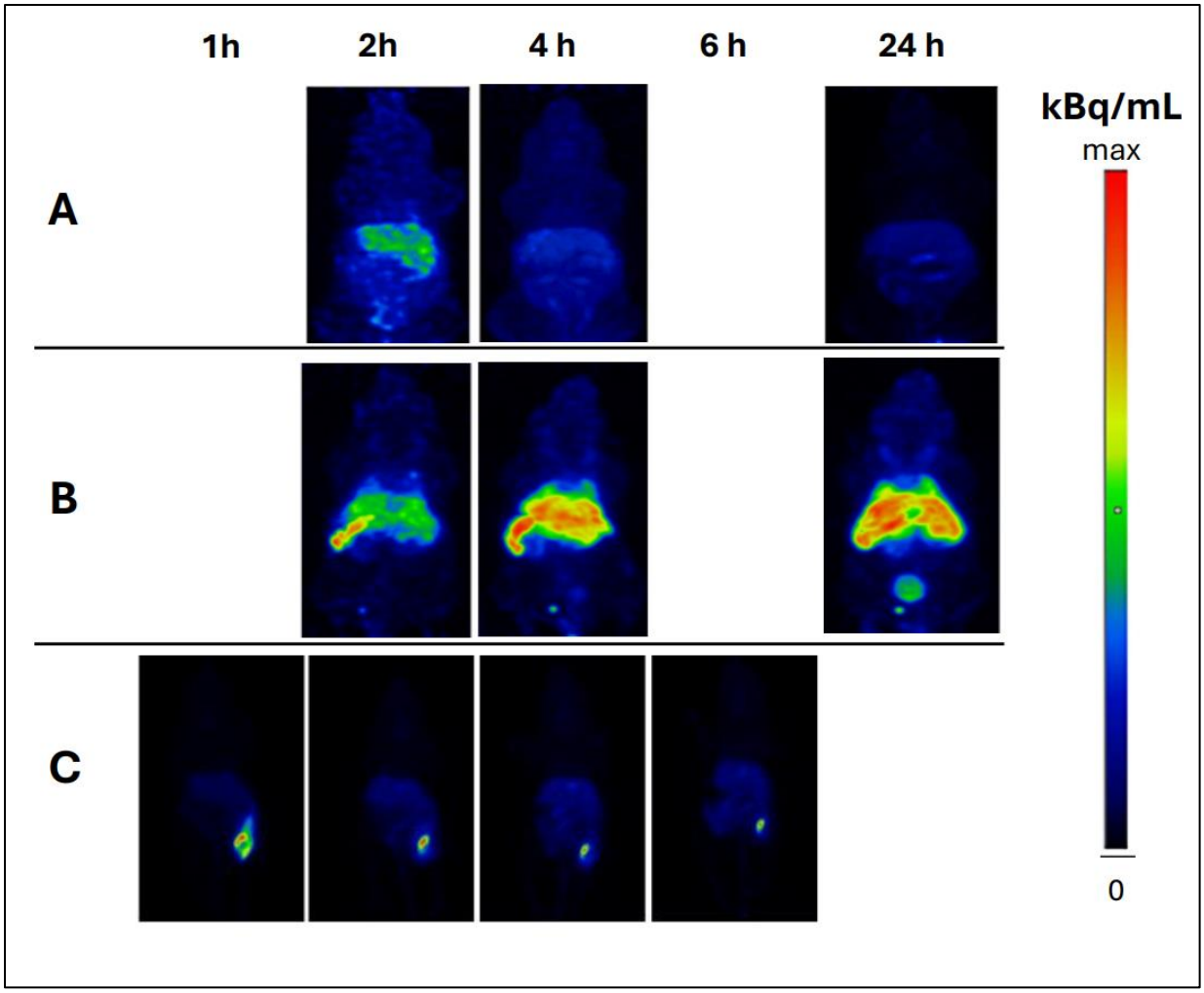

Figure 7: Micro-PET imaging of [^{64}Cu]Cu-DOTA-h-R3 and [^{64}Cu]Cu-SarAr-h-R3.
The MIP of representative healthy athymic nude mice injected IV either with **A**) [^{64}Cu]Cu-DOTA-h-R3 (ID = 6.56 MBq) or **B**) [^{64}Cu]Cu-SarAr-h-R3 (ID = 10.04) as well as **C**) a control animal injected IP with of [^{64}Cu]$CuCl_2$ (29.02 MBq). All micro-PET images were acquired at the indicated time points post administration (see top line) and normalized for radioactive decay for comparison. Color scale: signal intensity measured in kBq/ml.

As before, the standard deviation, mean, and coefficients of variation were calculated. The CV was used to assess the SD in comparison to the mean and to determine if the SD was high or low (Tables A8 and A10).

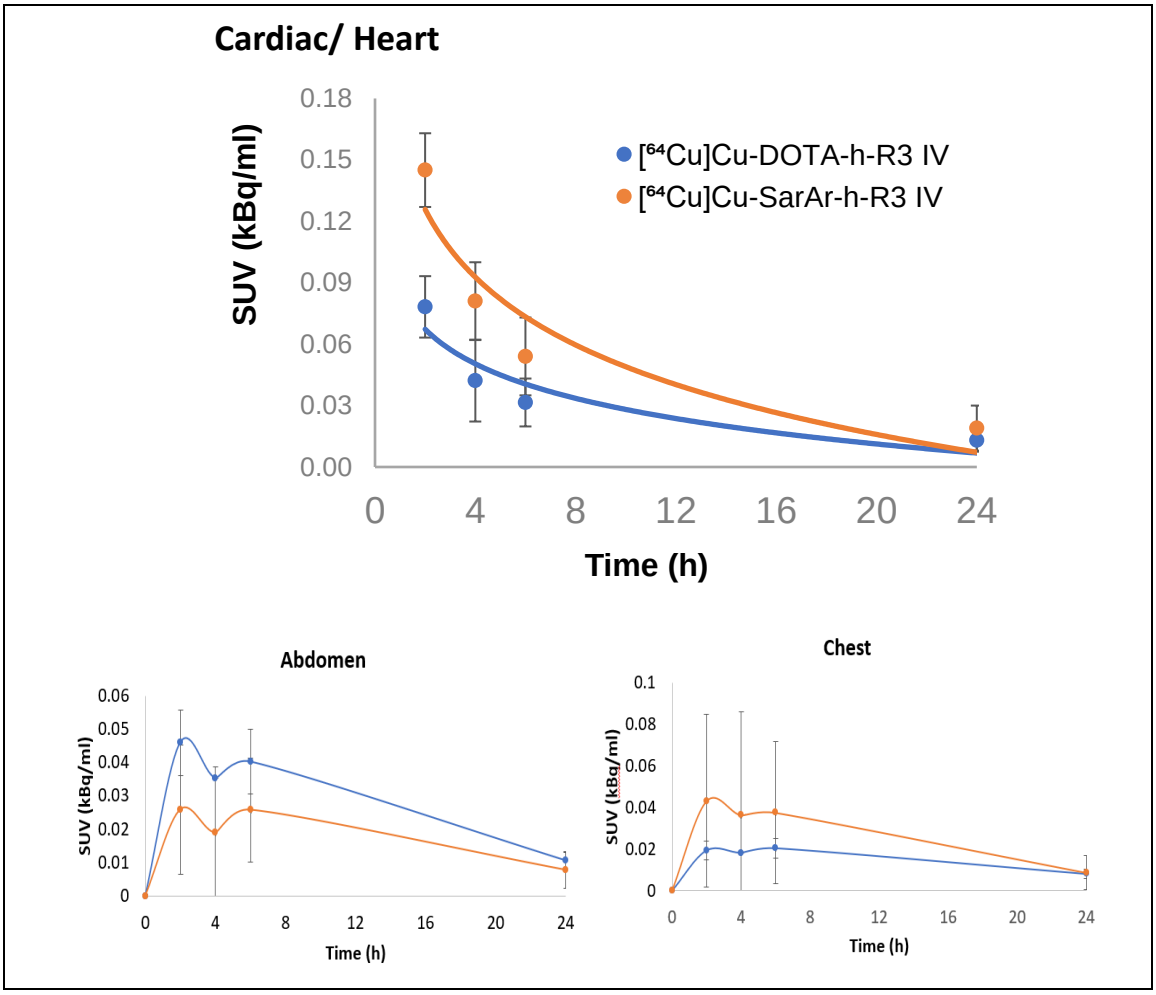

Figure 8: Time-activity curves for [^{64}Cu]Cu-DOTA-h-R3 and [^{64}Cu]Cu-SarAr-h-R3. Display of [^{64}Cu]Cu-DOTA-h-R3 (blue; n=2) and [^{64}Cu]Cu-SarAr-h-R3 (orange; n=4) concentration over time in various regions of healthy mice. The reconstructed images underwent a 3D-VOI analysis delineating cardiac region, chest and abdomen, providing SUV values (kBq/ml). Results are displayed as mean SUV ± sem.

The CV values for the cardiac region, chest abdomen at 2 h, 4h, 6 h and 24 h for [^{64}Cu]Cu-DOTA-h-R3 were all less <1 (at 4 h, the SD, mean and coefficient of variation were not calculated due n=1) (Table A8). The CV values for [^{64}Cu]Cu-SarAr-h-R3 were consistently <1 in all regions at all times points, except at 4 h as the SD was higher than the mean, suggesting that the data points were highly dispersed at this time point (Table A10). For [^{64}Cu]Cu-DOTA-h-R3 and [^{64}Cu]Cu-SarAr-h-R3, the differences observed between all the time points (cardiac, chest, abdomen) were not statistically significant (refer to Tables A9 and A11 for *P*-values). Additionally, the *in vivo* distribution of [^{64}Cu]Cu-Cl_2 was quantified

from the micro-PET images as well. Standard SUVs and VOI-based time-activity curves were employed to determine the concentrations of the tracer in different anatomical regions, including the whole body, abdomen, chest and cardiac area (**Figure 9**).

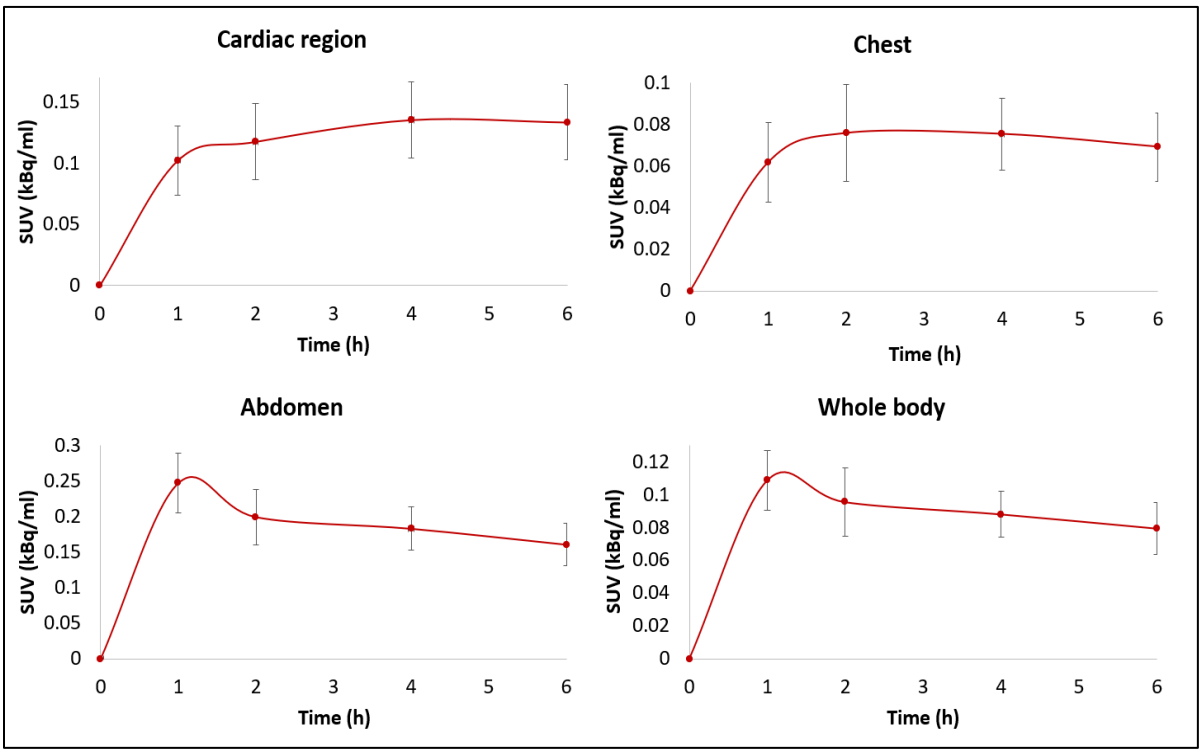

Figure 9: PET image derived time-activity curves for [^{64}Cu]Cu-Cl_2.
Time-activity curves derived from a 3D-VOI analysis of micro-PET images obtained of the mice injected IP with [^{64}Cu]Cu-Cl_2. Reconstructed images (n=6) were subjected to SUV (kBq/ml) quantification for the cardiac region, chest and abdomen for each time point. Results are displayed as mean SUV ± sem.

All values for mean, standard deviation and coefficients of variation are presented in Table A12. The low CV indicate that the data points were not spread out widely, as the SD was low and less than the mean in all the regions and time points.

The results of the study showed that the activity present in the abdomen was substantially higher at the 1 h time point compared to the 4 h time point after administration (P = 0.014; please see Table A13 for P-values). Additionally, the activity present in the abdomen 1 h PI was significantly higher than at 6 h (P = 0.003). Similarly, the difference between activities available in the whole body at 1 h and 6 h after administration was also found to

be statistically significant ($P = 0.019$). However, no statistically significant differences were observed between the time points in the cardiac region and chest.

6.2 *Ex vivo* biodistribution analysis

To validate the results from the micro-PET image analysis, endpoint biodistribution studies were available that related to measurement of each organ-based radioactivity *ex vivo*. Various organs/tissues were therefore dissected, weighed and the activity on organs/tissues was determined by sensitive gamma counting. For this project, this data was further analyzed. Corrections for background, activity decay, and non-injected tracer were carried out whereafter the results were expressed in relation to the injected dose (ID) and adjusted for organ/tissue weight (%ID/g). The results were reported as a percentage of the injected dose per gram (%ID/g) of organ or tissue. Organs or tissues displaying an activity level of 1% ID/g were regarded as having a negligible activity level, whereas those with <5% ID/g were seen as possessing moderate but acceptable amount of activity. Organs or tissues showing the activity level of 10% ID/g were considered to have elevated levels of activity.

6.2.1 *Ex vivo* biodistribution of [^{89}Zr]Zr-DFO-h-R3

To compare how the different routes of administration would influence the biodistribution of [^{89}Zr]Zr-DFO-h-R3, endpoint measurements from various organs and tissues was determined at 48 h after intravenous or intraperitoneal [^{89}Zr]Zr-DFO-h-R3 injections (**Figure 10**) (please see Tables A14 for biodistribution data and *P*-values). The results indicate that for IV administered [^{89}Zr]Zr-DFO-h-R3, the highest tracer concentration was present in the plasma, with an activity level of 19.18 ± 0.86 %ID/g, followed by kidneys (9.21± 0.23 %ID/g), the lungs (6.23 ± 1.01 %ID/g), the heart (5.71 ± 0.04 %ID/g), the bladder (5.09 ± 2.88 %ID/g) and the skin (5.08 ± 0.24 %ID/g). The activities of other organs and tissues were less than 5 %ID/g.

At 48 h after IP administered [^{89}Zr]Zr-DFO-h-R3 the results showed similarities in organ distribution, the plasma exhibited the highest level of [^{89}Zr]Zr-DFO-h-R3 uptake, with an activity of 19.97 ± 1.05 %ID/g. This was followed by the kidneys with an activity of 10.36 ± 1.21 %ID/g, the lungs (7.02 ± 3.15 %ID/g), the spleen (6.55 ± 2.38 %ID/g), the bladder

(6.54 ± 2.94 %ID/g), skin (5.15 ± 0.47 %ID/g) and bone (femur 5.46 ± 2.29 %ID/g). The remaining tissues and organs had activity levels <5 %ID/g.

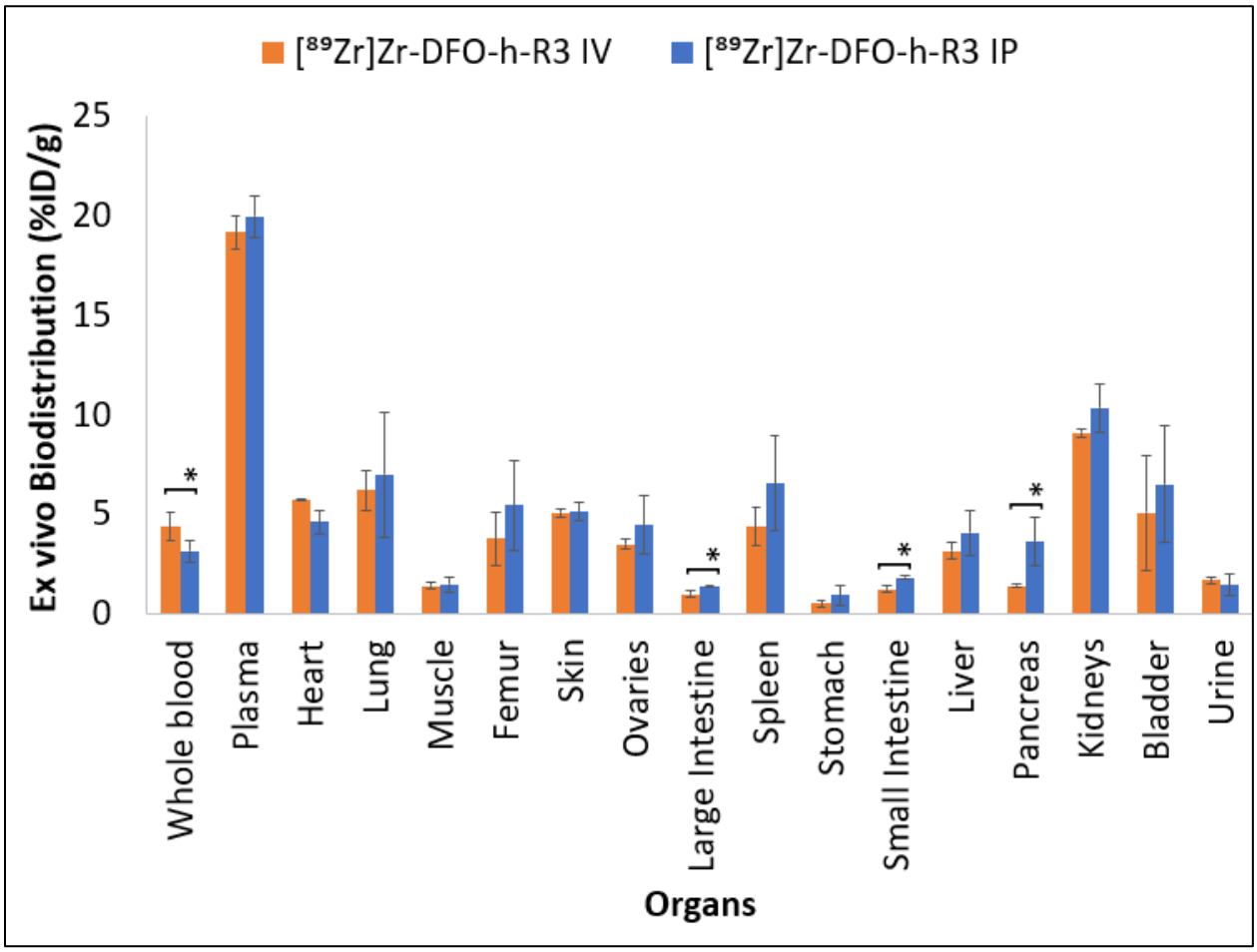

Figure 10: *Ex vivo* biodistribution of [^{89}Zr]Zr-DFO-h-R3.
[^{89}Zr]Zr-DFO-h-R3 was administered to healthy mice intravenously (n=5) or intraperitoneally (n=4). The mice were euthanized at 48 h post injection and relevant organs were collected and underwent gamma counting. Results are expressed as the mean percentage of injected dose per gram of each organ (%ID/g) ± SD. Student's *t*-test was performed to determine statistically significant differences between the two administration routes (*P < 0.05).

The statistical analysis revealed significant differences between IV and IP administration of [^{89}Zr]Zr-DFO-h-R3 in some organs. The activity was significantly higher for the IV injection route concerning whole blood (P = 0.031), whilst the activity in the large (P =

0.004) and small intestine (P = 0.001), as well as the pancreas (P = 0.033) demonstrated significantly higher activity levels for the IP route *vs* IV injection of the tracer. Notably, the radioactivity observed in the pancreas following IP administration was <5%ID/g but approximately twice the level observed after IV injection.

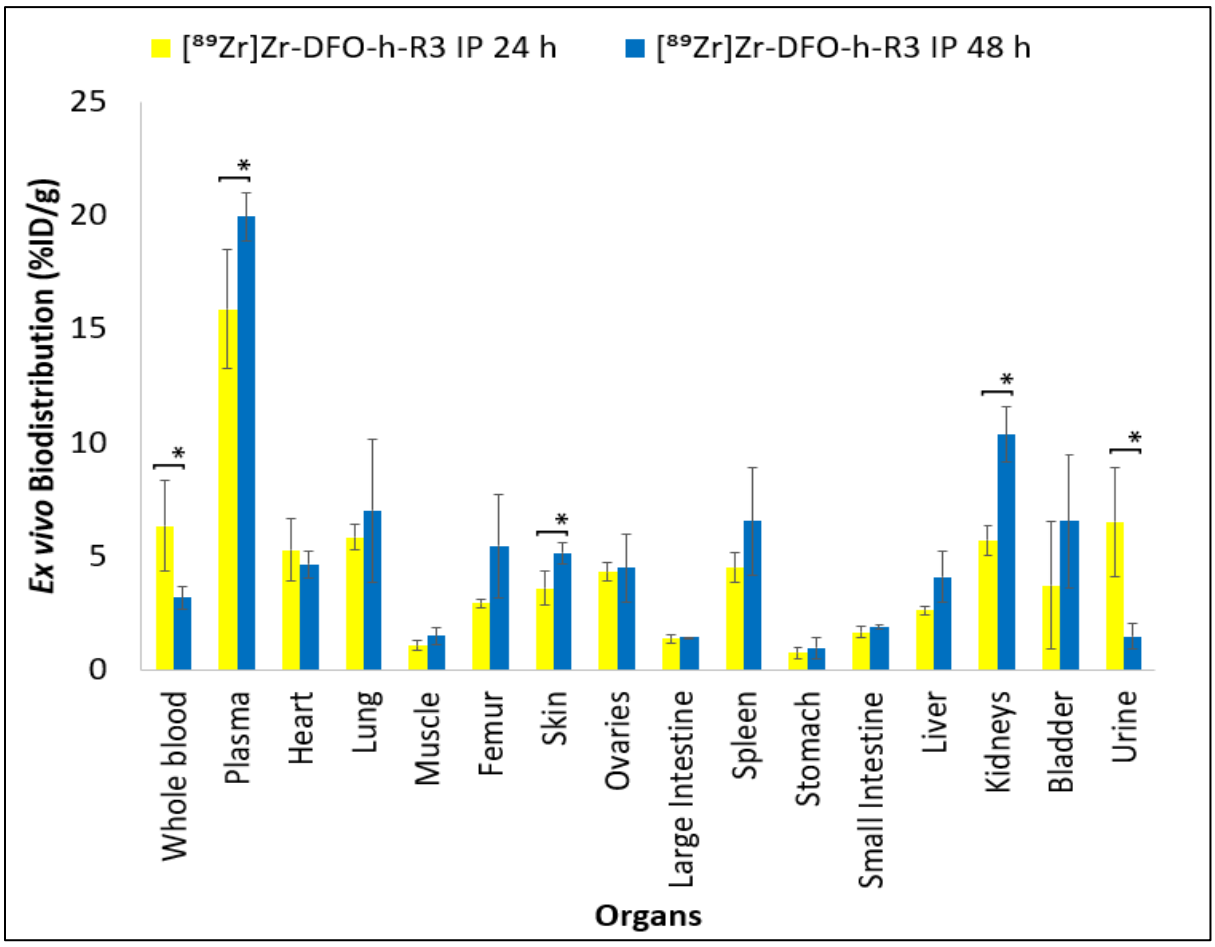

Figure 11: Extended *ex vivo* biodistribution of IP administered [^{89}Zr]Zr-DFO-h-R3. Healthy mice received [^{89}Zr]Zr-DFO-h-R3 and were euthanized at 24 h (n=6) or 48 h (n=4) post injection. Relevant organs were collected and underwent sensitive gamma counting. Results are expressed as the mean percentage of injected dose per gram of each organ (%ID/g) ± SD. Student's *t*-test was performed to determine statistically significant differences between the two administration routes (*P < 0.05).

To further evaluate any delayed uptake or altered clearance over time, the biodistribution of IP injected [^{89}Zr]Zr-DFO-h-R3 in various organs/tissues from 24 h was compared with

results from the organs dissected at 48 h after IP administration (**Figure 11**) (refer to Tables A15 for the biodistribution data and *P*-values).

The radioactivity of [^{89}Zr]Zr-DFO-h-R3 found in whole blood decreased significantly from 6.33 ± 2.00 %ID/g at 24 h to 3.17 ± 0.52 %ID/g at 48 h (P = 0.046). However, the radioactivity of the compound in the plasma was found to be significantly higher at 48 h (19.97 ± 1.05%ID/g) compared to 24 h (15.90 ± 2.61%ID/g; P = 0.045); which may have caused increased levels of [^{89}Zr]Zr-DFO-h-R3 in other organs (insignificantly but now >5%) after 48 h when IP injected.

The activity levels of IP injected [^{89}Zr]Zr-DFO-h-R3 were found significantly higher in the skin (P = 0.016) and kidneys (P = 0.003) after 48 h of administration compared to the concentration found at 24 h. Additionally, the radioactivity of [^{89}Zr]Zr-DFO-h-R3 in the urine was four times lower at 48 h (P = 0.020) as compared to 24 h. Uptake in the abdominal organs (intestines and ovaries) remained favorably-low at about 2 %ID/g.

Ex vivo biodistribution of any ^{89}Zr-labeled compound may be compared to that of [^{89}Zr]Zr-oxalate to further study its potential as imaging agent. Therefore, organ distribution of the negative reference (control) [^{89}Zr]Zr-oxalate (24 h post IP administration) was compared to that of [^{89}Zr]Zr-DFO-h-R3 (**Figure 12**) (please see Tables A16 for biodistribution data and *P*-values).

The femur (bone) exhibited the peak activity level (17.28 ± 4.34 %ID/g), which was five-fold higher compared to the bone uptake from mice injected with [^{89}Zr]Zr-DFO-h-R3 (2.92 ± 0.19 %ID/g; P = 0.001). As [^{89}Zr]Zr-oxalate's biodistribution would be similar to uncomplexed ^{89}Zr-metal ions, which is known to predominantly target the bone,[208] the low bone uptake of [^{89}Zr]Zr-DFO-h-R3 indicated that the complex was stable *in vivo* with negligible amounts of complexed ^{89}Zr dissociating from the DFO-h-R3 conjugate. IP injected [^{89}Zr]Zr-oxalate caused elevated renal uptake (7.25 ± 2.53 %ID/g); however, radioactivity measured in other organs and tissues were < 5 %ID/g.

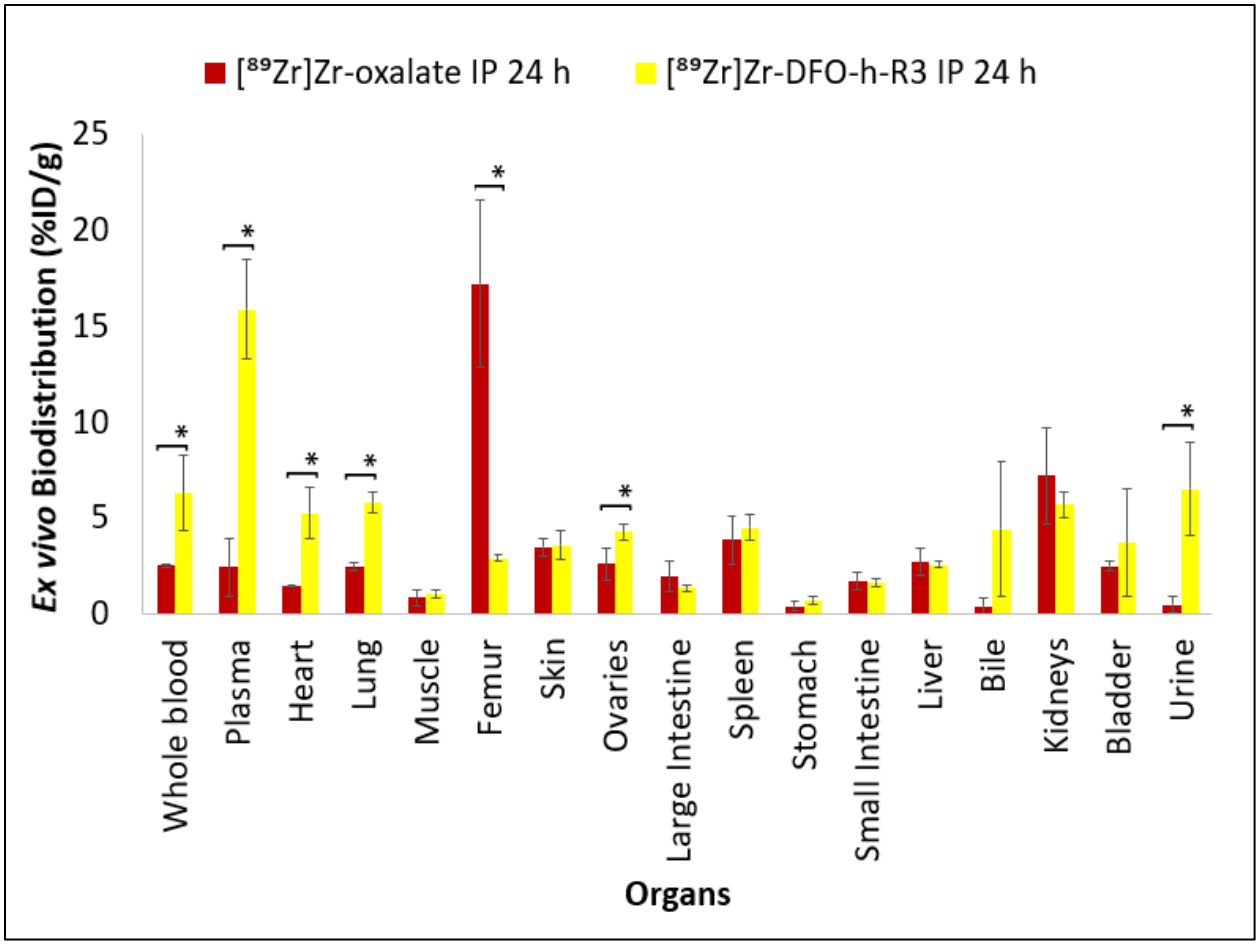

Figure 12: *Ex vivo* biodistribution of [^{89}Zr]Zr-oxalate and [^{89}Zr]Zr-DFO-h-R3.
Healthy mice were injected intraperitoneally either with [^{89}Zr]Zr-oxalate (n=6) or [^{89}Zr]Zr-DFO-h-R3 (n=6). The mice were euthanized 24 h post injection and relevant organs were collected and underwent sensitive gamma counting. Results are expressed as percentage of injected dose per gram of each organ (%ID/g) ± SD. Student's *t*-test was performed to determine statistically significant differences between [^{89}Zr]Zr-oxalate and [^{89}Zr]Zr-DFO-h-R3 (*P < 0.05).

Compared to [^{89}Zr]Zr-oxalate the statistical analysis for [^{89}Zr]Zr-DFO-h-R3 revealed thirteen times higher urinary uptake (P = 0.014), six times higher plasma uptake (P = 0.0004), three times higher kidney (P= 0.002) and heart uptake (P = 0.011) as well as a two-fold higher uptake seen for in whole blood (P = 0.032) and the lungs (P = 0.001). The remaining organs and tissues exhibited activity levels <5 %ID/g.

6.2.2 *Ex vivo* biodistribution of ^{64}Cu-labeled h-R3

To confirm the outcome from both the [^{64}Cu]Cu-DOTA-h-R3 and [^{64}Cu]Cu-SarAr-h-R3 micro-PET image analyses, *ex vivo* endpoint biodistribution studies were conducted. Using different metal chelators may reflect in an altered organ distribution of the respective radioconjugate. Therefore, data was available to compare the biodistribution of IV administered [^{64}Cu]Cu-DOTA-h-R3 or [^{64}Cu]Cu-SarAr-h-R3 in various organs and tissues at 24 h post injection (**Figure 13**; please refer to Tables A17 for biodistribution data and *P*-values).

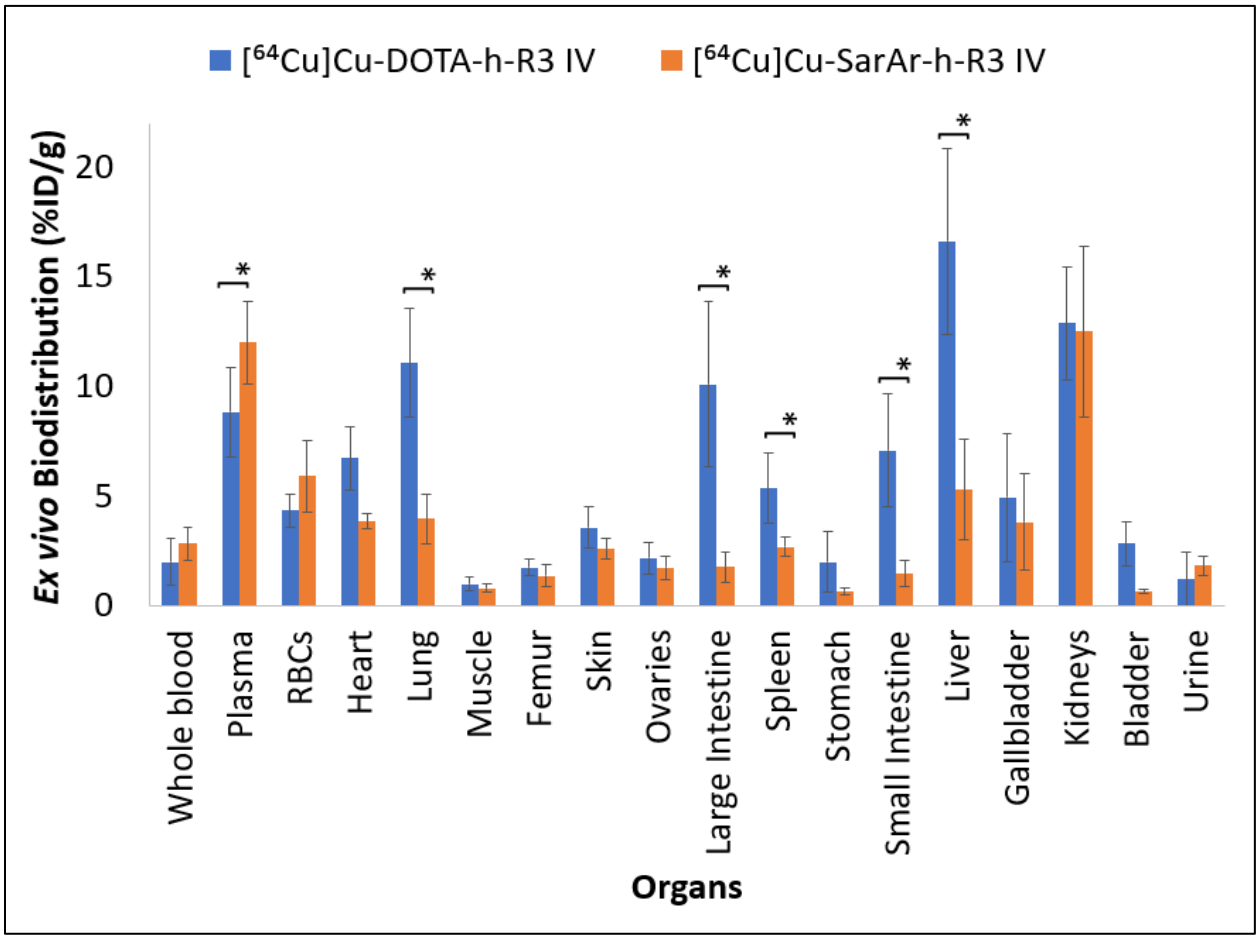

Figure 13: Ex vivo biodistribution of [^{64}Cu]Cu-DOTA-h-R3 and [^{64}Cu]Cu-SarAr-h-R3. Healthy mice were intravenously injected with either [^{64}Cu]Cu-DOTA-h-R3 (n=4) or [^{64}Cu]Cu-SarAr-h-R3 (n=6). The mice were euthanized 24 h post injection and relevant organs were collected which underwent sensitive gamma counting. Results are expressed as percentage of injected dose per gram of each organ (%ID/g) ± SD. Student's *t*-test was performed to determine statistically significant differences

between [^{64}Cu]Cu-DOTA-h-R3 and [^{64}Cu]Cu-SarAr-h-R3 (*P < 0.05). Red blood cells (RBCs).

The liver displayed the highest accumulation of radioactivity of [^{64}Cu]Cu-DOTA-h-R3 (16.62 ± 4.24 %ID/g), significantly higher than that of [^{64}Cu]Cu-SarAr-h-R3 (5.29 ± 2.31 %ID/g; P = 0.006). Similarly, [^{64}Cu]Cu-DOTA-h-R3 was found to be five times higher in the large intestine (P = 0.021), four times larger in the small intestine (P = 0.021) and two times higher in the lungs (P = 0.006). The splenic uptake of [^{64}Cu]Cu-DOTA-h-R3 was approximately 5 %ID/g but was significantly higher than [^{64}Cu]Cu-SarAr-h-R3 (P = 0.039). In contrast, the only significantly higher accumulation of [^{64}Cu]Cu-SarAr-h-R3 compared to [^{64}Cu]Cu-DOTA-h-R3 was found in plasma (P = 0.047).

After the liver, maximal uptake of [^{64}Cu]Cu-DOTA-h-R3 was observed in the kidneys (12.87 ± 2.60 %ID/g), followed by the lungs (11.07 ± 2.49 %ID/g), large intestine (10.10 ± 3.79 %ID/g), plasma (8.84 ± 2.04 %ID/g), small intestine (7.09 ± 2.60 %ID/g), heart (6.72 ± 1.46 %ID/g) and spleen (5.35 ± 1.58 %ID/g). Other organs and tissues showed radioactivity uptake <5 %ID/g. For [^{64}Cu]Cu-SarAr-h-R3, the kidneys showed the highest level of activity measured at 12.51 ± 3.89 %ID/g, followed by the plasma (12.01 ± 1.89 %ID/g), the red blood cells (RBCs; 5.92 ± 1.62 %ID/g) and the liver (5.29 ± 2.31 %ID/g). Other organs and tissues had activity < 5 %ID/g.

[^{64}Cu]Cu-Cl_2 served as a control compound to mimic any eventual distribution of copper-64 that may leak from the chelator. Furthermore, the *ex vivo* distribution of [^{64}Cu]Cu-Cl_2 after different routes of administration was determined in various organs and tissues 6 hours after administration (**Figure 14**; please refer to Tables A18 for biodistribution data and P-values). Highly significant differences (P <0.001) between [^{64}Cu]Cu-Cl_2 administered IP and IV were observed for the liver (IP: 32.88 ± 1.33 %ID/g vs. IV: 6.19 ± 2.05 %ID/g;), the large intestine (IP: 27.80 ± 1.90 %ID/g *vs*. IV: 5.52 ± 3.32 %ID/g), the small intestine (IP: 19.24 ± 4.26 %ID/g *vs*. IV: 3.94 ± 0.43 %ID/g) the femur (4.61 ± 0.41 %ID/g *vs*. 2.82 ± 0.36 %ID/g) and muscle tissue (1.95 ± 0.22 %ID/g *vs*. 1.12 ± 0.27 %ID/g).

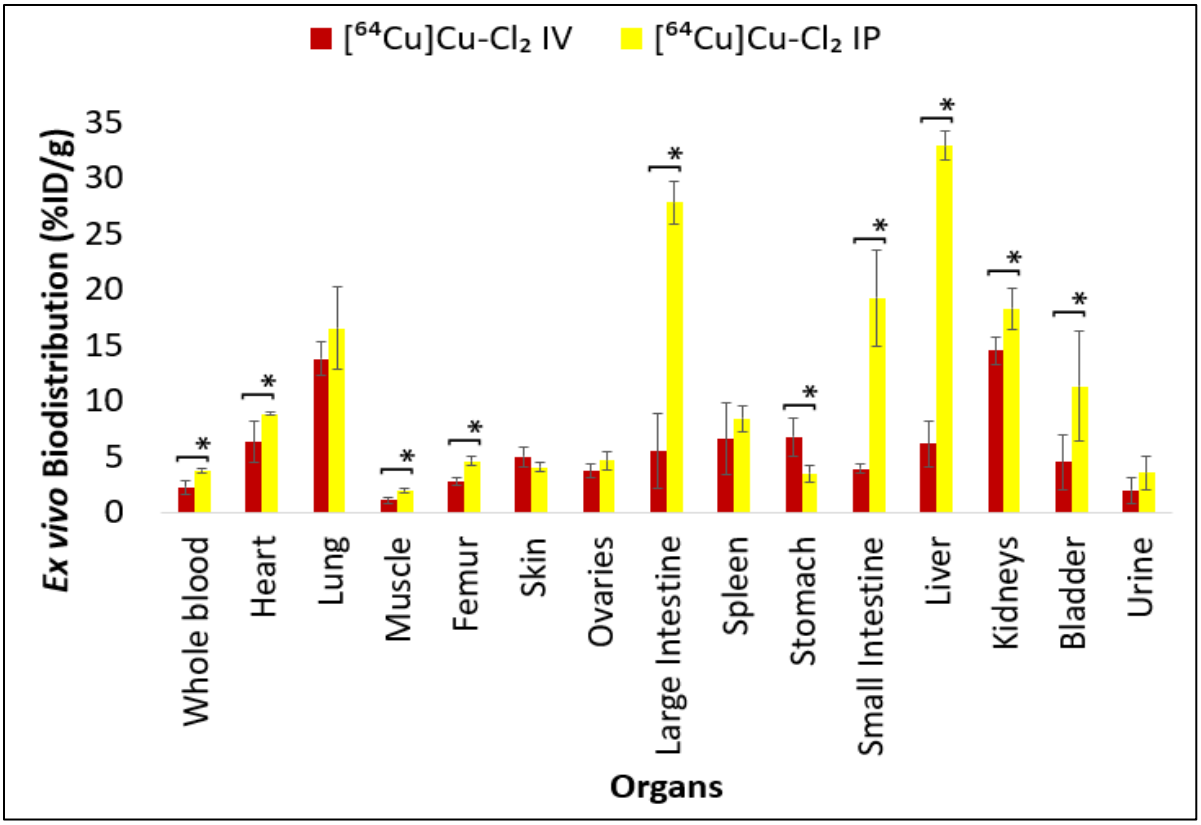

Figure 14: *Ex vivo* biodistribution of [^{64}Cu]Cu-Cl$_2$.
[^{64}Cu]Cu-Cl$_2$ was administered either IV (n=6) or IP (n=6) in healthy mice. The mice were euthanized 6 h post injection and organs were collected and subsequently underwent gamma counting. Results are expressed as a percentage of injected dose per gram of each organ (%ID/g) ±SD. Student's *t*-test was performed to determine statistically significant differences between the two administration routes (*$P < 0.05$).

In addition, higher uptake values were found in the following organs after IP injected [^{64}Cu]Cu-Cl$_2$ compared to its IV injection:

- Kidneys IP (18.28 ± 1.84 %ID/g *vs.* IV 14.52 ± 1.23 %ID/g; P = **0.006**),
- lungs IP (16.53 ± 3.66 %ID/g *vs.* IV 13.79 ± 1.52 %ID/g; P = 0.140),
- bladder IP (11.35 ± 4.96 %ID/g *vs.* IV 4.53 ± 2.44 %ID/g; P = **0.018**),
- whole blood IP (3.80 ± 0.19 %ID/g *vs.* IV 2.28 ± 0.60 %ID/g; P = **0.003**),
- heart IP (8.86 ± 0.11 %ID/g *vs.* IV 6.36 ± 1.86 %ID/g; P = **0.022**),
- and spleen IP (8.44 ± 1.14 %ID/g *vs.* IV 6.60 ± 3.23 %ID/g; P = 0.282).

Notably, the radioactivity levels of IP administered [^{64}Cu]Cu-Cl$_2$ were found to be four to five times in intestinal area compared to IV administration. Only the stomach had higher activity of [^{64}Cu]Cu-Cl$_2$ in IV *vs.* IP administration. Despite the different injection routes

organ uptake remained favourably-low (<5%ID/g) concerning ovaries, femur, skin, whole blood, muscle and in urine.

7. DISCUSSION

Intravenous administration refers to the direct injection of compounds into the circulatory system via a vein. Once inside the bloodstream, the compound is distributed throughout the body via the circulatory system to all tissues within the body.[7, 209, 210] IP administration is a method of delivering compounds directly into the peritoneal cavity, which can lead to high concentrations within the peritoneal space while minimizing systemic drug concentrations.[196, 202] The primary route of absorption for substances administered intraperitoneally is through the mesenteric vessels, which drain into the portal vein and pass through the liver.[196] This route of administration may result in hepatic metabolism of substances before they enter the systemic circulation.[203] The absorption of compounds administered IP is generally different than that of intravenous injections [211]; however, it is subject to research to consider alternate injection routes, for example considering during validation of radiopharmaceuticals for translating to clinics. Especially, the usage of radiometal-radiotracers is expanding. Despite all progress in the field, for example DFO, a widely-used chelator for ^{89}Zr inherently suffers from inadequate stability *in vivo* and results in unspecific association of the radiometal to bones.[160] This was further demonstrated by the injection of [^{89}Zr]Zr-oxalate, which exhibited behavior similar to that of free ^{89}Zr ions, showing a strong affinity for bone. Using this in the present study, suggests the significantly higher uptake observed in the femur upon administering [^{89}Zr]Zr-oxalate compared to [^{89}Zr]Zr-DFO-h-R3. The oxalate form facilitates zirconium's binding to bone, leading to an eight-fold increase in radioactivity in the femur ($P = 0.0002$).

In addition to different administration routes, the influence of metabolic processes in the body on the distribution and elimination of radiolabeled compounds should not be underestimated.[212] The progressive accumulation of [^{89}Zr]Zr-DFO-h-R3 in the kidneys between 24 h and 48 h after IP administration might be attributed to metabolic breakdown and renal excretion. The peritoneal cavity, where IP injection is given, allows for the absorption of substances into the bloodstream. The proximity of the injection site to the peritoneum facilitates rapid absorption of tracer into the systemic circulation, resulting in

increased activity levels in the abdomen shortly after administration.[213, 214] Statistically significant difference was observed in the abdomen between [^{89}Zr]Zr-DFO-h-R3 and [^{89}Zr]Zr-oxalate, both administered via IP injection. There was a slow decrease of activity in the abdomen after the administration of [^{89}Zr]Zr-DFO-h-R3 compared to the administration of [^{89}Zr]Zr-oxalate. [^{89}Zr]Zr-oxalate may drive the selective uptake and retention of the tracer in bone tissues, including the spine, resulting in the observed accumulation pattern.[208, 215]

Ex vivo biodistribution 24 h PI, confirmed that the bone did have significantly higher activity of [^{89}Zr]Zr-oxalate than [^{89}Zr]Zr-DFO-h-R3 24 h PI, indicating that the [^{89}Zr]Zr-DFO-h-R3 complex was stable *in vivo*, with little/no ^{89}Zr ions dissociating from the DFO-h-R3 complex 24 h PI.

The tail area exhibited slow clearance rates for [^{89}Zr]Zr-DFO-h-R3 compared to other organs, leading to prolonged retention of the tracer in this region after IV administration. This was due to frequent occurrence of *para*-venous activity deposited during the injection process. The delayed spread of activity to other organs beyond 6 h post administration suggests that [^{89}Zr]Zr-DFO-h-R3 gradually disseminates from the tail to other tissues or organs.

As indicative in the TAC's, the significant decrease in activity from 2 h to 4 h in the cardiac region and chest may be due to the initial distribution and accumulation of [^{89}Zr]Zr-DFO-h-R3 in these areas following IV administration. The absence of statistically significant differences in activity levels in the abdomen across different time points (2 h, 4 h, 6 h, 24 h and 48 h) suggests that the tracer remained stable and did not undergo dissociation or clearance in these regions throughout the observation period. The significant decrease in activity from 2 h to 24 h and further reduction by 48 h in the abdomen indicates that [^{89}Zr]Zr-DFO-h-R3 spread to other organs. However, IV administration of [^{89}Zr]Zr-DFO-h-R3 led to observable retention of the compound in the kidneys, as evidenced by *ex vivo* biodistribution data; albeit no statistically significant differences were noted in the biodistribution profiles between IP and IV of [^{89}Zr]Zr-DFO-h-R3.

The peak in activity of [^{89}Zr]Zr-oxalate at 1 h PI followed by a significant decrease by 6 h PI in the abdominal area suggests rapid initial distribution and subsequent clearance of

the tracer from this region. The lack of statistically significant differences in activity levels between different time points in the chest, and cardiac regions indicates fair integrity of [^{89}Zr]Zr-oxalate and clearance in these areas over the monitored time intervals. The high uptake in the plasma suggests that the tracer is extensively bound to plasma proteins or remains in the blood circulation for a significant period.[208, 216] The biodistribution results demonstrated sustained uptake of [^{89}Zr]Zr-DFO-h-R3 in the plasma after 24 h and 48 h regardless of IV- or IP administration.

The pancreas is a considered a retroperitoneal gland located on the posterior wall of the abdomen near the peritoneum.[217] Following IP administration, [^{89}Zr]Zr-DFO-h-R3 had higher local availability for absorption by the pancreas, resulting in significantly higher radioactivity levels (P = 0.033) in this organ compared to IV administration. The proximity of the pancreas to the injection site in the peritoneal cavity facilitates greater uptake, leading to approximately twice the level of radioactivity observed after IV injection.

The direct bolus of [^{89}Zr]Zr-DFO-h-R3 into the bloodstream via IV administration results in higher immediate systemic levels of the compound, as reflected by the significantly higher activity in the whole blood. The intestines and pancreas may have higher permeability and retention for [^{89}Zr]Zr-DFO-h-R3 when administered via the IP route, contributing to the observed differences in radioactivity levels. At 24 h post administration, most of [^{89}Zr]Zr-DFO-h-R3 was eradicated from the bloodstream, partly distributed, excreted or mildly retained in specific tissues. However, compared to smaller molecules, prolonged presence in the blood provides more opportunities for the compound to be taken up by tissues over time, indicating the increased tissue radioactivity. The high activity level of [^{89}Zr]Zr-DFO-h-R3 was observed in the plasma 24 h PI (vs. low activity of [^{89}Zr]Zr-oxalate). This indicates that the DFO-chelated compound remains in circulation and is less readily taken up by the bone compared to [^{89}Zr]Zr-oxalate.

[^{64}Cu]Cu-SarAr-h-R3 have a high affinity for receptors or binding sites present in the spleen and liver, leading to its preferential accumulation in these organs over time.[161] The metabolic processes in the spleen and liver, which are involved in the breakdown and clearance of substances from the bloodstream, can influence the retention of the tracer. [^{64}Cu]Cu-SarAr-h-R3 is metabolically stable, it can result in prolonged presence and

accumulation in the spleen and liver.[218] Monoclonal antibodies (mAbs) are eliminated from the body through either excretion or degradation processes. Unlike small molecules, mAbs are too large to be filtered out by the kidneys and typically do not get excreted in the urine, except under certain pathological conditions.[219] Following IV administration, [^{64}Cu]Cu-SarAr-h-R3 and [^{64}Cu]Cu-DOTA-h-R3 are directly introduced into the bloodstream, leading to direct distribution throughout the body via the circulatory system. The high uptake of [^{64}Cu]Cu-SarAr-h-R3 in the plasma indicates its presence in the systemic circulation, where it can interact with blood components and be transported to different organs and tissues.

The kidneys play a crucial role in the clearance of circulating substances from the bloodstream, and compounds that are not readily reabsorbed are excreted into the urine.[220, 221] The elevated uptake of [^{64}Cu]Cu-SarAr-h-R3 in the kidneys suggests accumulation of the tracer in the renal tissue, possibly due to its excretion through the urinary system.[222] The liver being a primary site for metabolism and detoxification [223, 224] has demonstrated high uptake of [^{64}Cu]Cu-DOTA-h-R3 which suggests that this complex is processed by the liver's metabolic pathways. Thus, supported by the nature of the SarAr chelator and its preference to elicit and enable renal transport mechanisms of larger molecules is a valuable outcome of this study. Simultaneously lower liver uptake of [^{64}Cu]Cu-SarAr-h-R3 compared to [^{64}Cu]Cu-DOTA-h-R3 indicates less hepatic processing or retention.

Consequently, the unwanted organ uptake and observed differences in biodistribution comparing [^{64}Cu]Cu-DOTA-h-R3 and [^{64}Cu]Cu-SarAr-h-R3 are primarily due to the distinct properties of the chelating agents (DOTA *versus* SarAr) and their interactions with biological systems. The DOTA chelator promotes higher uptake in the liver and broad distribution in metabolically active tissues, while the SarAr chelator facilitates efficient renal clearance and prolonged circulation, resulting in higher kidney and plasma activity.

Looking at its results for *ex vivo* biodistribution analysis significant differences in the radioactivity levels of [^{64}Cu]Cu-Cl_2 between IV and IP administration routes are primarily due to the differences in initial absorption sites and subsequent distribution patterns. IP administration seems to incur higher hepatic and intestinal uptake due to the first-pass

effect through the portal circulation, while IV administration shows higher uptake in the kidneys and lungs due to direct systemic circulation and immediate filtration roles. These factors collectively explain why IP administered [^{64}Cu]Cu-Cl_2 shows significantly higher activity levels in several organs compared to IV administration.

This study had various technical and analytical ***limitations***, notwithstanding being a retrospective study design that has the challenge of initial gaps to data sets or quality of the provided data in general. Although a statistically sufficient number of animals per group were included in the operational part of the study, the initial review of the data sets revealed technical and operational problems that were evident in the individual data sets, such as the occurrence of high levels of *para*-venous radioactivity, inconsistent or missing CT scans and unforeseen image artifacts (possibly caused by radioactive contaminants or accidental urination). Those negatively influenced data sets had to either be excluded or, if possible, run a partial image analysis. A few reconstructed PET images also suffered from low count rates which resulted in in non-comparable image quality within or across groups. This was however mitigated by applying corrective measures to such data sets which was performed as part of the different options, e.g., low radioactivity acquisition modus used as the standard software provided by Mediso for scans acquired with ID >3 MBq/ animal, and usage of “masking-off” areas of high (nodal) abdominal radioactivity present due to IP injection in scans > 6 h. Further corrections would have been possible, if the scan were to be performed with an internal source that can be positioned in the field of view in the vicinity of the animal) – a recommended procedure to more accurately compare groups of animals that have received varying levels of ID.

Challenges and limitations during the studies’ data collection have been mostly towards drawing the accurate 3D-VOI, especially if limited or no CT information was provided to navigate the PET image by way of anatomical (skeletal) reference points. Such mistakes between animals of the same group were considered acceptable. Data collection within the multiple scans performed on the same animal for each tracer was mitigated to use the same VOI information and only use shift-and-pivot actions within the software (which keeps the VOI size nearly the same). Results show that the variability within grouped imaging timepoints and data for one animal followed known (acceptable) limits (about ±

20%). Problems with animal movements that have been observed between CT and PET overlay were solved by manual correction by 2 experienced research radiographers. Nevertheless, some data sets were not salvageable, and some groups suffered from limited numbers of animals that lowered the integrity of the data during statistical analysis (mainly when comparing IV versus IP administered groups). Although potential findings were demonstrated and discussed; a sound conclusion may be too speculative and overly interpretive for particular image-guided analyses. In addition, the gaps in suitable animal numbers for this study's analysis or the overall PET/CT image quality warrant further investigation and optimization of imaging protocols - especially relevant for low-radioactivity PET-image acquisition.

8. CONCLUSION

In this study, preliminary findings concerning the exploration of different tracer injection routes as well as demonstrating *in vivo* pharmacokinetic behaviour of different radiometal-chelator combinations conjugated to h-R3 are presented. Elevated levels of radioactivity in the abdomen, intestines, liver/spleen or bone were deemed unfavourable. *Ex vivo* organ biodistribution data analyses provided adequate results. Contrary to IV administration, IP injection of [^{89}Zr]Zr-DFO-h-R3 resulted in high levels of radioactivity in the spleen and femoral bone (bone marrow included). When given IV, [^{64}Cu]Cu-DOTA-h-R3 exhibited larger amounts of radioactivity in the intestines, liver/spleen compared to IV injected [^{64}Cu]Cu-SarAr-h-R3. When [^{64}Cu]Cu-SarAr-h-R3 was given via IV, a prolonged high plasma radioactivity suggested extended blood circulation. The study results suggest that both, IV administered [^{64}Cu]Cu-SarAr-h-R3 and IV administered [^{89}Zr]Zr-DFO-h-R3 may provide the required pharmacokinetic behavior and time-activity relation (and excretion route) to allow for diagnostic imaging *in vivo* between 4-24 h post injection. [^{64}Cu]Cu-SarAr-h-R3 and [^{89}Zr]Zr-DFO-h-R3 may therefore be considered for future exploration in EGFR-overexpressing cancers and/or correlation analysis with cancer tissue analyses for h-R3 expression *in situ*. Further refinement of the h-R3 radiolabeling techniques is recommended to improve molar activity and improve imaging accuracy by decreasing the risk for an undesired, low-radioactivity-based imaging acquisition.

Improving the radiolabeling techniques for h-R3 can be accomplished by increasing molar activity, enhancing labeling stability and reducing non-specific binding.[225, 226]

9. REFERENCES

1. Sohel M, Sultana H, Sultana T, Al Amin M, Aktar S, Ali MC, Rahim ZB, Hossain MA, Al Mamun A, Amin MN, Dash R. Chemotherapeutic potential of hesperetin for cancer treatment, with mechanistic insights: A comprehensive review. Heliyon. 2022;8(1):e08815.
2. Slika H, Mansour H, Wehbe N, Nasser SA, Iratni R, Nasrallah G, Shaito A, Ghaddar T, Kobeissy F, Eid AH. Therapeutic potential of flavonoids in cancer: Ros-mediated mechanisms. Biomed Pharmacother. 2022;146:112442.
3. Viegas S, Ladeira C, Costa-Veiga A, Perelman J, Gajski G. Forgotten public health impacts of cancer - an overview. Arh Hig Rada Toksikol. 2017;68(4):287-97.
4. Xu M, Liu X, Li P, Yang Y, Zhang W, Zhao S, Zeng Y, Zhou X, Zeng LH, Yang G. Modified natriuretic peptides and their potential roles in cancer treatment. Biomed J. 2022;45(1):118-31.
5. Elveny M, Khan A, Nakhjiri AT, Albadarin AB. A state-of-the-art review on the application of various pharmaceutical nanoparticles as a promising technology in cancer treatment. Arabian Journal of Chemistry. 2021;14(10).
6. Howell KC. Review on cancer. Research and reviews: journal of medical and health sciences. 2016;2016.
7. Cooper GM. The cell: A molecular approach. 2nd edition: Sinauer Associates, Inc.; 2000. Available from: https://www.ncbi.nlm.nih.gov/books/NBK9963/#_ncbi_dlg_citbx_NBK9963.
8. Malaviya M, Kishorbhai VT. Overview of an ovarian cancer and its treatment aspects. International Journal of Pharmaceutical and Biological Science Archive. 2021;9(2).
9. Wallace J. Humane endpoints and cancer research. ILAR J. 2000;41(2):87-93.
10. Keyvani V, Riahi E, Yousefi M, Esmaeili SA, Shafabakhsh R, Moradi Hasan-Abad A, Mahjoubin-Tehran M, Hamblin MR, Mollazadeh S, Mirzaei H. Gynecologic cancer, cancer stem cells, and possible targeted therapies. Front Pharmacol. 2022;13:823572.
11. Zhang PW, Chen L, Huang T, Zhang N, Kong XY, Cai YD. Classifying ten types of major cancers based on reverse phase protein array profiles. PLoS One. 2015;10(3):e0123147.
12. Heim D, Budczies J, Stenzinger A, Treue D, Hufnagl P, Denkert C, Dietel M, Klauschen F. Cancer beyond organ and tissue specificity: Next-generation-sequencing gene mutation data reveal complex genetic similarities across major cancers. Int J Cancer. 2014;135(10):2362-9.
13. Xu Y, Cui J, Puett D. Cancer classification and molecular signature identification. In: Xu Y, Cui J, Puett D, editors. Cancer bioinformatics. New York, NY: Springer New York; 2014. p. 65-87.
14. Fabio M, Alberto LH, Federica C, Nicola G, Vito P, Fabio M. Cd38: A target for immunotherapeutic approaches in multiple myeloma2018; 9.
15. Piechocki M, Koziolek W, Sroka D, Matrejek A, Miziolek P, Saiuk N, Sledzik M, Jaworska A, Bereza K, Pluta E, Banas T. Trends in incidence and mortality of gynecological and breast cancers in poland (1980-2018). Clin Epidemiol. 2022;14:95-114.
16. Vultaggio A, Petrella MC, Tomao F, Nencini F, Mecheri V, Marini A, Perlato M, Vivarelli E, De Angelis C, Ferrarini I, Pillozzi S, Matucci A, Antonuzzo L. The anti-ige monoclonal antibody omalizumab as adjuvant treatment in desensitization to carboplatin in patients with ovarian cancer. Gynecol Oncol Rep. 2021;38:100880.
17. Reyners AK, Broekman KE, Glaudemans AW, Brouwers AH, Arts HJ, van der Zee AG, de Vries EG, Jalving M. Molecular imaging in ovarian cancer. Ann Oncol. 2016;27 Suppl 1:i23-i9.
18. Miao M, Miao Y, Zhu Y, Wang J, Zhou H. Advances in exosomes as diagnostic and therapeutic biomarkers for gynaecological malignancies. Cancers (Basel). 2022;14(19):4743.

19. Moffitt L, Karimnia N, Stephens A, Bilandzic M. Therapeutic targeting of collective invasion in ovarian cancer. Int J Mol Sci. 2019;20(6):1466.
20. Manzoor H, Naheed H, Ahmad K, Iftikhar S, Asif M, Shuja J, Sultan N, Ali I, Inayatullah S, Khan YH. Pattern of gynaecological malignancies in south western region of pakistan: An overview of 12 years. Biomed Rep. 2017;7(5):487-91.
21. Jacson M J, Mishra B. Histone modifications: The double edged sword in gynaecological cancers. World Journal of Current Medical and Pharmaceutical Research. 2020;02(02):120-4.
22. Erem AS, Appiah-Kubi A, Konney TO, Amo-Antwi K, Bell SG, Johnson TRB, Johnston C, Tawiah Odoi A, Lawrence ER. Gynecologic oncology sub-specialty training in ghana: A model for sustainable impact on gynecologic cancer care in sub-saharan africa. Frontiers in Public Health. 2020;8.
23. Dhokotera TG, Muchengeti M, Davidović M, Rohner E, Olago V, Egger M, Bohlius J. Gynaecologic and breast cancers in women living with hiv in south africa: A record linkage study. International journal of cancer. 2024;154(2):284-96.
24. Olorunfemi G, Libhaber E, Ezechi OC, Musenge E. Population-based temporal trends and ethnic disparity in cervical cancer mortality in south africa (1999-2018): A join point and age-period-cohort regression analyses. Cancers (Basel). 2022;14(24):6256.
25. Kemppainen J, Hynninen J, Virtanen J, Seppanen M. Pet/ct for evaluation of ovarian cancer. Semin Nucl Med. 2019;49(6):484-92.
26. Lheureux S, Gourley C, Vergote I, Oza AM. Epithelial ovarian cancer. Lancet. 2019;393(10177):1240-53.
27. Gaona-Luviano P, Medina-Gaona LA, Magana-Perez K. Epidemiology of ovarian cancer. Chin Clin Oncol. 2020;9(4):47.
28. Penny SM. Ovarian cancer: An overview. Radiol Technol. 2020;91(6):561-75.
29. Fujita M, Tase T, Kakugawa Y, Hoshi S, Nishino Y, Nagase S, Ito K, Niikura H, Yaegashi N, Minami Y. Smoking, earlier menarche and low parity as independent risk factors for gynecologic cancers in japanese: A case-control study. Tohoku J Exp Med. 2008;216(4):297-307.
30. Ozturk R, Bakir S, Kazankaya F, Paker S, Ertem G. Awareness about gynecologic cancers and related factors among healthy women: A cross-sectional study. Soc Work Public Health. 2021;36(7-8):847-56.
31. Pecorelli S, Benedet JL, Creasman WT, Shepherd JH, on behalf of the – FCoGO. Figo staging of gynecologic cancer. International Journal of Gynecology & Obstetrics. 1999;65(3):243-9.
32. Höhn AK, Brambs CE, Hiller GGR, May D, Schmoeckel E, Horn L-C. 2020 who classification of female genital tumors. Geburtshilfe und Frauenheilkunde. 2021;81(10):1145-53.
33. Webber C, Gospodarowicz M, Sobin LH, Wittekind C, Greene FL, Mason MD, Compton C, Brierley J, Groome PA. Improving the tnm classification: Findings from a 10-year continuous literature review. International Journal of Cancer. 2014;135(2):371-8.
34. Okunade KS. Human papillomavirus and cervical cancer. Journal of obstetrics and gynaecology : the journal of the Institute of Obstetrics and Gynaecology. 2020;40(5):602-8.
35. Benson RC. Part i: Cancer of the cervix uteri. CA: A Cancer Journal for Clinicians. 1967;17(4):173-82.
36. Vale DB, Cavalcante LA, Andrade LALDA, Teixeira JC, Menin TLodR, Zeferino LC. Stage and histology of cervical cancer in women under 25 years old. Journal of Gynecologic Oncology. 2019;30(4).
37. McCluggage WG. Progress in the pathological arena of gynecological cancers. International journal of gynaecology and obstetrics: the official organ of the International Federation of Gynaecology and Obstetrics. 2021;155 Suppl 1:107-14.
38. Guimaraes DP, Hainaut P. Tp53: A key gene in human cancer. Biochimie. 2002;84(1):83-93.
39. Martin ACR, Facchiano AM, Cuff AL, Hernandez-Boussard T, Olivier M, Hainaut P, Thornton JM. Integrating mutation data and structural analysis of the tp53 tumor-suppressor protein. Human Mutation. 2002;19(2):149-64.

40. Petitjean A, Achatz MIW, Borresen-Dale AL, Hainaut P, Olivier M. Tp53 mutations in human cancers: Functional selection and impact on cancer prognosis and outcomes. Oncogene. 2007;26(15):2157-65.
41. Hodgson A, Park KJ, Djordjevic B, Howitt BE, Nucci MR, Oliva E, Stolnicu S, Xu B, Soslow RA, Parra-Herran C. International endocervical adenocarcinoma criteria and classification: Validation and interobserver reproducibility. The American journal of surgical pathology. 2019;43(1):75-83.
42. Green J, Berrington De Gonzalez A, Sweetland S, Beral V, Chilvers C, Crossley B, Deacon J, Hermon C, Jha P, Mant D, Peto J, Pike M, Vessey MP. Risk factors for adenocarcinoma and squamous cell carcinoma of the cervix in women aged 20–44 years: The uk national case–control study of cervical cancer. British Journal of Cancer. 2003;89(11):2078-86.
43. Bahrami A, Hasanzadeh M, Shahidsales S, Farazestanian M, Hassanian SM, Moetamani Ahmadi M, Maftouh M, Gharib M, Yousefi Z, Kadkhodayan S, Ferns GA, Avan A. Genetic susceptibility in cervical cancer: From bench to bedside. Journal of Cellular Physiology. 2018;233(3):1929-39.
44. Liu Z-C, Liu W-D, Liu Y-H, Ye X-H, Chen S-D. Multiple sexual partners as a potential independent risk factor for cervical cancer: A meta-analysis of epidemiological studies. Asian Pacific Journal of Cancer Prevention. 2015;16(9):3893-900.
45. Brinton LA, Hamman RF, Huggins GR, Lehman HF, Levine RS, Mallin K, Fraumeni JF. Sexual and reproductive risk factors for invasive squamous cell cervical cancer. Journal of the National Cancer Institute. 1987;79(1):23-30.
46. Kalogera E, Dowdy SC, Bakkum-Gamez JN. Preserving fertility in young patients with endometrial cancer: Current perspectives. International Journal of Women's Health [Internet]. 2014; 2014(default):[691-701 pp.].
47. Zhang S, Gong T-T, Liu F-H, Jiang Y-T, Sun H, Ma X-X, Zhao Y-H, Wu Q-J. Global, regional, and national burden of endometrial cancer, 1990–2017: Results from the global burden of disease study, 2017. Frontiers in Oncology. 2019;9.
48. Goel JK, Kumar P. Cancer endometrium: An update. Journal of SAFOG. 2012;4(2):75-84.
49. Urick ME, Bell DW. Clinical actionability of molecular targets in endometrial cancer. Nature Reviews Cancer. 2019;19(9):510-21.
50. Prat J, Gallardo A, Cuatrecasas M, Catasus L. Endometrial carcinoma: Pathology and genetics. Pathology. 2007;39(1):72-87.
51. Doll A, Abal M, Rigau M, Monge M, Gonzalez M, Demajo S, Colas E, Llaurado M, Alazzouzi H, Planaguma J, Lohmann MA, Garcia J, Castellvi S, Ramon y Cajal J, Gil-Moreno A, Xercavins J, Alameda F, Reventos J. Novel molecular profiles of endometrial cancer-new light through old windows. J Steroid Biochem Mol Biol. 2008;108(3-5):221-9.
52. Lim D, Oliva E. Nonendometrioid endometrial carcinomas. Semin Diagn Pathol. 2010;27(4):241-60.
53. Silva EG, Deavers MT, Malpica A. Undifferentiated carcinoma of the endometrium: A review. Pathology. 2007;39(1):134-8.
54. AlHilli M, Elson P, Rybicki L, Amarnath S, Yang B, Michener CM, Rose PG. Undifferentiated endometrial carcinoma: A national cancer database analysis of prognostic factors and treatment outcomes. International Journal of Gynecologic Cancer [Internet]. 2019; 29(7):[1126 p.]. Available from: http://dx.doi.org/10.1136/ijgc-2019-000465.
55. Setiawan VW, Yang HP, Pike MC, McCann SE, Yu H, Xiang Y-B, Wolk A, Wentzensen N, Weiss NS, Webb PM, Van Den Brandt PA, Van De Vijver K, Thompson PJ, Strom BL, Spurdle AB, Soslow RA, Shu X-O, Schairer C, Sacerdote C, Rohan TE, Robien K, Risch HA, Ricceri F, Rebbeck TR, Rastogi R, Prescott J, Polidoro S, Park Y, Olson SH, Moysich KB, Miller AB, McCullough ML, Matsuno RK, Magliocco AM, Lurie G, Lu L, Lissowska J, Liang X, Lacey JV, Kolonel LN, Henderson BE, Hankinson SE, Håkansson N, Goodman MT, Gaudet MM, Garcia-Closas M, Friedenreich CM, Freudenheim JL, Doherty J, De Vivo I, Courneya KS, Cook

LS, Chen C, Cerhan JR, Cai H, Brinton LA, Bernstein L, Anderson KE, Anton-Culver H, Schouten LJ, Horn-Ross PL. Type i and ii endometrial cancers: Have they different risk factors? Journal of Clinical Oncology. 2013;31(20):2607-18.
56. Raglan O, Kalliala I, Markozannes G, Cividini S, Gunter MJ, Nautiyal J, Gabra H, Paraskevaidis E, Martin-Hirsch P, Tsilidis KK, Kyrgiou M. Risk factors for endometrial cancer: An umbrella review of the literature. International Journal of Cancer. 2019;145(7):1719-30.
57. Chhabra S, Bhavani M, Deshpande A. Trends of vulvar cancer. Journal of obstetrics and gynaecology : the journal of the Institute of Obstetrics and Gynaecology. 2014;34(2):165-8.
58. Bray F, Laversanne M, Weiderpass E, Arbyn M. Geographic and temporal variations in the incidence of vulvar and vaginal cancers. International journal of cancer. 2020;147(10):2764-71.
59. International Collaboration of Epidemiological Studies of Cervical C. Comparison of risk factors for invasive squamous cell carcinoma and adenocarcinoma of the cervix: Collaborative reanalysis of individual data on 8,097 women with squamous cell carcinoma and 1,374 women with adenocarcinoma from 12 epidemiological studies. Int J Cancer. 2007;120(4):885-91.
60. Parkash V, Aisagbonhi O, Riddle N, Siddon A, Panse G, Fadare O. Recent advances in the classification of gynecological tract tumors: Updates from the 5th edition of the world health organization “blue book”. Archives of Pathology & Laboratory Medicine. 2023;147(10):1204-16.
61. Hrudka J, Rosová B, Halaška MJ. Squamous cell carcinoma with sarcomatoid differentiation or carcinosarcoma of the uterine cervix associated with hpv33 infection: Report of a rare case. Diagnostic Pathology [Internet]. 2020; 15(1). Available from: http://dx.doi.org/10.1186/s13000-020-00934-y.
62. Desouki MM, Fadare O. Primary adenocarcinomas of the vulva and related structures: An enigmatic and diverse group of tumors☆. Seminars in diagnostic pathology. 2021;38(1):71-84.
63. Duong TH, Flowers LC. Vulvo-vaginal cancers: Risks, evaluation, prevention and early detection. Obstetrics and gynecology clinics of North America. 2007;34(4):783-802, x.
64. Muñoz N, Castellsagué X, de González AB, Gissmann L. Chapter 1: Hpv in the etiology of human cancer. Vaccine. 2006;24:S1-S10.
65. Edwards CL, Tortolero-Luna G, Linares AC, Malpica A, Baker VV, Cook E, Johnson E, Follen Mitchell M. Vulvar intraepithelial neoplasia and vulvar cancer. Obstetrics and gynecology clinics of North America. 1996;23(2):295-324.
66. Hill-Daniel J, Roett MA. Genital cancers in women: Vulvar cancer. FP essentials. 2015;438:31-43; quiz 4-8.
67. Zheng F, Zhang Y, Chen S, Weng X, Rao Y, Fang H. Mechanism and current progress of poly adp-ribose polymerase (parp) inhibitors in the treatment of ovarian cancer. Biomed Pharmacother. 2020;123:109661.
68. Meinhold-Heerlein I, Hauptmann S. The heterogeneity of ovarian cancer. Arch Gynecol Obstet. 2014;289(2):237-9.
69. Stewart C, Ralyea C, Lockwood S. Ovarian cancer: An integrated review. Semin Oncol Nurs. 2019;35(2):151-6.
70. Suppiah S. The past, present and future of diagnostic imaging in ovarian cancer. Ovarian cancer - from pathogenesis to treatment2018.
71. Reid BM, Permuth JB, Sellers TA. Epidemiology of ovarian cancer: A review. Cancer Biol Med. 2017;14(1):9-32.
72. Funston G, O’Flynn H, Ryan NAJ, Hamilton W, Crosbie EJ. Recognizing gynecological cancer in primary care: Risk factors, red flags, and referrals. Advances in Therapy. 2018;35(4):577-89.
73. Sarkar M, Konar H, Raut D. Clinico-pathological features of gynecological malignancies in a tertiary care hospital in eastern india: Importance of strengthening primary health care in prevention and early detection. Asian Pacific journal of cancer prevention : APJCP [Internet]. 2013; 14(6):[3541-7 pp.].

74. Dasari S, Wudayagiri R, Valluru L. Cervical cancer: Biomarkers for diagnosis and treatment. Clinica Chimica Acta. 2015;445:7-11.
75. Zavesky L, Jandakova E, Turyna R, Langmeierova L, Weinberger V, Minar L, Kohoutova M. New perspectives in diagnosis of gynaecological cancers: Emerging role of circulating micrornas as novel biomarkers. Neoplasma. 2015;62(4):509-20.
76. Williams P, Bond CM, Burton C, Murchie P. A systematic review of the use, quality and effects of pelvic examination in primary care for the detection of gynaecological cancer. Journal of Obstetrics and Gynaecology [Internet]. 2018; 38(5):[737- pp.]. Available from: http://dx.doi.org/10.1080/01443615.2018.1444410.
77. Jin J. Pelvic examinations in nonpregnant women. JAMA. 2017;317(9):984.
78. Soma L, Allen M, Tobin L, Ganster C, Bulley M, Hunt J, Kricka LJ, Senior M, Kao A. Ca-125 concentrations in patients awaiting cardiac transplantation. Clin Chem. 2002;48(12):2289-90.
79. Sutaria RR, Satia MN, Badhwar VR. Unusual presentation of a case of ovarian endometrioma. International Journal of Reproduction, Contraception, Obstetrics and Gynecology. 2018;7(8):3403.
80. Ferraro S, Braga F, Lanzoni M, Boracchi P, Biganzoli EM, Panteghini M. Serum human epididymis protein 4 vs carbohydrate antigen 125 for ovarian cancer diagnosis: A systematic review. Journal of clinical pathology. 2013;66(4):273-81.
81. Escudero JM, Auge JM, Filella X, Torne A, Pahisa J, Molina R. Comparison of serum human epididymis protein 4 with cancer antigen 125 as a tumor marker in patients with malignant and nonmalignant diseases. Clinical chemistry. 2011;57(11):1534-44.
82. Simmons AR, Baggerly K, Bast RC. The emerging role of he4 in the evaluation of epithelial ovarian and endometrial carcinomas. Oncology (Williston Park, NY). 2013;27(6):548-56.
83. Pruthi S, Gostout BS, Lindor NM. Identification and management of women with brca mutations or hereditary predisposition for breast and ovarian cancer. Mayo Clinic proceedings. 2010;85(12):1111-20.
84. Metcalfe KA, Dennis C-L, Poll A, Armel S, Demsky R, Carlsson L, Nanda S, Kiss A, Narod SA. Effect of decision aid for breast cancer prevention on decisional conflict in women with a brca1 or brca2 mutation: A multisite, randomized, controlled trial. Genetics in medicine : official journal of the American College of Medical Genetics. 2017;19(3):330-6.
85. Ludeman L, Valori RM, Shepherd NA. The principles and techniques of biopsy. Surgery (Oxford). 2002;20(8):iii-vii.
86. Tilly H, Dreyling M, Group EGW. Diffuse large b-cell non-hodgkin's lymphoma: Esmo clinical practice guidelines for diagnosis, treatment and follow-up. Ann Oncol. 2010;21 Suppl 5(Supplement 5):v172-4.
87. Burke L. Colposcopy of the cervix. The uterus. Clinical perspectives in obstetrics and gynecology1991. p. 141-54.
88. Gagné HM. Colposcopy of the vagina and vulva. Obstetrics and gynecology clinics of North America. 2008;35(4):659-69; x.
89. Asati P, Sultan S, Nigam RK, Asati S. Study of colposcopic and histopathological correlation for cervical lesion at tertiary care: An original research. International journal of health sciences. 2022:2672-82.
90. Williams PM, Gaddey HL. Endometrial biopsy: Tips and pitfalls. American family physician. 2020;101(9):551-6.
91. Griffin N, Grant LA, Freeman SJ, Jimenez-Linan M, Berman LH, Earl H, Ahmed AA, Crawford R, Brenton J, Sala E. Image-guided biopsy in patients with suspected ovarian carcinoma: A safe and effective technique? European radiology. 2009;19(1):230-5.
92. Deguara C, Davis C. Laparoscopic entry techniques. Curr Opin Obstet Gynecol. 2011;23(4):268-72.
93. Ahmad G, Baker J, Finnerty J, Phillips K, Watson A. Laparoscopic entry techniques. Cochrane Database of Systematic Reviews [Internet]. 2019; (1).

94. Ruiz-Fernandez D, Galiana-Merino JJ, de Ramon-Fernandez A, Vives-Boix V, Enriquez-Buendia P. A dcp-based method for improving laparoscopic images. J Med Syst. 2020;44(4):78.
95. Obermair A, Hiebl S. Laparoscopy in the treatment of ovarian tumours of low malignant potential. Aust N Z J Obstet Gynaecol. 2007;47(6):438-44.
96. Ellmann A, Holness J. Nuclear medicine in oncology 1 : Lymphoma, and cancer of the lung, colon, and oesophagus. CME. 2013;31(8):279-83.
97. Castellani F, Nganga EC, Dumas L, Banerjee S, Rockall AG. Imaging in the pre-operative staging of ovarian cancer. Abdom Radiol (NY). 2019;44(2):685-96.
98. Expert Panel on Women's I, Kang SK, Reinhold C, Atri M, Benson CB, Bhosale PR, Jhingran A, Lakhman Y, Maturen KE, Nicola R, Pandharipande PV, Salazar GM, Shipp TD, Simpson L, Small W, Jr., Sussman BL, Uyeda JW, Wall DJ, Whitcomb BP, Zelop CM, Glanc P. Acr appropriateness criteria((r)) staging and follow-up of ovarian cancer. J Am Coll Radiol. 2018;15(5S):S198-S207.
99. Luczynska E, Zbigniew K. Diagnostic imaging in gynecology. Ginekol Pol. 2022;93(1):63-9.
100. Fischerova D, Burgetova A. Imaging techniques for the evaluation of ovarian cancer. Best Pract Res Clin Obstet Gynaecol. 2014;28(5):697-720.
101. Fischerova D. Ultrasound scanning of the pelvis and abdomen for staging of gynecological tumors: A review. Ultrasound Obstet Gynecol. 2011;38(3):246-66.
102. Iyer VR, Lee SI. Mri, ct, and pet/ct for ovarian cancer detection and adnexal lesion characterization. AJR Am J Roentgenol. 2010;194(2):311-21.
103. Foti PV, Attina G, Spadola S, Caltabiano R, Farina R, Palmucci S, Zarbo G, Zarbo R, D'Arrigo M, Milone P, Ettorre GC. Mr imaging of ovarian masses: Classification and differential diagnosis. Insights Imaging. 2016;7(1):21-41.
104. Ryoo UN, Choi CH, Yoon JY, Noh SK, Kang H, Kim WY, Kim BH, Kim T-J, Lee J-W, Lee J-H, Kim B-G, Bae D-S. Mr imaging in endometrial carcinoma as a diagnostic tool for the prediction of myometrial invasion and lymph node metastasis. Cancer Research and Treatment : Official Journal of Korean Cancer Association. 2007;39(4):165-70.
105. Sahdev A, Sohaib SA, Wenaden AET, Shepherd JH, Reznek RH. The performance of magnetic resonance imaging in early cervical carcinoma: A long-term experience. International journal of gynecological cancer : official journal of the International Gynecological Cancer Society. 2007;17(3):629-36.
106. Seyed Mohammad A, Mardanshahi A, Shahhosseini R, Hosseinimehr SJ. Nuclear medicine for imaging of epithelial ovarian cancer. Future Oncology. 2016;12(9):1165-–77.
107. Eary JF. Nuclear medicine in cancer diagnosis. Lancet. 1999;354(9181):853-7.
108. Vahidfar N, Farzanefar S, Ahmadzadehfar H, Molloy EN, Eppard E. A review of nuclear medicine approaches in the diagnosis and the treatment of gynecological malignancies. Cancers (Basel). 2022;14(7).
109. Balma M, Liberini V, Racca M, Laudicella R, Bauckneht M, Buschiazzo A, Nicolotti DG, Peano S, Bianchi A, Albano G, Quartuccio N, Abgral R, Morbelli SD, D'Alessandria C, Terreno E, Huellner MW, Papaleo A, Deandreis D. Non-conventional and investigational pet radiotracers for breast cancer: A systematic review. Front Med (Lausanne). 2022;9:881551.
110. Kiraga Ł, Kucharzewska P, Paisey S, Cheda Ł, Domańska A, Rogulski Z, Rygiel TP, Boffi A, Król M. Nuclear imaging for immune cell tracking in vivo – comparison of various cell labeling methods and their application. Coordination Chemistry Reviews. 2021;445.
111. Decazes P, Bohn P. Immunotherapy by immune checkpoint inhibitors and nuclear medicine imaging: Current and future applications. Cancers (Basel). 2020;12(2):371.
112. Alavi A, Hirsch LJ. Studies of central nervous system disorders with single photon emission computed tomography and positron emission tomography: Evolution over the past 2 decades. Semin Nucl Med. 1991;21(1):58-81.

113. Michael DD. Single-photon emission computed tomography in neurotherapeutics. Neurotherapeutics [Internet]. 2005; 2(2):[237-49 pp.].
114. Krishnan V, Berek JS, Dorigo O. Immunotherapy in ovarian cancer. Curr Probl Cancer. 2017;41(1):48-63.
115. Crisan G, Moldovean-Cioroianu NS, Timaru DG, Andries G, Cainap C, Chis V. Radiopharmaceuticals for pet and spect imaging: A literature review over the last decade. Int J Mol Sci. 2022;23(9):5023.
116. Petersson J, Sanchez-Crespo A, Larsson SA, Mure M. Physiological imaging of the lung: Single-photon-emission computed tomography (spect). J Appl Physiol (1985). 2007;102(1):468-76.
117. Aluicio-Sarduy E, Ellison PA, Barnhart TE, Cai W, Nickles RJ, Engle JW. Pet radiometals for antibody labeling. J Labelled Comp Radiopharm. 2018;61(9):636-51.
118. Di Lorenzo G, Ricci G, Severini GM, Romano F, Biffi S. Imaging and therapy of ovarian cancer: Clinical application of nanoparticles and future perspectives. Theranostics. 2018;8(16):4279-94.
119. Sanaz K, Liesl SE, Babak S, Ali G, Abass A. Advantages and applications of total-body pet scanning. Diagnostics [Internet]. 2022; 12(2):[426 p.]. Available from: http://dx.doi.org/10.3390/diagnostics12020426.
120. Lee SI, Catalano OA, Dehdashti F. Evaluation of gynecologic cancer with mr imaging, 18f-fdg pet/ct, and pet/mr imaging. J Nucl Med. 2015;56(3):436-43.
121. Papathanassiou D, Bruna-Muraille C, Liehn JC, Nguyen TD, Cure H. Positron emission tomography in oncology: Present and future of pet and pet/ct. Crit Rev Oncol Hematol. 2009;72(3):239-54.
122. Apostolova I, Wedel F, Brenner W. Imaging of tumor metabolism using positron emission tomography (pet). Metabolism in cancer. Recent results in cancer research 2197-6767: Cham : Springer International Publishing : Springer; 2016. p. 177-205.
123. Bussink J, Kaanders JH, van der Graaf WT, Oyen WJ. Pet-ct for radiotherapy treatment planning and response monitoring in solid tumors. Nat Rev Clin Oncol. 2011;8(4):233-42.
124. ElHariri MAG, Harira M, Riad MM. Usefulness of pet–ct in the evaluation of suspected recurrent ovarian carcinoma. Egyptian Journal of Radiology and Nuclear Medicine. 2019;50(1).
125. Gazis E. The ionizing radiation interaction with matter, thex-ray computedtomography imaging, the nuclear medicine spect, pet and pet-ct tomography imaging. Intech. 2019.
126. Narayanan P, Sahdev A. The role of (18)f-fdg pet ct in common gynaecological malignancies. Br J Radiol. 2017;90(1079):20170283.
127. Dolci C, Ceppi L, Guerra L, Crivellaro C, Lamanna M, Adorni M, Elisei F, Bonazzi CM, Sina F, Fruscio R, Messa C. Role of (18) f-fluoro-2-deoxyglucose positron emission tomography/computed tomography (18f-fdg pet/ct) in malignant ovarian germ cell tumors: A single-center experience with long term follow-up. Int J Gynecol Cancer. 2019;29(8):1298-303.
128. McKinley ET, Ayers GD, Smith RA, Saleh SA, Zhao P, Washington MK, Coffey RJ, Manning HC. Limits of [18f]-flt pet as a biomarker of proliferation in oncology. PLoS One. 2013;8(3):e58938.
129. Schelhaas S, Heinzmann K, Bollineni VR, Kramer GM, Liu Y, Waterton JC, Aboagye EO, Shields AF, Soloviev D, Jacobs AH. Preclinical applications of 3'-deoxy-3'-[(18)f]fluorothymidine in oncology - a systematic review. Theranostics. 2017;7(1):40-50.
130. Zhang CC, Yan Z, Li W, Kuszpit K, Painter CL, Zhang Q, Lappin PB, Nichols T, Lira ME, Affolter T, Fahey NR, Cullinane C, Spilker M, Zasadny K, O'Brien P, Buckman D, Wong A, Christensen JG. [(18)f]flt-pet imaging does not always "light up" proliferating tumor cells. Clin Cancer Res. 2012;18(5):1303-12.
131. Tsujikawa T, Makino A, Mori T, Tsuyoshi H, Kiyono Y, Yoshida Y, Okazawa H. Pet imaging of estrogen receptors for gynecological tumors. Clin Nucl Med. 2022;47(7):e481-e8.
132. van Kruchten M, de Vries EFJ, Arts HJG, Jager NM, Bongaerts AHH, Glaudemans AWJM, Hollema H, de Vries EGE, Hospers GAP, Reyners AKL. Assessment of estrogen receptor expression in epithelial ovarian cancer patients using 16α-18f-fluoro-17β-estradiol pet/ct. Journal of Nuclear Medicine. 2015;56(1):50-5.

133. Liao GJ, Clark AS, Schubert EK, Mankoff DA. 18f-fluoroestradiol pet: Current status and potential future clinical applications. J Nucl Med. 2016;57(8):1269-75.
134. Piert M, Machulla HJ, Picchio M, Reischl G, Ziegler S, Kumar P, Wester HJ, Beck R, McEwan AJ, Wiebe LI, Schwaiger M. Hypoxia-specific tumor imaging with 18f-fluoroazomycin arabinoside. J Nucl Med. 2005;46(1):106-13.
135. Vaupel P, Mayer A. Hypoxia in cancer: Significance and impact on clinical outcome. Cancer Metastasis Rev. 2007;26(2):225-39.
136. Laitala A, Erler JT. Hypoxic signalling in tumour stroma. Front Oncol. 2018;8:189.
137. Klemba A, Bodnar L, Was H, Brodaczewska KK, Wcislo G, Szczylik CA, Kieda C. Hypoxia-mediated decrease of ovarian cancer cells reaction to treatment: Significance for chemo- and immunotherapies. International Journal of Molecular Sciences [Internet]. 2020; 21(24).
138. Saita K, Chen M, Spratt NJ, Porritt MJ, Liberatore GT, Read SJ, Levi CR, Donnan GA, Ackermann U, Tochon-Danguy HJ, Sachinidis JI, Howells DW. Imaging the ischemic penumbra with 18f-fluoromisonidazole in a rat model of ischemic stroke. Stroke. 2004;35(4):975-80.
139. Masaki Y, Shimizu Y, Yoshioka T, Tanaka Y, Nishijima K, Zhao S, Higashino K, Sakamoto S, Numata Y, Yamaguchi Y, Tamaki N, Kuge Y. The accumulation mechanism of the hypoxia imaging probe "fmiso" by imaging mass spectrometry: Possible involvement of low-molecular metabolites. Sci Rep. 2015;5(1):16802.
140. Tran LB, Bol A, Labar D, Jordan B, Magat J, Mignion L, Gregoire V, Gallez B. Hypoxia imaging with the nitroimidazole 18f-faza pet tracer: A comparison with oxylite, epr oximetry and 19f-mri relaxometry. Radiother Oncol. 2012;105(1):29-35.
141. Rajendran JG, Krohn KA. F-18 fluoromisonidazole for imaging tumor hypoxia: Imaging the microenvironment for personalized cancer therapy. Semin Nucl Med. 2015;45(2):151-62.
142. Savi A, Incerti E, Fallanca F, Bettinardi V, Rossetti F, Monterisi C, Compierchio A, Negri G, Zannini P, Gianolli L, Picchio M. First evaluation of pet-based human biodistribution and dosimetry of (18)f-faza, a tracer for imaging tumor hypoxia. J Nucl Med. 2017;58(8):1224-9.
143. Agency IAE. Atlas of non-fdg pet – ct in diagnostic oncology. VIENNA: IAEA; 2021. 256- p.
144. Cheng J, Lei L, Xu J, Sun Y, Zhang Y, Wang X, Pan L, Shao Z, Zhang Y, Liu G. 18f-fluoromisonidazole pet/ct: A potential tool for predicting primary endocrine therapy resistance in breast cancer. J Nucl Med. 2013;54(3):333-40.
145. Busk M, Horsman MR, Jakobsen S, Bussink J, van der Kogel A, Overgaard J. Cellular uptake of pet tracers of glucose metabolism and hypoxia and their linkage. Eur J Nucl Med Mol Imaging. 2008;35(12):2294-303.
146. Lewis JS, Laforest R, Dehdashti F, Grigsby PW, Welch MJ, Siegel BA. An imaging comparison of 64cu-atsm and 60cu-atsm in cancer of the uterine cervix. J Nucl Med. 2008;49(7):1177-82.
147. Wei W, Rosenkrans ZT, Liu J, Huang G, Luo QY, Cai W. Immunopet: Concept, design, and applications. Chem Rev. 2020;120(8):3787-851.
148. Dewulf J, Adhikari K, Vangestel C, Wyngaert TVD, Elvas F. Development of antibody immuno-pet/spect radiopharmaceuticals for imaging of oncological disorders-an update. Cancers (Basel). 2020;12(7).
149. Sugiura G, Kuhn H, Sauter M, Haberkorn U, Mier W. Radiolabeling strategies for tumor-targeting proteinaceous drugs. Molecules. 2014;19(2):2135-65.
150. White JM, Escorcia FE, Viola NT. Perspectives on metals-based radioimmunotherapy (rit): Moving forward. Theranostics. 2021;11(13):6293-314.
151. Teicher BA, Chari RV. Antibody conjugate therapeutics: Challenges and potential. Clin Cancer Res. 2011;17(20):6389-97.
152. Fu R, Carroll L, Yahioglu G, Aboagye EO, Miller PW. Antibody fragment and affibody immunopet imaging agents: Radiolabelling strategies and applications. ChemMedChem. 2018;13(23):2466-78.

153. Liu S. Bifunctional coupling agents for radiolabeling of biomolecules and target-specific delivery of metallic radionuclides. Adv Drug Deliv Rev. 2008;60(12):1347-70.
154. Jauw YW, Menke-van der Houven van Oordt CW, Hoekstra OS, Hendrikse NH, Vugts DJ, Zijlstra JM, Huisman MC, van Dongen GA. Immuno-positron emission tomography with zirconium-89-labeled monoclonal antibodies in oncology: What can we learn from initial clinical trials? Front Pharmacol. 2016;7:131.
155. Dammes N, Peer D. Monoclonal antibody-based molecular imaging strategies and theranostic opportunities. Theranostics. 2020;10(2):938-55.
156. Yoon JK, Park BN, Ryu EK, An YS, Lee SJ. Current perspectives on (89)zr-pet imaging. Int J Mol Sci. 2020;21(12):1-18.
157. Elmekharam N, Gobalakrishnan S, Thadigiri C, Wang L, Gawi A, Zweit J. Labeling of anti-sas1b with zirconium-89 as a novel immune-pet probe for uterine cancer imaging. Journal of Biosciences and Medicines. 2021;09(11):30-41.
158. Perk LR, Vosjan MJ, Visser GW, Budde M, Jurek P, Kiefer GE, van Dongen GA. P-isothiocyanatobenzyl-desferrioxamine: A new bifunctional chelate for facile radiolabeling of monoclonal antibodies with zirconium-89 for immuno-pet imaging. Eur J Nucl Med Mol Imaging. 2010;37(2):250-9.
159. Zhou Y, Li J, Xu X, Zhao M, Zhang B, Deng S, Wu Y. 64cu-based radiopharmaceuticals in molecular imaging. Technology in Cancer Research & Treatment. 2019;18:1533033819830758.
160. Feiner IVJ, Brandt M, Cowell J, Demuth T, Vugts D, Gasser G, Mindt TL. The race for hydroxamate-based zirconium-89 chelators. Cancers (Basel). 2021;13(17).
161. Voss SD, Smith SV, DiBartolo N, McIntosh LJ, Cyr EM, Bonab AA, Dearling JL, Carter EA, Fischman AJ, Treves ST, Gillies SD, Sargeson AM, Huston JS, Packard AB. Positron emission tomography (pet) imaging of neuroblastoma and melanoma with 64cu-sarar immunoconjugates. Proc Natl Acad Sci U S A. 2007;104(44):17489-93.
162. Schneppensieper T, Seibig S, Zahl A, Tregloan P, van Eldik R. Influence of chelate effects on the water-exchange mechanism of polyaminecarboxylate complexes of iron(iii). Inorg Chem. 2001;40(15):3670-6.
163. Huclier-Markai S, Alliot C, Sebti J, Brunel B, Aupiais J. A comparative thermodynamic study of the formation of scandium complexes with dtpa and dota. RSC Advances. 2015;5(121):99606-17.
164. Van De Watering FCJ, Rijpkema M, Perk L, Brinkmann U, Oyen WJG, Boerman OC. Zirconium-89 labeled antibodies: A new tool for molecular imaging in cancer patients. BioMed Research International. 2014;2014:1-13.
165. McQuade P, McCarthy DW, Welch MJ. Metal radionuclides for pet imaging. Positron Emission Tomography. 2006:237-50.
166. Gutfilen B, Souza SA, Valentini G. Copper-64: A real theranostic agent. Drug Des Devel Ther. 2018;12:3235-45.
167. Cai Z, Anderson CJ. Chelators for copper radionuclides in positron emission tomography radiopharmaceuticals. J Labelled Comp Radiopharm. 2014;57(4):224-30.
168. Dearling JL, Paterson BM, Akurathi V, Betanzos-Lara S, Treves ST, Voss SD, White JM, Huston JS, Smith SV, Donnelly PS, Packard AB. The ionic charge of copper-64 complexes conjugated to an engineered antibody affects biodistribution. Bioconjug Chem. 2015;26(4):707-17.
169. Ramakrishnan MS, Eswaraiah A, Crombet T, Piedra P, Saurez G, Iyer H, Arvind AS. Nimotuzumab, a promising therapeutic monoclonal for treatment of tumorsof epithelial origin. Landes Bioscience. 2009(February):41-8.
170. Voss SD, Smith SV, Dibartolo N, McIntosh LJ, Cyr EM, Bonab AA, Dearling JLJ, Carter EA, Fischman AJ, Treves ST, Gillies SD, Sargeson AM, Huston JS, Packard AB. Positron emission tomography (pet) imaging of neuroblastoma and melanoma with ⁶⁴ cu-sarar immunoconjugates. Proceedings of the National Academy of Sciences. 2007;104(44):17489-93.

171. Ramakrishnan MS, Eswaraiah A, Crombet T, Piedra P, Saurez G, Iyer H, Arvind AS. Nimotuzumab, a promising therapeutic monoclonal for treatment of tumors of epithelial origin. mAbs. 2009;1(1):41-8.
172. Treglia G, Salsano M. Pet imaging using radiolabelled antibodies: Future direction in tumor diagnosis and correlate applications. Research and Reports in Nuclear Medicine. 2013.
173. Chang HR. Trastuzumab-based neoadjuvant therapy in patients with her2-positive breast cancer. Cancer. 2010;116(12):2856-67.
174. Persson M, Gedda L, Lundqvist H, Tolmachev V, Nordgren H, Malmstrom PU, Carlsson J. [177lu]pertuzumab: Experimental therapy of her-2-expressing xenografts. Cancer Res. 2007;67(1):326-31.
175. Spector NL, Blackwell KL. Understanding the mechanisms behind trastuzumab therapy for human epidermal growth factor receptor 2-positive breast cancer. J Clin Oncol. 2009;27(34):5838-47.
176. Slamon DJ, Leyland-Jones B, Shak S, Fuchs H, Paton V, Bajamonde A, Fleming T, Eiermann W, Wolter J, Pegram M, Baselga J, Norton L. Use of chemotherapy plus a monoclonal antibody against her2 for metastatic breast cancer that overexpresses her2. N Engl J Med. 2001;344(11):783-92.
177. Hubalek M, Brantner C, Marth C. Role of pertuzumab in the treatment of her2-positive breast cancer. Breast Cancer: Targets and Therapy. 2012:65.
178. Talavera A, Friemann R, GóMez-Puerta S, Martinez-Fleites C, Garrido G, Rabasa A, LóPez-Requena A, Pupo A, Johansen RF, SáNchez O, Krengel U, Moreno E. Nimotuzumab, an antitumor antibody that targets the epidermal growth factor receptor, blocks ligand binding while permitting the active receptor conformation. Cancer Research. 2009;69(14):5851-9.
179. Mazorra Z, Chao L, Lavastida A, Sanchez B, Ramos M, Iznaga N, Crombet T. Nimotuzumab: Beyond the egfr signaling cascade inhibition. Seminars in Oncology. 2018;45(1):18-26.
180. Chen LF, Cohen EE, Grandis JR. New strategies in head and neck cancer: Understanding resistance to epidermal growth factor receptor inhibitors. Clin Cancer Res. 2010;16(9):2489-95.
181. Hansen AR, Siu LL. Epidermal growth factor receptor targeting in head and neck cancer: Have we been just skimming the surface? J Clin Oncol. 2013;31(11):1381-3.
182. Crombet Ramos T, Mestre Fernandez B, Mazorra Herrera Z, Iznaga Escobar NE. Nimotuzumab for patients with inoperable cancer of the head and neck. Front Oncol. 2020;10:817.
183. Qu YY, Hu SL, Xu XY, Wang RZ, Yu HY, Xu JY, Chen L, Dong GL. Nimotuzumab enhances the radiosensitivity of cancer cells in vitro by inhibiting radiation-induced DNA damage repair. PLoS One. 2013;8(8):e70727.
184. Saurez-Martínez G, Bencomo-Yanes A. Nimotuzumab, effective immunotherapy for the treatment of malignant epithelial tumors. Biotecnologia Aplicada. 2014;31(2):150-8.
185. Ramakrishnan MS, Eswaraiah A, Crombet T, Piedra P, Saurez G, Iyer H, Arvind AS. Nimotuzumab, a promising therapeutic monoclonal for treatment of tumors of epithelial origin. MAbs. 2009;1(1):41-8.
186. Perez R, Moreno E, Garrido G, Crombet T. Egfr-targeting as a biological therapy: Understanding nimotuzumab's clinical effects. Cancers (Basel). 2011;3(2):2014-31.
187. Barta P, Laznickova A, Laznicek M, Vera DR, Beran M. Preclinical evaluation of radiolabelled nimotuzumab, a promising monoclonal antibody targeting the epidermal growth factor receptor. J Labelled Comp Radiopharm. 2013;56(5):280-8.
188. Vera DR, Eigner S, Beran M, Henke KE, Laznickova A, Laznicek M, Melichar F, Chinol M. Preclinical evaluation of (177)lu-nimotuzumab: A potential tool for radioimmunotherapy of epidermal growth factor receptor-overexpressing tumors. Cancer Biother Radiopharm. 2011;26(3):287-97.
189. Hartimath SV, Alizadeh E, Solomon VR, Chekol R, Bernhard W, Hill W, Parada AC, Barreto K, Geyer CR, Fonge H. Preclinical evaluation of (111)in-labeled pegylated maytansine nimotuzumab drug conjugates in egfr-positive cancer models. J Nucl Med. 2019;60(8):1103-10.
190. Hartimath SV, El-Sayed A, Makhlouf A, Bernhard W, Gonzalez C, Hill W, Parada AC, Barreto K, Geyer CR, Fonge H. Therapeutic potential of nimotuzumab pegylated-maytansine antibody drug conjugates against egfr positive xenograft. Oncotarget. 2019;10(10):1031-44.

191. Chekol R, Solomon VR, Alizadeh E, Bernhard W, Fisher D, Hill W, Barreto K, DeCoteau JF, Parada AC, Geyer CR, Fonge H. (89)zr-nimotuzumab for immunopet imaging of epidermal growth factor receptor i. Oncotarget. 2018;9(24):17117-32.
192. Izquierdo-Sanchez V, Muniz-Hernandez S, Vazquez-Becerra H, Pacheco-Yepez J, Romero-Pina ME, Arrieta O, Medina LA. Biodistribution and tumor uptake of (67)ga-nimotuzumab in a malignant pleural mesothelioma xenograft. Molecules. 2018;23(12).
193. Nguyen TT, Ho AS, Nguyen TK, Nguyen TN, Bui VC, Nguyen TB, Dang HH, Nguyen DK, Nguyen TN, Nguyen LT. Efficacy of nimotuzumab (hr3) conjugated with (131)i or (90)y in laryngeal carcinoma xenograft mouse model. Int J Radiat Biol. 2021;97(5):704-13.
194. Solomon VR, Barreto K, Bernhard W, Alizadeh E, Causey P, Perron R, Gendron D, Alam MK, Carr A, Geyer CR, Fonge H. Nimotuzumab site-specifically labeled with 89zr and 225ac using spytag/spycatcher for pet imaging and alpha particle radioimmunotherapy of epidermal growth factor receptor positive cancers. Cancers. 2020;12(11).
195. Wilken JA, Badri T, Cross S, Raji R, Santin AD, Schwartz P, Branscum AJ, Baron AT, Sakhitab AI, Maihle NJ. Egfr/her-targeted therapeutics in ovarian cancer. Future Med Chem. 2012;4(4):447-69.
196. Al Shoyaib A, Archie SR, Karamyan VT. Intraperitoneal route of drug administration: Should it be used in experimental animal studies? Pharm Res. 2019;37(1):12.
197. Yang S, Feng R, Pan ZC, Jiang T, Xu Q, Chen Q. A comparison of intravenous plus intraperitoneal chemotherapy with intravenous chemotherapy alone for the treatment of gastric cancer: A meta-analysis. Sci Rep. 2015;5(September 2014):12538.
198. Benedetti MS, Whomsley R, Poggesi I, Cawello W, Mathy Fo-X, Delporte M-L, Papeleu P, Watelet J-B. Drug metabolism and pharmacokinetics. Drug Metabolism Reviews. 2009;41(3):344-90.
199. Dou S, Smith M, Wang Y, Rusckowski M, Liu G. Intraperitoneal injection is not always a suitable alternative to intravenous injection for radiotherapy. Cancer Biother Radiopharm. 2013;28(4):335-42.
200. Chaudhary K, Haddadin S, Nistala R, Papageorgio C. Intraperitoneal drug therapy: An advantage. Curr Clin Pharmacol. 2010;5(2):82-8.
201. Shimada T, Nomura M, Yokogawa K, Miyamoto K-I, Endo Y, Sasaki T, Yonemura Y, Miyamoto KI. Pharmacokinetic advantage of intraperitoneal injection of docetaxel in the treatment for peritoneal dissemination of cancer in mice. JPP. 2005;57:177-81.
202. de Bree E, Michelakis D, Stamatiou D, Romanos J, Zoras O. Pharmacological principles of intraperitoneal and bidirectional chemotherapy. Pleura Peritoneum. 2017;2(2):47-62.
203. Turner PV, Brabb T, Pekow C, Vasbinder MA. Administration of substances to laboratory animals: Routes of administration and factors to consider. J Am Assoc Lab Anim Sci. 2011;50(5):600-13.
204. Altwerger G, Menderes G, Black JD, Azodi M. Should we continue intra-peritoneal chemotherapy in advanced ovarian cancer patients? Integrative cancer science and therapeutics. 2016;3.
205. Adil IH, Irshad AUR. A modified approach for detection of outliers. Pakistan Journal of Statistics and Operation Research. 2015;11(1):91.
206. Leys C, Ley C, Klein O, Bernard P, Licata L. Detecting outliers: Do not use standard deviation around the mean, use absolute deviation around the median. Journal of Experimental Social Psychology. 2013;49(4):764-6.
207. Newell KM, Hancock PA. Forgotten moments: A note on skewness and kurtosis as influential factors in inferences extrapolated from response distributions. Journal of motor behavior. 1984;16(3):320-35.
208. Duvenhage J, Ebenhan T, Garny S, Hernandez Gonzalez I, Leyva Montana R, Price R, Birkholtz LM, Zeevaart JR. Molecular imaging of a zirconium-89 labeled antibody targeting plasmodium falciparum-infected human erythrocytes. Mol Imaging Biol. 2020;22(1):115-23.

209. Rosenbaum SE. Basic pharmacokinetics and pharmacodynamics an integrated textbook and computer simulations. Newark: John Wiley & Sons, Incorporated; 2016. Available from: https://public.ebookcentral.proquest.com/choice/PublicFullRecord.aspx?p=7104454.
210. Ahmed TA. Pharmacokinetics of drugs following iv bolus, iv infusion, and oral administration. Basic pharmacokinetic concepts and some clinical applications: InTech; 2015.
211. Pocratsky AM, Sleigh JN. Intraperitoneal injection of neonatal mice. Bio Protoc. 2023;13(18):e4826.
212. Solon EG. Use of radioactive compounds and autoradiography to determine drug tissue distribution. Chemical research in toxicology. 2012;25(3):543-55.
213. Lukas G, Brindle SD, Greengard P. The route of absorption of intraperitoneally administered compounds. The Journal of pharmacology and experimental therapeutics. 1971;178(3):562-4.
214. Downer JB, Jones LA, Katzenellenbogen JA, Welch MJ. Effect of administration route on fes uptake into mcf-7 tumors. Nuclear Medicine and Biology. 2001;28(4):397-9.
215. Mostafa AMA, Zakaly HMH, Issa SAM, Uosif MAM, Alrowaili ZA, Zhukovsky MV. Exploring the potential of zirconium-89 in diagnostic radiopharmaceutical applications: An analytical investigation. Biomedicines. 2023;11(4).
216. Abou DS, Ku T, Smith-Jones PM. In vivo biodistribution and accumulation of 89zr in mice. Nuclear Medicine and Biology. 2011;38(5):675-81.
217. Martínez DV, Valenzuela JJ, Cariseo CV, Orellana MV, Iwanaga J, Gold M, Santana A. Incidence and clinical implications of anatomical variations of the pancreas. A systematic review. The FASEB Journal. 2022;36.
218. Bartolo ND, Sargeson AM, Donlevy TM, Smith SV. Synthesis of a new cage ligand, sarar, and its complexation with selected transition metal ions for potential use in radioimaging. Journal of The Chemical Society-dalton Transactions. 2001:2303-9.
219. Ryman JT, Meibohm B. Pharmacokinetics of monoclonal antibodies. CPT: pharmacometrics & systems pharmacology. 2017;6(9):576-88.
220. Feng B, LaPerle JL, Chang G, Varma MVS. Renal clearance in drug discovery and development: Molecular descriptors, drug transporters and disease state. Expert Opinion on Drug Metabolism & Toxicology. 2010;6(8):939-52.
221. Masereeuw R, Russel FGM. Mechanisms and clinical implications of renal drug excretion*. Drug Metabolism Reviews. 2001;33(3-4):299-351.
222. Scott RP, Quaggin SE. The cell biology of renal filtration. Journal of Cell Biology. 2015;209(2):199-210.
223. Zamek-Gliszczynski MJ, Hoffmaster KA, Nezasa K-i, Tallman MN, Brouwer KLR. Integration of hepatic drug transporters and phase ii metabolizing enzymes: Mechanisms of hepatic excretion of sulfate, glucuronide, and glutathione metabolites. European Journal of Pharmaceutical Sciences. 2006;27(5):447-86.
224. Robinson MW, Harmon C, O'Farrelly C. Liver immunology and its role in inflammation and homeostasis. Cellular & molecular immunology. 2016;13(3):267-76.
225. Sharma SK, Glaser JM, Edwards KJ, Khozeimeh Sarbisheh E, Salih AK, Lewis JS, Price EW. A systematic evaluation of antibody modification and 89zr-radiolabeling for optimized immuno-pet. Bioconjugate chemistry. 2021;32(7):1177-91.
226. Hong H, Zha Z, Zhao R, Luo Y, Jin W, Li L, Wang R, Yan L, Wang H, Ploessl K, Qiao J, Zhu L, Kung HF. [68ga]ga-hbed-cc-fapi derivatives with improved radiolabeling and specific tumor uptake. Molecular pharmaceutics. 2023;20(4):2159-69.

10. APPENDIX

Table A1: Study groups and application and comments for inclusion/exclusion criteria

Compound	Route of injection	Time of scan	Number of mice	Enrolled	Excluded	Reason for exclusion
[^{89}Zr]Zr-oxalate	IP	1 h	5	4	1	The scan was incomplete.
		2 h	6	4	2	Poor image quality.
		4 h	6	4	2	Poor image quality.
		6 h	4	3	1	Poor image quality.
		8 h	3	2	1	Scan was unavailable.
		24 h	3	2	1	Poor image quality.
[^{89}Zr]Zr-DFO-h-R3	IP	2 h	6	2	4	One scan with poor image quality. Three scans were inaccessible.
		4 h	3	1	2	One scan lacked quality. One scan was inaccessible.
		6 h	6	2	4	One scan lacked quality. Three scans were inaccessible or incomplete.
		24 h	6	2	4	Two scans incomplete and two scans inaccessible.
		48 h	3	2	1	Lacking scan quality – no solution for mismatching.
	IV	5 min	2	1	1	One scan was inaccessible.
		1 h	1	0	1	The scan was incomplete, (scan area for head cut off).
		2 h	3	3	0	
		4 h	2	2	0	

		6 h	6	3	3	Three scans were inaccessible / incomplete.
		24 h	3	3	0	
		48 h	3	3	0	
[^{64}Cu]Cu-Cl_2	IP	1 h	6	6	0	
		2 h	6	6	0	
		4 h	6	6	0	
		6 h	6	5	1	One scan was inaccessible.
[^{64}Cu]Cu-SarAr-h-R3	IV	2 h	4	3	1	The image quality was poor.
		4 h	3	3	0	
		6 h	4	3	1	The scan was incomplete.
		24 h	4	4	0	
[^{64}Cu]Cu-DOTA-h-R3	IV	2 h	2	2	0	
		4 h	1	1	0	
		6 h	2	2	0	
		24 h	2	2	0	
Total			117	87	30	

Table A2: Calculations of CV, SD, and mean SUV for IV administered [^{89}Zr]Zr-DFO-h-R3.

Region	Time point (h)	Mean SUV (kBq/ml)	SD (kBq/ml)	CV
Cardiac	2	0.161	0.044	0.060
	4	0.107	0.041	0.006
	6	0.079	0.026	0.089
	24	0.036	0.008	0.032
	48	0.014	0.006	0.012
Chest	2	0.026	0.002	0.090
	4	0.041	0.003	0.080
	6	0.033	0.018	0.541
	24	0.042	0.005	0.126
	48	0.024	0.013	0.533
Abdomen	2	0.018	0.003	0.151
	4	0.028	0.008	0.300
	6	0.020	0.013	0.640
	24	0.024	0.005	0.225

	48	0.013	0.008	0.629
Whole body	2	0.012	0.004	0.300
	4	0.019	0.004	0.221
	6	0.014	0.010	0.681
	24	0.017	0.003	0.172
	48	0.010	0.006	0.631

Table A3: Statistical analysis for IV administered [^{89}Zr]Zr-DFO-h-R3

Region	Time point (h)	*P-values*
Cardiac	2 vs 4	**0.003**
	2 vs 6	0.572
	2 vs 24	0.105
	2 vs 48	0.377
	4 vs 6	0.569
	4 vs 24	0.070
	4 vs 48	0.071
	6 vs 24	0.931
	6 vs 48	0.337
	24 vs 48	0.152
Chest	2 vs 4	0.043
	2 vs 6	0.580
	2 vs 24	**0.022**
	2 vs 48	0.803
	4 vs 6	0.509
	4 vs 24	0.885
	4 vs 48	0.138
	6 vs 24	0.484
	6 vs 48	0.526
	24 vs 48	0.125
Abdomen	2 vs 4	0.326
	2 vs 6	0.800
	2 vs 24	0.199
	2 vs 48	0.405
	4 vs 6	0.470
	4 vs 24	0.598
	4 vs 48	0.173
	6 vs 24	0.696
	6 vs 48	0.470
	24 vs 48	0.143
Whole body	2 vs 4	0.192
	2 vs 6	0.778
	2 vs 24	0.175
	2 vs 48	0.608

	4 vs 6	0.460
	4 vs 24	0.527
	4 vs 48	0.137
	6 vs 24	0.688
	6 vs 48	0.563
	24 vs 48	0.188

Footnote: $P < 0.05$ was considered statistically significant.

Table A4: Calculations of CV, SD, and mean SUV for IP administered [^{89}Zr]Zr-DFO-h-R3.

Region	Time point (h)	Mean SUV (kBq/ml)	SD (kBq/ml)	CV
Cardiac region	2	0.144	0.061	0.424
	6	0.184	0.036	0.198
	24	0.114	0.009	0.076
	48	0.069	0.004	0.060
Chest	2	0.073	0.054	0.738
	6	0.085	0.016	0.186
	24	0.066	0.010	0.159
	48	0.040	0.001	0.033
Abdomen	2	0.094	0.009	0.097
	6	0.070	0.013	0.187
	24	0.036	0.009	0.264
	48	0.020	0.003	0.131
Whole body	2	0.044	0.006	0.130
	6	0.040	0.006	0.147
	24	0.025	0.003	0.132
	48	0.015	0.002	0.141

Table A5: Statistical analysis for IP administered [^{89}Zr]Zr-DFO-h-R3.

Region	Time point (h)	*P-values*
Cardiac	2 vs 6	0.525
	2 vs 24	0.610
	2 vs 48	0.332
	6 vs 24	0.208
	6 vs 48	0.136
	24 vs 48	**0.048**
Chest	2 vs 6	0.809

	2 vs 24	0.880
	2 vs 48	0.543
	6 vs 24	0.305
	6 vs 48	0.152
	24 vs 48	0.172
Abdomen	2 vs 6	0.185
	2 vs 24	**0.025**
	2 vs 48	**0.040**
	6 vs 24	0.107
	6 vs 48	0.105
	24 vs 48	0.233
Whole body	2 vs 6	0.504
	2 vs 24	0.078
	2 vs 48	0.060
	6 vs 24	0.120
	6 vs 48	0.077
	24 vs 48	0.088

Footnote: $P < 0.05$ was considered statistically significant.

Table A6: Calculations of CV, SD, and mean SUV for IP administered [^{89}Zr]Zr-oxalate.

Region	Time point (h)	Mean SUV (kBq/ml)	SD (kBq/ml)	CV
Cardiac region	1	0.034	0.009	0.262
	2	0.048	0.009	0.179
	4	0.050	0.010	0.205
	6	0.046	0.007	0.154
Chest	1	0.022	0.008	0.354
	2	0.030	0.006	0.216
	4	0.032	0.005	0.160
	6	0.031	0.004	0.132
Abdomen	1	0.034	0.008	0.232
	2	0.028	0.006	0.231
	4	0.023	0.004	0.168
	6	0.019	0.004	0.186
Whole body	1	0.014	0.002	0.110
	2	0.015	0.002	0.150
	4	0.014	0.002	0.159
	6	0.012	0.002	0.147

Table A7: Statistical analysis for IP administered [^{89}Zr]Zr-oxalate

Region	Time point (h)	*P-values*
Cardiac	1 vs 2	0.070
	1 vs 4	0.065
	1 vs 6	0.756
	2 vs 4	0.812
	2 vs 6	0.315
	4 vs 6	0.264
Chest	1 vs 2	0.191
	1 vs 4	0.083
	1 vs 6	0.627
	2 vs 4	0.563
	2 vs 6	0.564
	4 vs 6	0.341
Abdomen	1 vs 2	0.281
	1 vs 4	0.055
	1 vs 6	**0.025**
	2 vs 4	0.210
	2 vs 6	0.060
	4 vs 6	0.181
Whole body	1 vs 2	0.665
	1 vs 4	0.955
	1 vs 6	0.131
	2 vs 4	0.672
	2 vs 6	0.099
	4 vs 6	0.180

Footnote: $P < 0.05$ was considered statistically significant.

Table A8: CV, SD, and mean SUV calculated for IV administered [^{64}Cu]Cu-DOTA-h-R3.

Region	Time point (h)	Mean SUV (kBq/ml)	SD (kBq/ml)	CV
Cardiac region	2	0.088	0.013	0.389
	6	0.057	0.012	0.018
	24	0.013	0.004	0.280
Chest	2	0.019	0.004	0.226
	6	0.020	0.005	0.226
	24	0.008	0.002	0.260
Abdomen	2	0.046	0.010	0.214
	6	0.040	0.010	0.242
	24	0.011	0.002	0.218
Whole body	2	0.025	0.006	0.249
	6	0.018	0.004	0.199
	24	0.006	0.001	0.207

Table A9: Statistical analysis for IV administered [^{64}Cu]Cu-DOTA-h-R3.

Region	Time point (h)	*P-values*
Cardiac	2 vs 6	0.056
	2 vs 24	0.097
	6 vs 24	0.089
Chest	2 vs 6	0.835
	2 vs 24	0.125
	6 vs 24	0.122
Abdomen	2 vs 6	0.617
	2 vs 24	0.109
	6 vs 24	0.130
Whole body	2 vs 6	0.332
	2 vs 24	0.132
	6 vs 24	0.102

Footnote: $P < 0.05$ was considered statistically significant.

Table A10: CV, SD, and mean SUV calculated for IV administered [^{64}Cu]Cu-SarAr-h-R3.

Region	Time point (h)	Mean SUV (kBq/ml)	SD (kBq/ml)	CV
Cardiac region	2	0.163	0.061	0.537
	4	0.089	0.023	0.648
	6	0.058	0.025	0.781
	24	0.034	0.022	0.737
Chest	2	0.043	0.042	0.962
	4	0.036	0.050	1.364
	6	0.038	0.034	0.908
	24	0.009	0.008	0.942
Abdomen	2	0.026	0.019	0.753
	4	0.019	0.020	1.041
	6	0.026	0.016	0.607
	24	0.008	0.005	0.699
Whole body	2	0.016	0.013	0.797
	4	0.011	0.013	1.100
	6	0.013	0.009	0.689
	24	0.004	0.003	0.692

Table A11: Statistical analysis for IV administered [^{64}Cu]Cu-SarAr-h-R3.

Region	Time point (h)	*P-values*
Cardiac	2 vs 4	0.058
	2 vs 6	0.098
	2 vs 24	0.234
	4 vs 6	0.158
	4 vs 24	0.202
	6 vs 24	0.331
Chest	2 vs 4	0.865
	2 vs 6	0.866
	2 vs 24	0.285
	4 vs 6	0.975
	4 vs 24	0.435
	6 vs 24	0.278

Abdomen	2 vs 4	0.688
	2 vs 6	0.995
	2 vs 24	0.245
	4 vs 6	0.664
	4 vs 24	0.431
	6 vs 24	0.176
Whole body	2 vs 4	0.686
	2 vs 6	0.784
	2 vs 24	0.248
	4 vs 6	0.850
	4 vs 24	0.426
	6 vs 24	0.223

Footnote: $P < 0.05$ was considered statistically significant.

Table A12: CV, SD, and mean SUV calculated for IP administered [^{64}Cu]Cu-Cl_2.

Region	**Time point (h)**	**Mean SUV (kBq/ml)**	**SD (kBq/ml)**	**CV**
Cardiac region	1	0.102	0.028	0.275
	2	0.118	0.031	0.264
	4	0.136	0.031	0.230
	6	0.134	0.031	0.231
Chest	1	0.062	0.019	0.308
	2	0.076	0.023	0.308
	4	0.075	0.017	0.231
	6	0.069	0.017	0.239
Abdomen	1	0.247	0.042	0.169
	2	0.200	0.039	0.194
	4	0.183	0.030	0.166
	6	0.161	0.030	0.184
Whole body	1	0.109	0.018	0.168
	2	0.096	0.021	0.217
	4	0.088	0.014	0.161
	6	0.079	0.016	0.199

Table A13: Statistical analysis for IP administered of [^{64}Cu]Cu-Cl_2.

Region	Time point (h)	*P-values*
Cardiac	1 vs 2	0.390
	1 vs 4	**0.082**
	1 vs 6	0.118
	2 vs 4	0.344
	2 vs 6	0.419
	4 vs 6	0.919
Chest	1 vs 2	0.281
	1 vs 4	0.226
	1 vs 6	0.505
	2 vs 4	0.972
	2 vs 6	0.598
	4 vs 6	0.563
Abdomen	1 vs 2	0.067
	1 vs 4	**0.014**
	1 vs 6	**0.003**
	2 vs 4	0.435
	2 vs 6	0.092
	4 vs 6	0.247
Whole body	1 vs 2	0.267
	1 vs 4	0.054
	1 vs 6	**0.019**
	2 vs 4	0.485
	2 vs 6	0.177
	4 vs 6	0.370

Footnote: $P < 0.05$ was considered statistically significant.

Table A14: Organ biodistribution of IP and IV administered [^{89}Zr]Zr-DFO-h-R3.

[^{89}Zr]Zr-DFO-h-R3	IP (48 h p.i.)		IV (48 h p.i.)		*P*-values
Organ	**Mean (%ID/g)**	**SEM**	**Mean (%ID/g)**	**SEM**	
Whole blood	3.177	0.524	4.405	0.676	**0.032**
Plasma	19.971	1.050	19.176	0.864	0.288
Heart	4.638	0.580	5.710	0.037	0.085
Lung	7.017	3.146	6.231	1.006	0.711
Muscle	1.493	0.367	1.412	0.160	0.705
Femur	5.459	2.291	3.794	1.355	0.259
Skin	5.150	0.471	5.078	0.243	0.799
Ovaries	4.489	1.489	3.501	0.244	0.369
Large Intestine	1.418	0.017	1.008	0.162	**0.005**
Spleen	6.548	2.382	4.384	0.956	0.167
Stomach	0.946	0.486	0.548	0.176	0.201
Small Intestine	1.853	0.092	1.268	0.187	**0.001**
Liver	4.085	1.128	3.165	0.423	0.203
Pancreas	3.654	1.189	1.420	0.100	**0.033**
Kidneys	10.360	1.212	9.102	0.235	0.125
Bladder	6.538	2.940	5.095	2.882	0.533
Urine	1.458	0.564	1.719	0.157	0.510

Footnotes: $P < 0.05$ was considered statistically significant. IP: n=4; IV: n=5.

Table A15: Organ and tissue biodistribution of IP administered [^{89}Zr]Zr-DFO-h-R3 at endpoint.

[^{89}Zr]Zr-DFO-h-R3	IP (24 h p.i.)		IP (48 h p.i.)		*P- values*
Organ	**Mean (%ID/g)**	**SEM**	**Mean (%ID/g)**	**SEM**	
Whole blood	6.325	1.998	3.167	0.524	**0.046**
Plasma	15.897	2.609	19.971	1.050	**0.045**
Heart	5.277	1.359	4.638	0.579	0.444
Lung	5.823	0.569	7.017	3.146	0.580
Muscle	1.066	0.231	1.493	0.366	0.105
Femur	2.924	0.188	5.459	2.291	0.113
Skin	3.585	0.742	5.150	0.472	**0.016**
Ovaries	4.300	0.407	4.489	1.489	0.850
Large Intestine	1.358	0.172	1.418	0.017	0.536
Spleen	4.500	0.671	6.548	2.382	0.185
Stomach	0.732	0.233	0.946	0.486	0.469
Small Intestine	1.661	0.234	1.853	0.093	0.202
Liver	2.609	0.189	4.085	1.128	0.077
Kidneys	5.707	0.655	10.360	1.212	**0.003**
Bladder	3.721	2.783	6.538	2.939	0.264
Urine	6.525	2.403	1.458	0.564	**0.020**

Footnote: $P < 0.05$ was considered statistically significant. Groups: 24h: n=6; 48h:n=4.

Table A16: Biodistribution after IP administered [^{89}Zr]Zr-oxalate and [^{89}Zr]Zr-DFO-h-R3.

[^{89}Zr]Zr-oxalate and [^{89}Zr]Zr-DFO-h-R3	**[^{89}Zr]Zr-oxalate - IP (24 h p.i.)**		**[^{89}Zr]Zr-DFO-h-R3 - IP (24 h p.i.)**		***P- values***
Organ	**Mean (%ID/g)**	**SEM**	**Mean (%ID/g)**	**SEM**	
Whole blood	2.536	0.103	6.325	1.998	**0.032**
Plasma	2.444	1.516	15.897	2.609	**< 0.001**
Heart	1.476	0.079	5.277	1.359	**0.011**
Lung	2.463	0.229	5.823	0.569	**< 0.001**
Muscle	0.871	0.415	1.067	0.231	0.367
Femur	17.237	4.346	2.924	0.188	**< 0.001**
Skin	3.488	0.471	3.585	0.742	0.829
Ovaries	2.626	0.849	4.300	0.407	**0.010**
Large Intestine	1.964	0.802	1.358	0.172	0.126
Spleen	3.882	1.253	4.500	0.671	0.368
Stomach	0.426	0.224	0.732	0.233	0.082
Small Intestine	1.704	0.449	1.661	0.234	0.846
Liver	2.719	0.703	2.609	0.189	0.728
Bile	0.435	0.406	4.424	3.517	0.107
Kidneys	7.230	2.511	5.707	0.655	0.213
Bladder	2.519	0.216	3.721	2.783	0.452
Urine	0.490	0.404	6.525	2.403	**0.014**

Footnotes: $P < 0.05$ was considered statistically significant. *Ex vivo* data sets [^{89}Zr]Zr-oxalate (n=6) and [^{89}Zr]Zr-DFO-h-R3 (n=6).

Table A17: Biodistribution of IV injected [^{64}Cu]Cu-DOTA-h-R3 and [^{64}Cu]Cu-SarAr-h-R3.

[^{64}Cu]Cu-DOTA-h-R3 and [^{64}Cu]Cu-SarAr-h-R3	IV [^{64}Cu]Cu-DOTA-h-R3 (24 h p.i.)		IV [^{64}Cu]Cu-SarAr-h-R3 (24 h p.i)		*P- values*
Organ	**Mean (%ID/g)**	**SEM**	**Mean (%ID/g)**	**SEM**	
Whole blood	1.999	1.047	2.846	0.749	0.221
Plasma	8.843	2.043	12.008	1.890	**0.047**
RBCs	4.338	0.767	5.918	1.622	0.075
Heart	6.718	1.465	3.850	0.334	0.088
Lung	11.073	2.494	3.954	1.119	**0.006**
Muscle	0.996	0.310	0.787	0.194	0.563
Femur	1.745	0.381	1.373	0.522	0.230
Skin	3.566	0.964	2.589	0.462	0.133
Ovaries	2.168	0.722	1.737	0.526	0.591
Large Intestine	10.096	3.786	1.774	0.700	**0.021**
Spleen	5.349	1.584	2.695	0.436	**0.039**
Stomach	1.983	1.375	0.662	0.135	0.171
Small Intestine	7.088	2.598	1.469	0.584	**0.021**
Liver	16.625	4.241	5.286	2.306	**0.006**
Gallbladder	4.924	2.906	3.817	2.216	0.599
Kidneys	12.870	2.597	12.506	3.892	0.866
Bladder	2.824	0.992	0.655	0.108	0.063
Urine	1.209	1.225	1.818	0.459	0.404

Footnotes: $P < 0.05$ was considered statistically significant. *Ex vivo* data sets [^{64}Cu]Cu-DOTA-h-R3 (n=4) and [^{64}Cu]Cu-SarAr-h-R3 (n=6).

Table A18: Organ biodistribution of IV- and IP administered [^{64}Cu]Cu-Cl_2 (n=6).

[^{64}Cu]Cu-Cl_2	IV (6 h p.i.)		IP (6 h p.i.)		*P- values*
Organ	**Mean (%ID/g)**	**SEM**	**Mean (%ID/g)**	**SEM**	
Whole blood	2.282	0.599	3.795	0.190	**0.003**
Heart	6.357	1.863	8.859	0.111	**0.022**
Lung	13.792	1.523	16.532	3.663	0.140
Muscle	1.122	0.265	1.952	0.220	**< 0.001**
Femur	2.822	0.362	4.607	0.413	**< 0.001**
Skin	5.002	0.893	4.073	0.439	0.087
Ovaries	3.752	0.587	4.651	0.824	0.122
Large Intestine	5.523	3.323	27.800	1.898	**< 0.001**
Spleen	6.597	3.227	8.441	1.144	0.282
Stomach	6.794	1.736	3.508	0.735	**0.004**
Small Intestine	3.937	0.432	19.242	4.260	**< 0.001**
Liver	6.188	2.050	32.879	1.327	**< 0.001**
Kidneys	14.525	1.227	18.282	1.843	**0.006**
Bladder	4.529	2.441	11.345	4.961	**0.018**
Urine	2.032	1.161	3.554	1.468	0.099

Footnote: $P < 0.05$ was considered statistically significant.